Spring 4-22-2013

A Rigorous Solution for Finite-State Inflow throughout the Flowfield

Zhongyang Fei
Washington University in St. Louis

WASHINGTON UNIVERSITY IN ST. LOUIS

School of Engineering and Applied Science

Department of Mechanical Engineering and Materials Science

Disseration Examination Committee:

David Peters, Chair
Philip Bayly
Guy Genin
Kenneth Jerina
Swaminathan Karunamoorthy
Jr-Shin Li

A Rigorous Solution for Finite-State Inflow throughout the Flowfield

by

Zhongyang Fei

A dissertation presented to the
Graduate School of Arts and Sciences
of Washington University in
partial fulfillment of the
requirements for the degree
of Doctor of Philosophy

May 2013

Saint Louis, Missouri

Table of Contents

List of Figures

List of Tables

List of Abbreviations

a_n^m, b_n^m: cosine and sine induced inflow expansion coefficients

$\bar{a}_n^m, \bar{b}_n^m$: real and imaginary part for cosine induced inflow expansion coefficients

$[D]$: damping matrix

E: error norm

$\vec{f}$: external body forces

H_n^m: combination of double factorials, $\frac{(n+m-1)!!(n-m-1)!!}{(n+m)!!(n-m)!!}$

k: thermal conductivity

K_n^m: Legendre constant, $(\pi/2)^{(-1)^{n+m}} H_n^m$

$[\tilde{L}]$: influence coefficient matrix

$[M]$: mass matrix

m, r: harmonic numbers

n, j: polynomial numbers

P: pressure divided by $V_\infty^2 \rho$ (non-dimensional)

p: pressure

$\bar{P}_m^n(\nu)$: normalized Legendre function of first kind

$\bar{Q}_m^n(i\eta)$: normalized Legendre function of second kind

R: rotor radius

t: time

$\bar{t}$:	nondimensinal time, Ωt
T :	temperature
$\vec{u}, \vec{w}$:	real and imaginary parts of velocity vector
$\vec{v}$:	vector of velocity components
$v_r, v_z, v_{\bar{\psi}}$:	radial, axial, and azimuthal induced velocity components of $\vec{v}$
V_∞ :	free-stream velocity
x, y, z :	non-dimensional rotor disk coordinates, coordinate divided by R
x_0, y_0 :	the Cartesian coordinates of the intersection point of rotor plane and the free-stream line, passing through a point $\nu, \eta, \bar{\psi}$
α_n^m, β_n^m :	velocity coefficients in Peters-He dynamic wake model
ξ :	non-dimensional coordinate along free-stream line, positive downstream, below disk
ρ :	air density
τ :	reduced time, $V_\infty t / R$
τ_n^{mc}, τ_n^{ms} :	cosine and sine part of pressure coefficients
ω :	frequency
$\vec{\upsilon}$:	complex representation of $\vec{v}$
Φ_n^{mc}, Φ_n^{ms} :	cosine and sine part of pressure potentials
$\bar{\Phi}$:	viscosity dissipation function
χ :	skew angle
Ψ_n^{mc}, Ψ_n^{ms} :	cosine and sine part of velocity potentials
$\nu, \eta, \bar{\psi}$:	ellipsoidal coordinates

$\nu_0, \eta_0, \bar{\psi}_0$: the ellipsoidal coordinates of the intersection point of rotor plane and the free-stream line

$\nu_0^*, \eta_0^*, \bar{\psi}_0^*$: the ellipsoidal coordinates of the centro-symmetric point of the intersection point of rotor plane and the free-stream line

$\nu^*, \eta^*, \bar{\psi}^*$: the ellipsoidal coordinates of the centro-symmetric point of the current position

$\tilde{\psi}_0$: azimuth angle on opposite side of rotor, which is equivalent to $\bar{\psi}_0 + \pi$

ω: reduced frequency, $\omega = \Omega R / V_\infty$

Ω: rotor speed, rad/sec

$\overset{+}{(\ )}$: Derivative with respect to non-dimensional time, i.e., $\partial / \partial \bar{t}$

$\overset{*}{(\ )}$: Derivative with respect to reduced time, i.e., $\partial / \partial \tau$

$\vec{\nabla}$: Laplacean operator

$(n)!!$: Double factorial of (n)

$$(n)!! = (n)(n-2)(n-4)\ldots(2), n = even$$
$$(n)!! = (n)(n-2)(n-4)\ldots(1), n = odd$$
$$(0)!! = 1; (-1)!! = 1; (-2)!! = \infty; (-3)!! = -1$$

Acknowledgments

I would like to thank Dr. David A. Peters for his endless support and help during my graduate study. It is really pleasant to work with him. He is an enthusiastic scientist and advisor. He is always available no matter when and where I need to discuss with him. His profound interpretation of the helicopter systems and theory inspirits me and guides me forward.

Thanks to the committee members, Dr. Phillip Bayly, Dr. Guy Genin, Dr. Kenneth Jerina, Dr. Swaminathan Karunamoorthy and Dr. Jr-Shin Li, for their support and advice. This work was sponsored by the joint Georgia Tech/Washington University in St. Louis Rotorcraft Center of Excellence, Dr. Michael Rutkowski and Dr. Robert Ormiston, Technical Monitors.

Zhongyang Fei

Washington University in St. Louis

March 2013

ABSTRACT OF THE DISSERTATION

A Rigorous Solution for Finite-State Inflow throughout the Flowfield

by

Zhongyang Fei

Doctor of Philosophy in Mechanical Engineering

Washington University in St. Louis, 2013

Professor David A. Peters

In this research, the Hseih/Duffy model is extended to all three velocity components of inflow across the rotor disk in a mathematically rigorous way so that it can be used to calculate the inflow below the rotor disk plane. This establishes a complete dynamic inflow model for the entire flow field with finite state method. The derivation is for the case of general skewed angle. The cost of the new method is that one needs to compute the co-states of the inflow equations in the upper hemisphere along with the normal states. Numerical comparisons with exact solutions for the z-component of flow in axial and skewed angle flow demonstrate excellent correlation with closed-form solutions. The simulations also illustrate that the model is valid at both the frequency domain and the time domain.

Meanwhile, in order to accelerate the convergence, an optimization of even terms is used to minimize the error in the axial component of the induced velocity in the on and on/off disk region. A novel method for calculating associate Legendre function of the second kind is also developed to solve the problem of divergence of $\bar{Q}_n^m(i\eta)$ for large η with the iterative method. An application of the new model is also conducted to compute inflow in the wake of a rotor with a finite number of blades. The velocities are plotted at different distances from the rotor disk and are

compared with the Glauert prediction for axial flow and wake swirl. In the finite-state model, the angular momentum does not jump instantaneously across the disk, but it does transition rapidly across the disk to correct Glauert value.

Chapter 1 Introduction

During the past thirty years, finite-state inflow models have developed steadily and moved from heuristic momentum-theory approximations to become rigorous solutions to the potential flow equations in three dimensions. The finite-state method is treated as an alternate method to the traditional vortex-lattice methods (VLM) or the computational fluid dynamic (CFD) approach. However, compared to these approaches, the finite-state method requires less computation and therefore can be used for real time rotor wake analysis.

The states of the models which have been developed are, by definition, unknowns in a set of first-order, ordinary differential equations—the coefficients of which depend on the free-stream impingement angle, the flight speed, and the thrust. The coefficients of the differential equations take the form of a mass matrix, a damping matrix, and an influence-coefficient matrix. For the Peters-He and Peters-Morillo models, these matrices are all in closed form, so they are easily assembled and can be used efficiently and reliably. After many years of evolution, the current model (Hsieh/Duffy model) has been developed such that one can compute all three components of the induced flow in the upper hemisphere above the plane of the rotor disk. However, the model is incapable of computing the induced flow in the hemisphere below the rotor disk. The flow below the disk is required in many applications—such as calculating the interaction of a rotor with external aerodynamic surfaces or with another rotor.

The main purpose of this study is to extend the Hsieh/Duffy model such that it can be used to compute induced flow below the plane of the rotor disk. This will establish a complete, finite-state dynamic inflow model for the entire flow field.

1.1 Previous Work

In the early 1980s, based on Mangler's actuator-disc theory, Ref. [1], Dale Pitt and David Peters developed a linear, unsteady theory that relates the transient rotor loads (thrust, roll moment and pitch moment) to the overall transient response of the rotor induced flow field, which is known as the Pitt-Peters model now, Ref. [2]. The perturbed induced inflow and the pressure distribution are defined as

$$\lambda = \lambda_0 + \bar{r}\lambda_s \sin(\bar{\psi}) + \bar{r}\lambda_c \cos(\bar{\psi}) \tag{1.1}$$

$$P = \sum_{m=0}^{1} \sum_{n=m+1}^{m+3} P_n^m(\nu) Q_n^m(i\eta) \left[C_n^m \cos(m\bar{\psi}) + D_n^m \sin(m\bar{\psi}) \right] \tag{1.2}$$

where ν, η and $\bar{\psi}$ are ellipsoidal coordinates defined in Appendix 1. P_n^m and Q_n^m are associated Legendre functions of the first and second kinds, and C_n^m and D_n^m are coefficients which are functions of time and are governed by a set of ordinary differential equations. With the assumption of superposition of pressure, in which the velocity field is derived from superimposing the unsteady pressure and static pressure of the flow, they obtained a set of differential equations to obtain the dynamic inflow derivatives for a helicopter rotor with an unsteady loading and induced flow distribution. The equations are expressed as:

$$[M] \begin{Bmatrix} \overset{+}{\lambda}_0 \\ \lambda_s \\ \lambda_c \end{Bmatrix} + [L]^{-1} \begin{Bmatrix} \lambda_0 \\ \lambda_s \\ \lambda_c \end{Bmatrix} = \begin{Bmatrix} C_T \\ -C_L \\ -C_M \end{Bmatrix} \tag{1.3}$$

where $[M]$ and $[L]$ are apparent mass matrix and the dynamic inflow gain matrix, respectively. They are defined as follows

$$[M] = \begin{bmatrix} \frac{128}{75\pi} & 0 & 0 \\ 0 & \frac{16}{45\pi} & 0 \\ 0 & 0 & \frac{16}{45\pi} \end{bmatrix} \tag{1.4}$$

$$[L]=\frac{1}{V}\begin{bmatrix} \frac{1}{2} & 0 & -\frac{15\pi}{64}\sqrt{\frac{1-\sin(\alpha)}{1+\sin(\alpha)}} \\ 0 & \frac{4}{1+\sin(\alpha)} & 0 \\ \frac{15\pi}{64}\sqrt{\frac{1-\sin(\alpha)}{1+\sin(\alpha)}} & 0 & \frac{4}{1+\sin(\alpha)} \end{bmatrix} \tag{1.5}$$

where V is the flow velocity, and α is the skewed angle of the free streamline, changing from 0° to 90°.

One can see from (1.3) that there are three states in this model, and each has a physical meaning. They represent, respectively, uniform flow, a side-to-side gradient, and a fore-to-aft gradient. The theory was verified experimentally, Ref. [3]. At present, it is used in virtually every stability and handling quality application. The limitation for the Pitt-Peters model is that it is a low-order approximation to the rotor induced flow field with only one harmonic and one radial shape function for each harmonic. Thus, the model is only the crudest wake description of uniform flow since its lack of higher-harmonic terms of the flow field.

Due to the limitation of the Pitt-Peters model, researchers desired a higher-harmonic theory which could be more accurate. In 1987, David Peters and Chengjian He developed a higher-harmonic theory, which is known as the Peters-He generalized dynamic wake model, Refs. [4] and [5]. The pressure distribution for the Peters-He model was extended from Pitt's pressure distribution to include higher harmonic terms and arbitrary number of radial functions for each harmonic

$$P=-\frac{1}{2}\sum_{m=0}^{\infty}\sum_{n=m+1,m+3,\cdots}^{\infty}\bar{P}_n^m(\nu)\bar{Q}_n^m(i\eta)\left[\tau_n^{mc}\cos(m\bar{\psi})+\tau_n^{ms}\sin(m\bar{\psi})\right] \tag{1.6}$$

The inflow distribution is expanded to include an arbitrary number of harmonics and radial functions, which is similar as the expression of the pressure

$$v_z=\sum_{m=0}^{\infty}\sum_{n=m+1,m+3,\cdots}^{\infty}\frac{\bar{P}_n^m(\nu)}{\nu}\left[\alpha_n^m\cos(m\bar{\psi})+\beta_n^m\sin(m\bar{\psi})\right] \tag{1.7}$$

where $\bar{P}_n^m(\nu)$ and $\bar{Q}_n^m(i\eta)$ are associated normalized Legendre functions of the first and second kind, respectively. (See Appendix 2)

Both Pitt and He began with the complete potential flow equations and then assumed "superposition of pressures," which implies that inflow modes with no induced velocity on the rotor disk are neglected. As a result, the Peters-He model takes the form

$$[M]\{\overset{+}{\alpha}_n^m\}+V\left[\tilde{L}^c\right]^{-1}\{\alpha_n^m\}=\frac{1}{2}\{\tau_n^{mc}\} \tag{1.8}$$

$$[M]\{\overset{+}{\beta}_n^m\}+V\left[\tilde{L}^s\right]^{-1}\{\beta_n^m\}=\frac{1}{2}\{\tau_n^{ms}\} \tag{1.9}$$

where $\{\alpha_n^m\}$ and $\{\beta_n^m\}$ are the coefficients of the axial induced velocity component on the disk, and $\{\tau_n^{mc}\}$ and $\{\tau_n^{ms}\}$ represent cosine and sine pressure coefficients. The matrix $[M]$ is the apparent mass matrix; and $\left[\tilde{L}^c\right]$ and $\left[\tilde{L}^s\right]$ are the cosine and sine influence coefficient matrices, respectively. These are all given in closed form. The Peters-He model has been validated against wind-tunnel data, Ref. [5]. As a mature dynamic inflow model, Peters-He model is widely used in many production codes including FLIGHTLAB (Advanced Rotorcraft Technology), COPTER (Bell Helicopter) and ONERA-DFVLR (European Community), etc, Ref. [6].

The Peters-He model contains only Legendre functions that have $m+n=odd$ which represents pressure discontinuities at the disk. As the result of discarding the $m+n=even$ terms, which are related to mass-sources, the Peters-He model cannot describe the inflow distribution caused by mass-injection. Further, it treats only the normal component of flow on the rotor disk.

Subsequent researchers have attempted to extend the Peters-He model to include all components of flow throughout the field. In 1996, Wen-Ming Cao and David Peters made an attempt to compute the flow off of the rotor disk as well as on the disk, Ref. [7]. This work demonstrated that there must be a second set of wake

states (besides the He states) for flow off the rotor to be calculated; but it was not known what these states should be.

In 2001, Jorge Morillo and David Peters addressed these issues and showed that the extra states could be found rigorously (with no need for the limiting assumption of superposition of pressures) by writing the velocity field as a gradient of velocity potentials and by including the mass source terms in the expansions, so that the $m+n=odd$ terms and $m+n=even$ terms are all included in the model, Ref. [6].

$$P=-\sum_{m=0}^{\infty}\sum_{n=m+1}^{\infty}\left[\tau_n^{mc}\Phi_n^{mc}+\tau_n^{ms}\Phi_n^{ms}\right] \tag{1.10}$$

$$\vec{v}=\sum_{m=0}^{\infty}\sum_{n=m+1}^{\infty}\left[\hat{a}_n^m\vec{\nabla}\Psi_n^{mc}+\hat{b}_n^m\vec{\nabla}\Psi_n^{ms}\right] \tag{1.11}$$

where Φ_n^m and Ψ_n^m are the pressure and velocity potentials. This set of functions was also used by Pitt and He, but they only considered the odd functions and considered them only for the normal component of velocity. With these definitions, Morillo and Peters were able to use a Galerkin approach to obtain a closed-form set of equations for all three components of the velocity potential—and thus of the velocity field everywhere in the upper hemisphere (i.e., upstream hemisphere)—including the plane of the rotor disk. The governing equations are obtained from this Galerkin procedure in closed form and take the following form:

$$\left[M^c\right]\left\{\overset{*}{a}_n^m\right\}+\left[D^c\right]\left[\tilde{L}^c\right]^{-1}\left[M^c\right]\left\{a_n^m\right\}=\left[D^c\right]\left\{\tau_n^{mc}\right\} \tag{1.12}$$

$$\left[M^s\right]\left\{\overset{*}{b}_n^m\right\}+\left[D^s\right]\left[\tilde{L}^s\right]^{-1}\left[M^s\right]\left\{b_n^m\right\}=\left[D^s\right]\left\{\tau_n^{ms}\right\} \tag{1.13}$$

where $\left[D\right]$ is the damping matrix. All matrices are in closed form, and mass sources are also allowed. The Peters-Morillo model gave excellent agreement with a class of closed-form solutions for step response and frequency response above the rotor disk, but convergence was slow due to ill-conditioned matrices. However, the Peters-Morillo model could not treat non-zero flux mass sources, which are the fundamental mass-source terms (the terms with $m=n$).

In 2005, Ke Yu and David Peters tried to develop an improved state-space representation that included the non-zero mass flux forcing terms, Ref. [8]. They extended the $[D]$ matrix in the right-hand side to incorporate the mass source terms into the governing equation

$$\left[M^c\right]\left\{\overset{*}{a}{}_n^m\right\}+\left(\left[D^c\right]\cos\chi-\left[C^c\right]\sin\chi\right)\left\{a_n^m\right\}=\left[\bar{D}^c\right]\left\{\tau_n^{mc}\right\} \tag{1.14}$$

where $[C]$ is a secondary damping matrix, χ is the inflow angle, and $\left[\bar{D}\right]$ is the extended matrix. However, they were unable to find the potential functions for $m=n$ and consequently still had not added the missing states. Despite the extended $[D]$ matrix, the model was still ill-conditioned and converged slowly.

Hsieh and Peters, Ref. [9], found the here-to-fore illusive potential functions for $m=n$. The special case $m=n=0$ still involved a singularity, but they replaced the infinite integral with an approximate solution for the infinite kinetic energy that converged as the number of terms was increased. Later, Garcia-Duffy and Peters incorporated these into a complete dynamic inflow model for all components of flow in the upper hemisphere—and with good convergence, Ref. [10]. This model with the $m=n$ term will be referred to as the Hsieh/Duffy model.

All of these models are only valid for the flow on or above the plane of the rotor disk. What remains, then, is to find a solution for the flow below the plane of the rotor, and apply the new method to finite blade systems and find the inflow within the wake region.

1.2 Objective and Approach

The aim of this research is to find a model to describe the velocity distribution below the disk. Due to the constraints and limitation of Galerkin approach (that expansion functions must satisfy all boundary conditions), the modified Peters- Morillo model can only be used either on or above the rotor plane. This is because there are discontinuities in the wake across vortex sheets which make it problematical to find a

valid expansion function for velocity in that region. Furthermore, the flow in the wake is literally not potential flow so that no velocity potential exists. Here we will overcome these obstacles by obtaining a closed-form expression for the flow below the plane of the rotor disk in terms of velocities (and adjoint velocities) above the plane.

In the work to be presented in this dissertation, we will start from the exact solution and use the information above the disk to demonstrate by mathematical proof that the complete flow everywhere in the flow field can be developed in closed form from the flow in the upper hemisphere. The cost of this transaction is that one must also compute the adjoint of the velocity (i.e., the co-states of the flow) in the upper hemisphere. Once that is done, then the complete flow below the plane (including inside of the rotor wake) follows directly. If the solution above the disk has converged, then the solution below the disk is guaranteed to converge as well.

After getting the formula for the inflow model below the rotor disk, we will validate the new method for both frequency responses and step responses for axial flow, will compare with the analytical solution to make sure it could be used in both frequency domain and time domain. And then will show the effectiveness of the method for skewed angle flow and apply this method for finite blade system to predict the wake region below the rotor disk. For large skew angels, there must be an optimization of odd and even terms for Hsieh-Duffy model above the rotor disk. Here, for the inflow below the rotor disk, we will similarly try to find the optimized combination of odd and even terms to minimize the error within wake region.

Chapter 2 Inflow Theory Fundamentals

2.1 Fluid Dynamics Equations

The governing equations for Newtonian fluid are based on the basic conservation laws, which include the conservation of mass, the conservation of momentum and the conservation of energy. Each the conservation laws lead to one or a set of differential equations. Together with the equation of states, one can describe the motion of Newtonian fluid, Ref. [11]:

$$\frac{\partial \rho}{\partial t} + \vec{\nabla} \bullet \left(\rho \vec{v}_t \right) = 0 \tag{2.1}$$

$$\rho \frac{\partial \vec{v}_t}{\partial t} + \rho \left(\vec{v}_t \bullet \vec{\nabla} \right) \vec{v}_t = -\vec{\nabla} p + \vec{\nabla} \left(\bar{\lambda} \vec{\nabla} \bullet \vec{v}_t \right) + \bar{\mu} \left(\vec{\nabla} \left(\vec{\nabla} \bullet \vec{v}_t \right) + \left(\vec{\nabla} \bullet \vec{\nabla} \right) \vec{v}_t \right) + \rho \vec{f} \tag{2.2}$$

$$\rho \frac{\partial e}{\partial t} + \rho \left(\vec{v}_t \bullet \vec{\nabla} \right) e = -p \vec{\nabla} \bullet \vec{v}_t + \vec{\nabla} \left(k \vec{\nabla} T \right) + \bar{\Phi} \tag{2.3}$$

$$p = p\left(\rho, T \right) \tag{2.4}$$

$$e = e\left(\rho, T \right) \tag{2.5}$$

where ρ is the fluid density, $\vec{v}_t$ is the total velocity, p is the pressure, $\bar{\lambda}$ and $\bar{\mu}$ are the second viscosity coefficient and the dynamic viscosity respectively, $\vec{f}$ represents the external forces, e is the internal energy per unit mass, k is the thermal conductivity of the fluid, $\bar{\Phi}$ is the viscous dissipation function and T is temperature.

However, for a helicopter, it is reasonable to assume that the inflow at standard atmospheric conditions is incompressible and inviscid around the actuator disk, Ref. [11]. Since there are no significant body forces around an actuator disk, the equations are reduced to the following potential flow equations

$$\vec{\nabla} \bullet \vec{v}_t = 0 \tag{2.6}$$

$$\rho \frac{\partial \vec{v}_t}{\partial t} + \rho \left(\vec{v}_t \bullet \vec{\nabla} \right) \vec{v}_t = -\vec{\nabla} p \tag{2.7}$$

Here, we consider the linearized equations written as a perturbation of velocity about the steady free-stream. The steady free-stream velocity is labeled V_∞. The total velocity is represented by

$$\vec{v}_t = V_\infty \vec{\xi} + \delta\vec{v} \tag{2.8}$$

where $\vec{\xi}$ is a unit vector that is along the free streamline and is skewed with respect to positive z by an angel of χ as shown in Figure 2- 1; and

$$\delta\vec{v} = \delta v_x \vec{i} + \delta v_y \vec{j} + \delta v_z \vec{k} \tag{2.9}$$

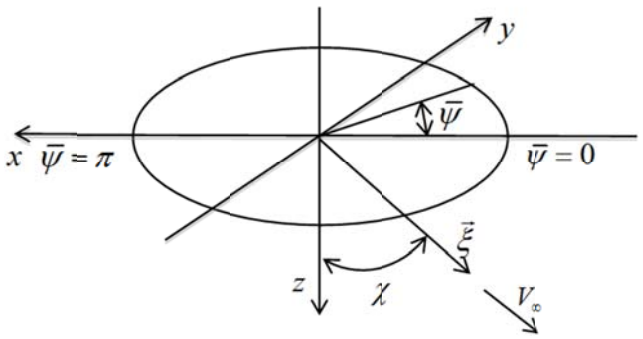

Figure 2-1 Coordinate system

Also, from the coordinates in Figure 2-1, we know that $\vec{\xi}$ can be expressed as

$$\vec{\xi} = -\sin(\chi)\vec{i} + \cos(\chi)\vec{k}$$

where $\vec{i}$, $\vec{j}$ and $\vec{k}$ are unit vectors in x, y and z directions, respectively.

Substitution of these equations into the momentum equations and continuous equation, considering that V_∞ constant, gives linearized equations:

$$\vec{\nabla} \bullet \delta\vec{v} = 0 \tag{2.10}$$

$$\rho \frac{\partial \delta\vec{v}}{\partial t} + \rho V_\infty \frac{\partial \delta\vec{v}}{\partial \xi} = -\vec{\nabla} p \tag{2.11}$$

To normalize the variables, all lengths are divided by the rotor radius R; and the velocities are all divided by V_∞. Therefore, equations (2.10)-(2.11) in can be rewritten as

$$\vec{\nabla} \bullet \vec{v} = 0 \tag{2.12}$$

$$\frac{\partial \vec{v}}{\partial \tau} + \frac{\partial \vec{v}}{\partial \xi} = -\vec{\nabla} P \tag{2.13}$$

where we have defined P as normalized pressure $p/\rho V_\infty^2$, $\vec{v}$ as normalized induced velocity $\delta\vec{v}/V_\infty$ and time as a reduced time τ, which is tV_∞/R; and where the Laplacian operator is redefined as the gradient with respect to nondimensional coordinates. The boundary condition in the upper hemisphere is that velocity $\vec{v}$ must be zero in all directions far upstream.

Suppose $\vec{v}$ can be represented by the gradient of some function, Ψ, then we may write

$$\vec{v} = \vec{\nabla}\Psi \tag{2.14}$$

Then it is clear from equation (2.12) that Ψ will be a potential function and will satisfy Laplace's equation

$$\vec{\nabla} \bullet \vec{\nabla}\Psi = 0 \tag{2.15}$$

Substitution of this velocity potential in equation (2.14) into equation (2.13), followed by a divergence operation to the resultant equation, gives:

$$\frac{\partial \vec{\nabla} \bullet \vec{\nabla}\Psi}{\partial \tau} + \frac{\partial \vec{\nabla} \bullet \vec{\nabla}\Psi}{\partial \xi} = -\vec{\nabla} \bullet \vec{\nabla} P \tag{2.16}$$

Based on equation (2.15), the left hand side of equation (2.16) is equal to 0, so if we define

$$\Phi = P \tag{2.17}$$

Then we know Φ satisfies Laplace's equation

$$\vec{\nabla} \bullet \vec{\nabla}\Phi = 0 \tag{2.18}$$

which implies that Φ is also a potential function, as it is actually related to pressure, so we call it pressure potential. Solution of equations (2.15) or (2.18) will yield a family of functions in terms of which we may expand both Ψ and Φ.

2.2 Pressure Potentials

In order to write the equations, we expand the pressure in terms of potential functions which satisfy Laplace equations. As discontinuities in pressure only occur across the disk, we choose the solutions to Laplace equations in ellipsoidal coordinates to reconstruct the pressures in the flow field. (See in Appendix 2) The pressure potential then could be expressed as

$$\Phi_n^{mc}\left(\nu,\eta,\bar{\psi}\right)=\bar{P}_n^m\left(\nu\right)\bar{Q}_n^m\left(i\eta\right)\cos\left(m\bar{\psi}\right) \tag{2.19}$$

$$\Phi_n^{ms}\left(\nu,\eta,\bar{\psi}\right)=\bar{P}_n^m\left(\nu\right)\bar{Q}_n^m\left(i\eta\right)\sin\left(m\bar{\psi}\right) \tag{2.20}$$

where ν, η and $\bar{\psi}$ are the ellipsoidal coordinates defined in Appendix 1 and m takes values from $\{0,1,2,3,4,\ldots\}$ and n is from $\{m,m+1,m+2,m+3,\ldots\}$.

This choice not only satisfies the boundary conditions but also contains both odd terms and even terms, which are capable for describing pressure discontinuities and mass injections anywhere on the rotor disk. In the plane of the rotor disk but off the disk $\nu=0$, the functions with $m+n=odd$ ($\bar{P}_n^m\left(\nu\right)$ are odd functions) are zero. For $m+n=even$ ($\bar{P}_n^m\left(\nu\right)$ are even functions), the pressure potential has normal derivatives on that plane. One can also see from Figure A1.1 that $0<\nu<1$ above the disk while $-1<\nu<0$ below the disk. Since there is a jump in ν across the disk, this implies a jump in Φ. On the disk, $\eta=0$ such that the $m+n=odd$ potentials can be used to describe a pressure jump of the system; and $m+n=even$ potentials (which have a discontinuity in slope) can be used to represent a mass source in the flow field.

The pressure can be expanded as a summation of all the pressure potential terms as

$$P=-\sum_{m=0}^{\infty}\sum_{n=m}^{\infty}\left(\tau_n^{mc}\Phi_n^{mc}+\tau_n^{ms}\Phi_n^{ms}\right) \tag{2.21}$$

The pressure drop and the injected mass across the disk could be expressed by the flowing equations

$$\Delta P = \left[P_{lower} - P_{upper} \right]\Big|_{\eta=0} = 2\sum_{m=0}^{\infty} \sum_{n=m+1,m+3,\cdots}^{\infty} \left(\tau_n^{mc} \Phi_n^{mc} + \tau_n^{ms} \Phi_n^{ms} \right)\Big|_{\eta=0} \tag{2.22}$$

$$\frac{\Delta \dot{m}}{\rho V_\infty} = \left[P_{lower} + P_{upper} \right]\Big|_{\eta=0} = 2\sum_{m=0}^{\infty} \sum_{n=m,m+2,\cdots}^{\infty} \left(\tau_n^{mc} \Phi_n^{mc} + \tau_n^{ms} \Phi_n^{ms} \right)\Big|_{\eta=0} \tag{2.23}$$

where ΔP is the net pressure drop across the disk going from negative to positive z, and $\Delta \dot{m}$ is the net mass per unit time per unit area being injected into the flow field at the disk.

2.3 Velocity Potentials

There are useful definitions of velocity potentials. One set are defined as the prime potentials and the other set are derived potentials. In order to satisfy the upstream boundary condition, the prime potentials are defined as

$$\Psi_n^{mc} = \int_{-\infty}^{\xi} \Phi_n^m \cos\left(m\bar{\psi} \right) d\xi \tag{2.24}$$

$$\Psi_n^{ms} = \int_{-\infty}^{\xi} \Phi_n^m \sin\left(m\bar{\psi} \right) d\xi \tag{2.25}$$

As we know $\lim_{\eta \to \infty} \bar{Q}_n^m \left(i\eta \right) = 0$, so it is guaranteed that the definition of the prime potential will satisfy the boundary condition that the velocity field far upstream from the rotor is equal to zero. Then the flow velocities can be written as

$$\vec{v} = \sum_{m=0}^{\infty} \sum_{n=m}^{\infty} \left(\hat{a}_n^m \vec{\nabla} \Psi_n^{mc} + \hat{b}_n^m \vec{\nabla} \Psi_n^{ms} \right) \tag{2.26}$$

Substitution of equations (2.24) and (2.25) into (2.26), noticing that $\hat{\Psi}_n^{mc}$, $\hat{\Psi}_n^{ms}$, Φ_n^{mc} and Φ_n^{ms} are only functions of nondimensional coordinates and $\hat{a}_n^m$, $\hat{b}_n^m$, τ_n^{mc} (and that the τ_n^{ms} are only functions of reduced time τ) gives:

$$\sum_{m=0}^{\infty} \sum_{n=m}^{\infty} \left(\vec{\nabla} \Psi_n^{mc} \frac{\partial \hat{a}_n^m}{\partial \tau} + \vec{\nabla} \frac{\partial \Psi_n^{mc}}{\partial \xi} \hat{a}_n^m \right) = \sum_{m=0}^{\infty} \sum_{n=m}^{\infty} \left(\vec{\nabla} \Phi_n^{mc} \tau_n^{mc} \right) \tag{2.27}$$

$$\sum_{m=0}^{\infty} \sum_{n=m}^{\infty} \left(\vec{\nabla} \Psi_n^{ms} \frac{\partial \hat{b}_n^m}{\partial \tau} + \vec{\nabla} \frac{\partial \Psi_n^{ms}}{\partial \xi} \hat{b}_n^m \right) = \sum_{m=0}^{\infty} \sum_{n=m}^{\infty} \left(\vec{\nabla} \Phi_n^{ms} \tau_n^{ms} \right) \tag{2.28}$$

There are no closed form expressions for these prime velocity potentials at arbitrary skew angles. Therefore, one must do preprocessing to calculate the gradients of Ψ_n^m at points in the flow field in order to calculate the velocity. This can be accomplished by integration of the potentials along the streamlines, which is time consuming.

The derived potentials, $\hat{\Psi}_n^m$, are defined as the prime potentials for the special case of axial flow. These can be found in closed form and thus avoid any numerical integration for calculating the induced velocity components. Their disadvantage is that the ξ derivative in the potential flow equations is more complicated for these. Peters and Morillo found the derived potentials (for $m \neq n$) in the following form:

$$\hat{\Psi}_n^m = \sigma_n^m \Phi_{n+1}^m + \varsigma_n^m \Phi_{n-1}^m \tag{2.29}$$

where

$$\sigma_n^m = \frac{1}{K_n^m \sqrt{(2n+1)(2n+3)\left[(n+1)^2 - m^2\right]}} \tag{2.30}$$

$$\varsigma_n^m = \frac{1}{K_n^m \sqrt{(4n^2-1)(n^2-m^2)}} \qquad n \neq m \tag{2.31}$$

and

$$K_n^m = \left(\frac{\pi}{2}\right)^{(-1)^{n+m}} H_n^m \tag{2.32}$$

$$H_n^m = \frac{(n+m+1)!!(n-m-1)!!}{(n+m)!!(n-m)!!} \tag{2.33}$$

This definition is only valid above the rotor disk ($n > m$). For the case when $m = n \neq 0$, Peters and Hsieh developed a formulation for the potentials in terms of an alternate type of "Legendre function" with subscript greater than superscript:

$$\hat{\Psi}_m^{mc} = \left[\sigma_m^m \bar{P}_{m+1}^m(\nu)\bar{Q}_{m+1}^m(i\eta) + \bar{P}_{m-1}^m(\nu)\bar{Q}_{m-1}^m(i\eta)\right]\cos(m\bar{\psi}) \tag{2.34}$$

$$\hat{\Psi}_m^{ms} = \left[\sigma_m^m \bar{P}_{m+1}^m(\nu)\bar{Q}_{m+1}^m(i\eta) + \bar{P}_{m-1}^m(\nu)\bar{Q}_{m-1}^m(i\eta)\right]\sin(m\bar{\psi}) \tag{2.35}$$

where

$$\bar{P}_{m-1}^{m}(\nu)=\frac{2}{\pi}\frac{\sqrt{(2m)!!}}{\sqrt{(2m+1)!!}}\frac{\left(1-\nu^2\right)^{m/2}}{(1+\nu)^m}\sum_{n=0}^{m-1}\frac{(m-1)!2^{m-1-n}(-1)^n}{n!(m-1-n)!(n+m)}(1-\nu)^n \qquad (2.36)$$

$$\bar{Q}_{m-1}^{m}(i\eta)=\frac{1}{\left(1+\eta^2\right)^{m/2}} \qquad (2.37)$$

Even here, however, the case for $m=n=0$ is singular. By solving the Laplace equation with $m=n=0$ and then adding a line singularity (which is not obtainable by separation of variables), Peters and Hsieh were able to find the $m=n=0$ derived velocity potential as

$$\hat{\Psi}_0^0=\frac{2}{\pi}\nu\left[1-\eta\tan^{-1}\left(\frac{1}{\eta}\right)\right]-\frac{2}{\pi}\ln|1+\nu|-\frac{1}{\pi}\ln\left|1+\eta^2\right|+\frac{2}{\pi}\ln|Z_{\max}| \qquad \nu>0 \qquad (2.38)$$

where $Z_{\max}$ is a large number representing the radius to which the ξ integral is taken. When the potential is evaluated at infinity, the last term cancels the logarithmic terms—so that the potential is zero at $Z_{\max}$. Of course, this additional constant has no effect on the velocity field because one needs only the gradients of the potential functions to obtain velocity. This large number $Z_{\max}$ will, however, affect the Galerkin integrals to be derived in the following section so that this logarithmic constant will need to be dealt with. (Derived velocity potentials are not defined below the rotor plane.)

As the velocity potentials all satisfy Laplace's equation, so the continuity equation in (2.12) will be satisfied simultaneously. That means it is sufficient to consider only the momentum equation as a governing equation for the velocity expansion coefficients. Thus, to obtain a finite-state wake model is equivalent to solve the problem of representing the momentum equations in finite-state form.

2.4 Galerkin Method

In order to transform the momentum equation into a set of ordinary differential equations, the Galerkin Method is adopted here in which velocities are expanded in terms of the prime potentials. (Derived potentials will be considered later.) The test

functions for the Galerkin method are chosen to be the same Laplace solutions that are used as expansions for the pressure potentials. Since the velocity potentials are only defined in the upper hemisphere, the integrations will be done in the upper hemisphere, and all boundary conditions are matched. As the integration is only considered over the upper hemisphere, the velocity solution will only be valid above the disk.

After substitution of the proper expansions of pressure potentials, velocity potentials, and the expression of velocity into the momentum equation, volume integration is taken on both sides of the momentum equations. With the divergence theorem, we can then transfer the volume integral into a surface integral, which vanishes at $r \to \infty$. By the method shown in Ref. [5], the surface integral in the plane of the rotor is transformed to integrals on the rotor disk, itself, which have closed-form representations. This leads to a set of ordinary differential equations. The cosine and sine functions completely separate into two uncoupled sets during this procedure. For the cosine parts, the Galerkin method gives:

$$\begin{bmatrix} \left[\tilde{L}^c\right]_{o,o} & \left[\tilde{L}^c\right]_{o,e} \\ \left[\tilde{L}^c\right]_{e,o} & \left[\tilde{L}^c\right]_{e,e} \end{bmatrix} \begin{Bmatrix} \overset{*}{\left\{\hat{a}_n^m\right\}_o} \\ \overset{*}{\left\{\hat{a}_n^m\right\}_e} \end{Bmatrix} + \begin{bmatrix} [D]^c_{o,o} & [D]^c_{o,e} \\ [D]^c_{e,o} & [D]^c_{e,e} \end{bmatrix} \begin{Bmatrix} \left\{\hat{a}_n^m\right\}_o \\ \left\{\hat{a}_n^m\right\}_e \end{Bmatrix} = \begin{bmatrix} [D]^c_{o,o} & [D]^c_{o,e} \\ [D]^c_{e,o} & [D]^c_{e,e} \end{bmatrix} \begin{Bmatrix} \left\{\tau_n^{mc}\right\}_o \\ \left\{\tau_n^{mc}\right\}_e \end{Bmatrix} \tag{2.39}$$

where

$$\left[\tilde{L}^c\right] = \left[\iint_s \frac{\partial \Phi_j^{rc}}{\partial z} \left(\int_0^\infty \Phi_n^{mc} d\xi \right) ds \right] = \left[\iint_s \Phi_j^{rc} \frac{\partial}{\partial z} \left(\int_0^\infty \Phi_n^{mc} d\xi \right) ds \right] \tag{2.40}$$

$$\left[D^c\right] = \left[\iint_s \frac{\partial \Phi_j^{rc}}{\partial z} \Phi_n^{mc} ds \right] = \left[\iint_s \Phi_j^{rc} \frac{\partial \Phi_n^{mc}}{\partial z} ds \right] \tag{2.41}$$

The sine components are similar to equation (2.39). Note that the subscript notation "o" stands for the terms with $m+n=odd$ and "e" is for the terms with $m+n=even$. For the cosine terms, $m=0,1,2,3,\ldots$ and for the sine terms $m=1,2,3,\ldots$, since

$$\Phi_n^{ms} = \bar{P}_n^{ms}(\nu)\bar{Q}_n^{ms}(i\eta)\sin(m\bar{\varphi}) \tag{2.42}$$

which implies that when $m=0$, $\Phi_n^{ms}=0$. In either the case of sine terms or cosine terms, $n=m,m+2,m+4,\ldots$ or $n=m+1,m+3,m+5,\ldots$ depending on the subscript of the partition is "e" or "o".

The $[D]$ matrix is as follows for both cosine and sine case:

$$D_{jn}^{rm} = \frac{1}{K_n^m}\delta_{jn}\delta_{rm}$$
$$j+r=odd; \qquad n+m=odd \tag{2.43}$$
$$j+r=even; \qquad n+m=even$$

$$D_{jn}^{rm} = \frac{2\delta_{nm}}{\pi\sqrt{H_n^m H_j^m}}\frac{\sqrt{(2j+1)(2n+1)}}{(j+n+1)(j-n)}(-1)^{\frac{j+3n-1}{2}}$$
$$j+r=odd; \qquad n+m=even \tag{2.44}$$
$$j+r=even; \qquad n+m=odd$$

And the $\left[\tilde{L}\right]$ matrix is given by

$$\left[\tilde{L}_{jn}^{0m}\right]^c = X^m\Gamma_{jn}^{0m} \tag{2.45}$$

$$\left[\tilde{L}_{jn}^{rm}\right]^c = \left[X^{|m-r|} + (-1)^l X^{|m-r|}\right]\Gamma_{jn}^{rm} \tag{2.46}$$

$$\left[\tilde{L}_{jn}^{rm}\right]^s = \left[X^{|m-r|} - (-1)^l X^{|m-r|}\right]\Gamma_{jn}^{rm} \tag{2.47}$$

where

$$X = \tan(\chi/2), \qquad l = \min(r,m) \tag{2.48}$$

$$\Gamma_{jn}^{rm} = \frac{sign(r-m)}{\sqrt{K_n^m K_j^r}\sqrt{(2n+1)(2j+1)}}\delta_{j,n\pm1}$$
$$r+m=odd; \qquad j+r=odd; \qquad n+m=odd \tag{2.49}$$
$$r+m=odd; \qquad j+r=even; \qquad n+m=even$$

$$\Gamma_{jn}^{rm} = \frac{(-1)^{\frac{n+j-2r}{2}}(2)\sqrt{(2n+1)(2j+1)}}{\sqrt{H_n^m H_j^r}(n+j)(n+j+2)\left[(n-j)^2-1\right]} \tag{2.50}$$
$$r+m=even; \qquad j+r=odd; \qquad n+m=odd$$

$$\Gamma_{jn}^{rm} = \frac{(-1)^{\frac{n+j-2r+2}{2}}(8)\sqrt{(2n+1)(2j+1)}}{\pi^2\sqrt{H_n^m H_j^r}\,(n+j)(n+j+2)\left[(n-j)^2-1\right]} \tag{2.51}$$

$$r+m=even; \qquad j+r=even; \qquad n+m=even$$

$$\Gamma_{jn}^{rm} = \frac{(-1)^{\frac{3n+j+2m-2r}{2}}(4)\,sign(r-m)\sqrt{(2n+1)(2j+1)}}{\pi\sqrt{H_n^m H_j^r}\,(n+j)(n+j+2)\left[(n-j)^2-1\right]} \tag{2.52}$$

$$r+m=odd; \qquad j+r=odd; \qquad n+m=even$$

$$r+m=odd; \qquad j+r=even; \qquad n+m=odd$$

$$\Gamma_{jn}^{rm} = \frac{1}{\sqrt{H_n^m H_j^r}\sqrt{(2n+1)(2j+1)}}\delta_{j,n\pm1} \tag{2.53}$$

$$j+m=even; \qquad j+r=odd; \qquad n+m=even$$

$$j+m=even; \qquad j+r=even; \qquad n+m=odd$$

The potential for $m=n=0$, has a logarithmic term, so the integral for Γ is formally infinite for the case of $m=r=n=j=0$. However, based on Ref. [4], we can express this integral as a finite series that approaches infinity as the number of terms approaches infinity.

$$\Gamma_{00}^{00} = \left(\frac{4}{\pi^2}\sum_{n=1}^{N_{\max}}\frac{1}{n}\right)+\frac{1}{2} \tag{2.54}$$

where $N_{\max}$ is the largest harmonic number. In this way, the integral is finite for a truncated approximation. This also allows a solution with a finite number of terms that provides formal convergence to the exact answer.

2.5 Equations in Terms of Derived Potentials

In the last section, a closed form representation of the dynamic equations is shown for the velocity potential expansions in terms of prime potentials. However, since the limitation of prime potential, we would like to write the velocity in terms of derived potentials. In order to do this, we need to change variables which relate the two sets

of basis functions over the upper hemisphere. In particular, the total velocity potential is could be written as

$$\left\{\hat{a}_n^m\right\}^T\left[\Psi_n^{mc}\right]=\left\{a_n^m\right\}^T\left\{\sigma_n^m\Phi_{n+1}^{mc}+\varsigma_n^m\Phi_{n-1}^{mc}\right\} \tag{2.55}$$

When a Galerkin approach is applied to equation (2.55), then the following relationship is found

$$\left\{\hat{a}_n^m\right\}=\left[\tilde{L}^c\right]^{-1}\left[M^c\right]\left\{a_n^m\right\} \tag{2.56}$$

where

$$\left[M^c\right]=\left[\tilde{L}^c\right]_{\chi=0}=\left[\iint_s\frac{\partial\Phi_j^{rc}}{\partial z}\Psi_n^{mc}ds\right] \tag{2.57}$$

A similar transformation therefore exists between $\left\{\hat{b}_n^m\right\}$ and $\left\{b_n^m\right\}$ that involves $\left[L^s\right]$ and $\left[M^s\right]$, which relates to sine coefficients. With this transformation of variables, the equation of motion for a skewed flow becomes

$$\left[M^c\right]\left\{\overset{*}{a}_n^m\right\}+\left[D^c\right]\left[L^c\right]^{-1}\left[M^c\right]\left\{a_n^m\right\}=\left[D^c\right]\left\{\tau_n^{mc}\right\} \tag{2.58}$$

The equation in equation (2.58) is a closed form expression for all components of the velocity above and on the rotor plane.

For the special case of axial flow ($\chi=0$), $\left[\tilde{L}^c\right]$ and $\left[M^c\right]$ are equivalent. So the momentum equation could be simplified as

$$\left[M^c\right]\left\{\overset{*}{a}_n^m\right\}+\left[D^c\right]\left\{a_n^m\right\}=\left[D^c\right]\left\{\tau_n^{mc}\right\} \tag{2.59}$$

Chapter 3 States and Mode Shapes

The Hsieh/Duffy model has never before been analyzed to find its modes and eigenvalues. Therefore, before proceed to flow below the disk, we first perform such an analysis.

3.1 Inflow Mode Shape Analysis

In order to study the characteristics of unsteady aerodynamics in forward flight, we first consider the homogeneous equations for the inflow wake model. Then the cosine and sine part of the homogenous motion equations could be reduced from (2.58) to the following equations

$$\left[M^c\right]\left\{\overset{*}{a_n^m}\right\}+\left[D^c\right]\left[\tilde{L}^c\right]^{-1}\left[M^c\right]\left\{a_n^m\right\}=\{0\} \tag{3.1}$$

$$\left[M^s\right]\left\{\overset{*}{b_n^m}\right\}+\left[D^s\right]\left[\tilde{L}^s\right]^{-1}\left[M^s\right]\left\{b_n^m\right\}=\{0\} \tag{3.2}$$

If we assume the eigensolution to the homogenous equations (3.1) and (3.2) are in the form of $\{\phi_c\}e^{\zeta_c\tau}$ and $\{\phi_s\}e^{\zeta_s\tau}$, then in order to obtain all the eigenvalues ζ_c and ζ_s, one needs only to solve

$$\left|\left[M^c\right]^{-1}\left[D^c\right]\left[\tilde{L}^c\right]^{-1}\left[M^c\right]-\zeta_c\left[I\right]\right|=0 \tag{3.3}$$

$$\left|\left[M^s\right]^{-1}\left[D^s\right]\left[\tilde{L}^s\right]^{-1}\left[M^s\right]-\zeta_s\left[I\right]\right|=0 \tag{3.4}$$

As we know, each eigenvector can be multiplied by an arbitrary constant. For the purposes of consistency, we normalize the eigenvectors so that the mode shapes will be unique.

Typically, there are several ways of normalization, Ref. [12]. Below is the methodology used in this dissertation. Since the procedure is quite similar, for either cosine or sine modes, we demonstrate eigenvalues and normalization on only the cosine modes. Suppose the mode shape is $\{\phi_c\}$, and the maximum absolute value of all the f^{th} element in the eigenvector is defined as:

$$\phi_{\max} = \max\left\{\left|\phi_c\right|_f\right\} \tag{3.5}$$

Then scale this f^{th} element in the eigenvector to be 1, we will have normalized eigenvector $\left\{\overline{\phi}_c\right\}$.

3.2 Results for Eigenvalues

In this section, we will show some results for eigenvalues first. For convenience in comparing with [13], we will consider an 8-harmonic case first.

Ref. [13] considers the He model in which only $n+m=odd$ terms are included in the expansion. For a maximum harmonic of $N_{\max}$, there are $\left(N_{\max}+1\right)\left(N_{\max}+2\right)/2$ sates in this model. For the Hsieh/Duffy model, on the other hand, all values of m and n are considered; and, therefore, there are roughly twice the number of states. For example, a case of 8 harmonics, the He model has 45 states (25 cosine and 20 sine). The Hsieh/Duffy model, however, has 94 states (52 cosine and 42 sine). This is because the Hsieh/Duffy model has eigenvalues corresponding to mass sources. For every harmonic, one of these mass-source eigenvalues becomes more and more sluggish as the number of terms is increased and become static in the limit as $N_{\max}$ approaches infinity. These low-order eigen modes will not be shown on the plots.

Figure 3-1 presents the real parts of the cosine eigenvalues—versus skew angle—for the case of 8 harmonics. This shows the heavy damping of dynamic inflow modes. Figure 3-2 gives the imaginary parts of the eigenvalues. Note that there is a set of critical skew angles at which two different real eigenvalues coalesce with each other and split into a complex-conjugate pair—giving an imaginary part—indicating an oscillating decay. The frequency generally increases with skew angle but can also peak and start to diminish in some cases. The eigenvectors show that the modes are highly coupled especially with larger skew angles.

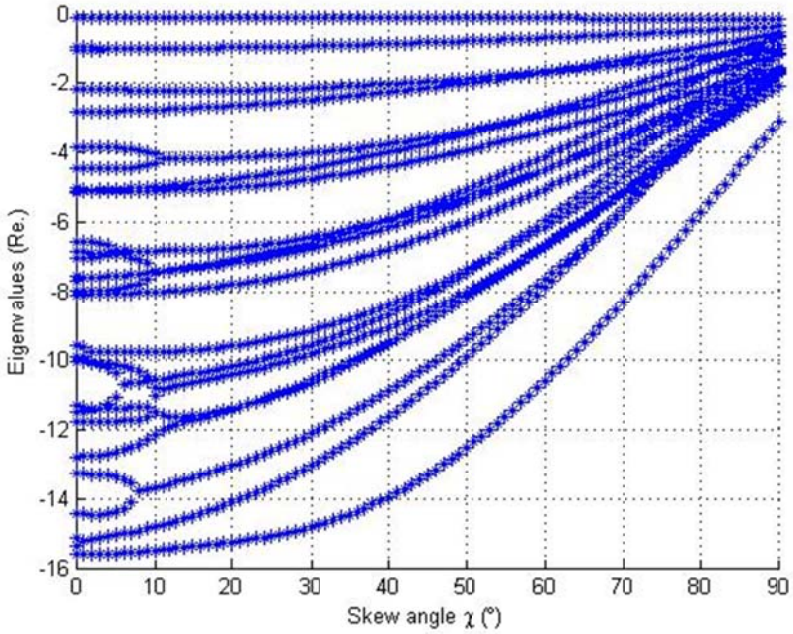

Figure 3-1 Inflow eigenvalue vs. different skew angle (cos, real part)

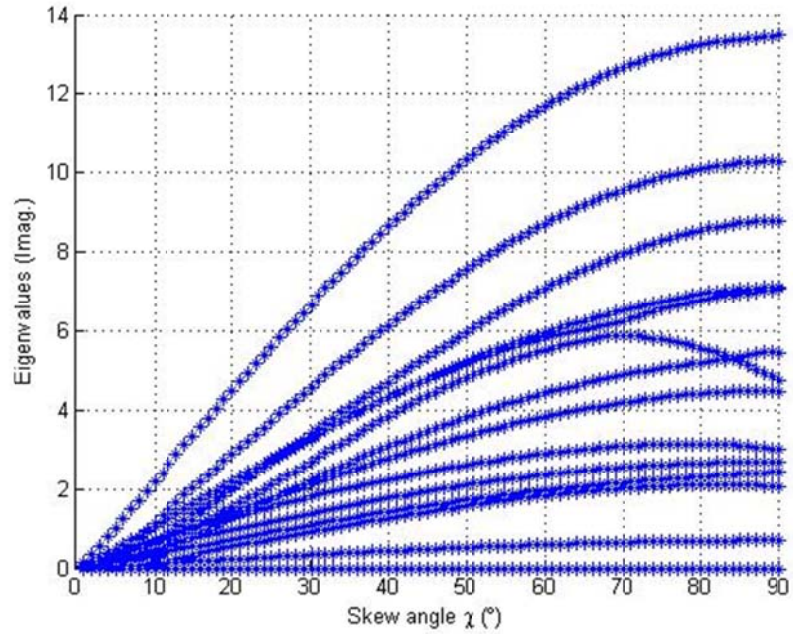

Figure 3-2 Inflow eigenvalue vs. different skew angle (cos, imag. part)

For the sine modes, we follow the procedure for cosine part. The real and imaginary parts of the first 24 eigenvalues are shown in Figure 3-3 and Figure 3-4.

Even though there should be 50 states for both cosine and sine harmonics, some of the eigenvalues are really small, which means the affections of such eigenvalues are neglectable, so we omit these ones and choose the former ones to show. From Figure 3-1 to Figure 3-4, we can tell some eigenvalues coupled with others if the skew angle is bigger than some specific values. As we know the smaller the real part is, the quicker the influence will die out; the bigger the imaginary part is, the stronger the oscillation could be. So from these four figures, we can tell that with $\chi = 0^o$, which is axial flow case, the eigenvalues are uncoupled with each other, and there will be no oscillations, but for the edgewise flow case, which means $\chi = 90^o$, the oscillation will be the worst for all the skew angles.

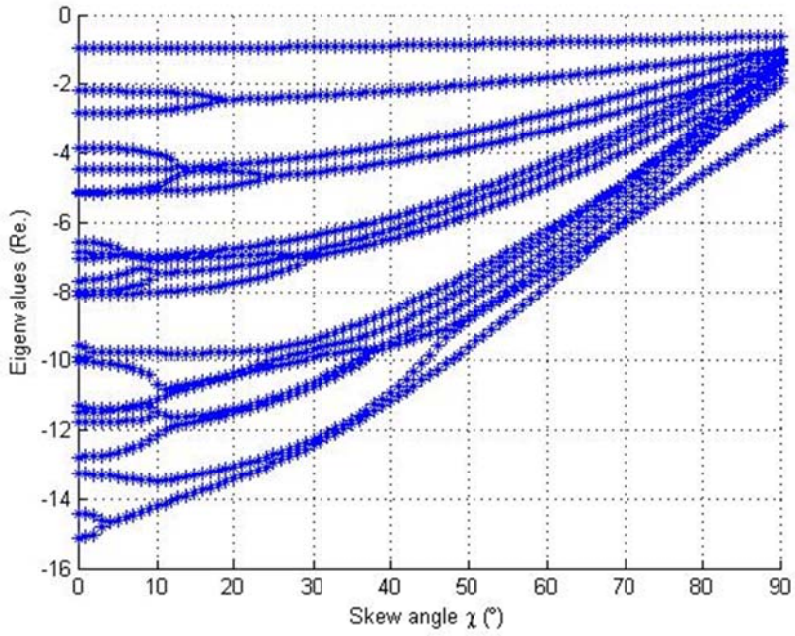

Figure 3-3 Inflow eigenvalue vs. different skew angle (sin, real. part)

The eigenvalue distribution completely determines the rotor dynamics. For simplification, we only consider responses due to the eigenvalues for a helicopter in climb—which implies the skew angle equals to 0. In axial flow, the harmonics are uncoupled with each other, so we can calculate and record them separately. It is known that $\left[M^c\right] = \left[\tilde{L}^c\right]$, $\left[M^s\right] = \left[\tilde{L}^s\right]$ while $\chi = 0^o$. Then Equations (3.3) and (3.4) could be rewritten as

$$\left|\left[M^c\right]^{-1}\left[D^c\right]-\zeta_c\left[I\right]\right|=0 \tag{3.6}$$

$$\left|\left[M^s\right]^{-1}\left[D^s\right]-\zeta_s\left[I\right]\right|=0 \tag{3.7}$$

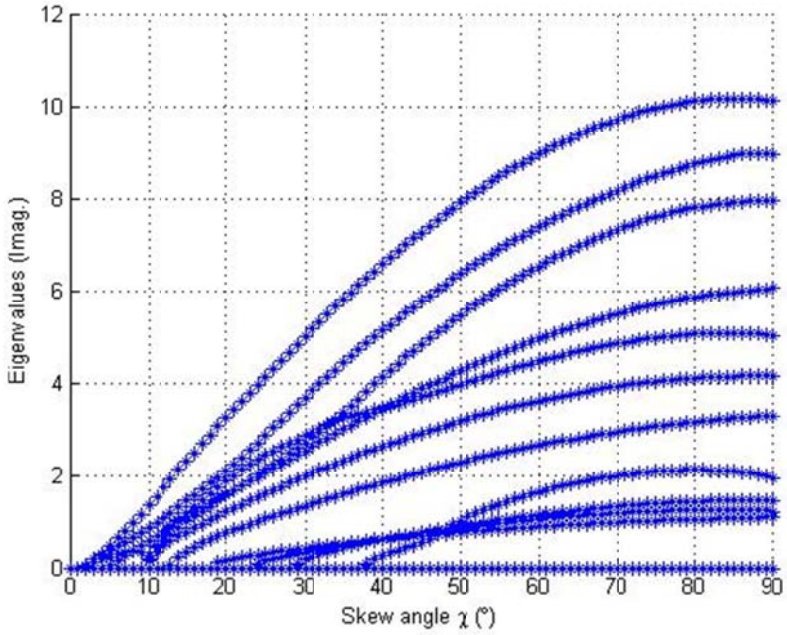

Figure 3-4 Inflow eigenvalue vs. different skew angle (sin, imag. part)

We use the indices for coefficients a_n^m and b_n^m to label the eigenvalues, then we can compare the eigenvalues for the Peters-He model as listed in Table 3.1. The eigenvalues for the Hsieh/Duffy model are listed in Table 3.2.

From Table 3.1 and Table 3.2, we can tell that the eigenvalues for sine part are the same as the eigenvalues for the cosine part with the exclusion of $m=0$.

As the block for $m=0$ is uncoupled with other blocks for $\chi=0$, and $\left[M^s\right]$ and $\left[D^s\right]$ are the same with $\left[M^c\right]$ and $\left[D^c\right]$ exclude $m=0$ terms, so the eigenvalues are the same for the rest value of m. In the following, we calculate eigenvalues for 12 Harmonic numbers, and the records for cosine part are shown in Table 3.3 and Table 3.4.

Table 3.1 Eigenvalues for Peters-He dynamic inflow model

(cos and sin parts, 8 Harmonics)

n / m	cosine					sine		
	0	1	2	3	4	2	3	4
0	--	-2.006	--	-5.125	--	--	--	--
1	--	--	-3.453	--	-6.632	-3.453	--	-6.632
2	--	--	--	-4.768	--	--	-4.768	--
3	--	--	--	--	-6.021	--	--	-6.021
4	--	--	--	--	--	--	--	--

Table 3.2 Eigenvalues for Hsieh/Duffy dynamic inflow model

(cos and sin parts, 8 Harmonics)

n / m	cosine					sine		
	0	1	2	3	4	2	3	4
0	-0.137	-1.061	-2.807	-5.036	-7.554	--	--	--
1	--	-0.970	-2.842	-5.178	-7.673	-0.970	-2.842	-5.178
2	--	--	-2.188	-4.487	-7.041	--	-2.188	-4.487
3	--	--	--	-3.840	-6.556	--	--	-3.840
4	--	--	--	--	-5.106	--	--	--

Comparing Table 3.1 and Table 3.3, we find that the eigenvalues change slightly. This slight change is due to the fact that the number of radial terms in each harmonic is limited by the highest harmonic of interest. Therefore, changing maximum $N_{\max}$ changes the number of expansion terms in each series. On the other hand, a comparison of Table 3.2 and Table 3.4 shows that the lowest eigenvalues are quite different. This is because that eigenvalue is tending to zero as $N_{\max}$ approaches infinity.

Table 3.3 Eigenvalues for Peters-He dynamic inflow model

(cos parts, 12 Harmonics)

n / m	cosine				
	0	1	2	3	4
0	--	-2.006	--	-5.125	--
1	--	--	-3.453	--	-6.627
2	--	--	--	-4.768	--
3	--	--	--	--	-6.020
4	--	--	--	--	--

Table 3.4 Eigenvalues for Hsieh/Duffy dynamic inflow model

(cos part, 12 Harmonics)

n / m	cosine				
	0	1	2	3	4
0	-0.098	-0.783	-2.172	-4.065	-6.288
1	--	-0.702	-2.174	-4.155	-6.453
2	--	--	-1.696	-3.634	-5.888
3	--	--	--	-3.094	-5.515
4	--	--	--	--	-4.288

The eigenvalues of Peters-He dynamic inflow model in hover follow a definite pattern. By regression, we can find the distribution could be described by the following equation:

$$\zeta = \frac{7}{16} + \frac{25}{16} n - \frac{11}{48} m \tag{3.8}$$

3.3 Mode Shapes for Axial Flow

In this section, we will talk about the mode shapes for the Hsieh/Duffy model. In order to identify each mode with different skew angles, we will calculate the

eigenvectors first. Here, we only show the real parts the of mode shapes, the imaginary parts could be obtained follow the same step. The mode shapes of the inflow velocity for cosine harmonics will be defined as

$$\vec{v} = \sum_{m=0}^{\infty} \sum_{n=m}^{\infty} \left[\bar{\phi}_{nc}^{m} \bar{P}_{n}^{m} \bar{Q}_{n}^{m} \cos\left(m\bar{\psi}\right) \right] \tag{3.9}$$

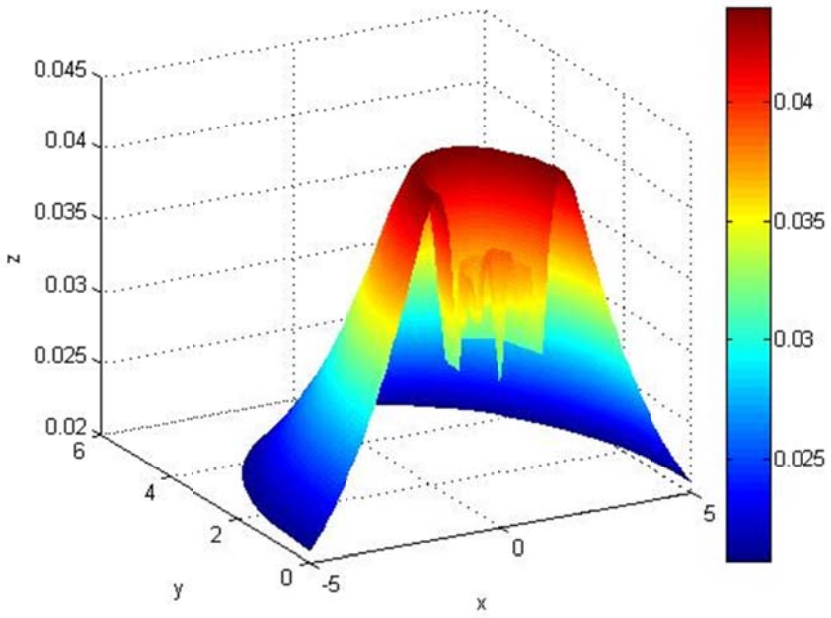

Figure 3-5 The first mode shape of Hsieh/Duffy model

The lowest eigenvalue mode is shown in Figure 3-5, which is axisymmetric in axial flow. There are no nodes in this mode, which makes it the fundamental mode. Some induced flow mode shapes contour plots with node lines are shown in Figure 3-6 to Figure 3-9 at some specific angles for cosine harmonics. Here we only choose $\chi = 0^{o}, 30^{o}, 60^{o}, 90^{o}$ to show what these mode shapes are like.

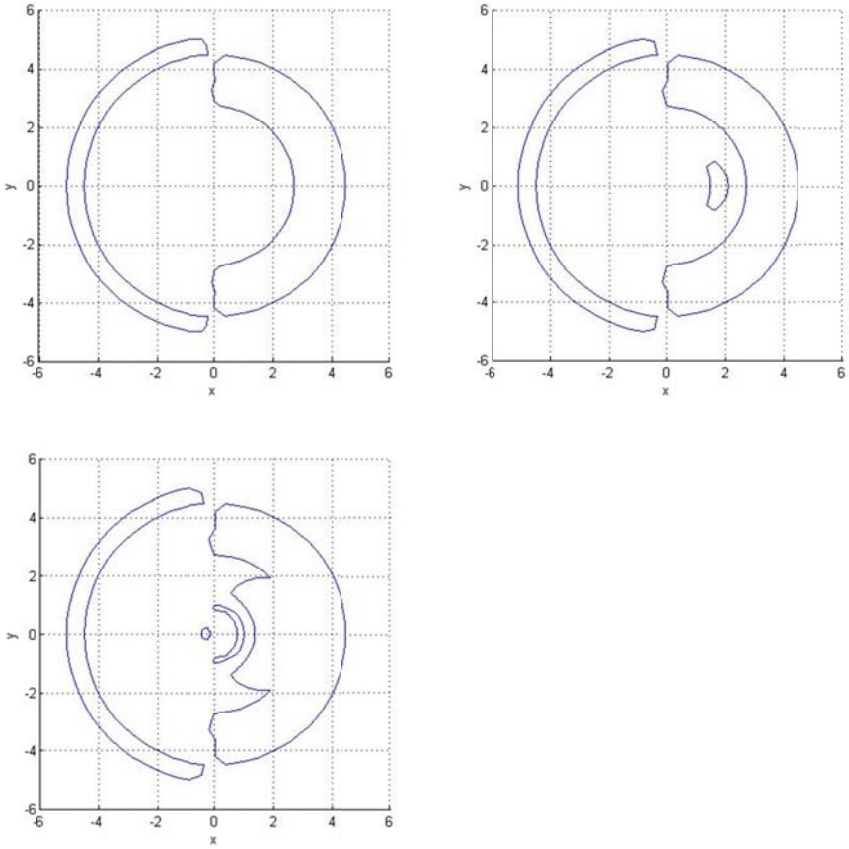

Figure 3-6 Node lines of the 1st inflow mode shape

at $\chi = 0^o, 30^o, 60^o, 90^o$ (cos part)

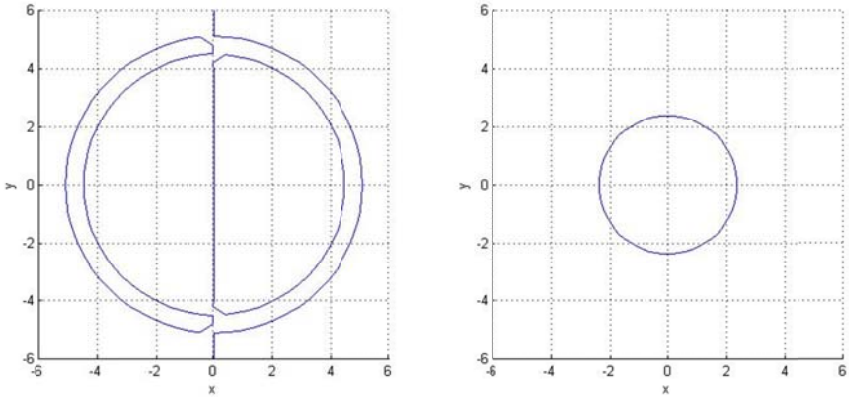

Figure 3-7 The 2nd and 3rd inflow mode shape

at $\chi = 0^o$ (cos part)

From Figure 3-5 to Figure 3-9, we can clearly see that the mode shapes are a complete set of functions on the rotor disk and in the plane of the rotor. In contrast, the He model of [13] gives only inflow on the rotor disk and thus is only a complete set of functions on that space. This further implies that the Peters-He dynamic wake model cannot be used to describe the inflow outside the disk, since no components of mode shapes off the disk. For the Hsieh/Duffy model, the modes can be used as a set of basis functions to describe the inflow space outside the rotor disk.

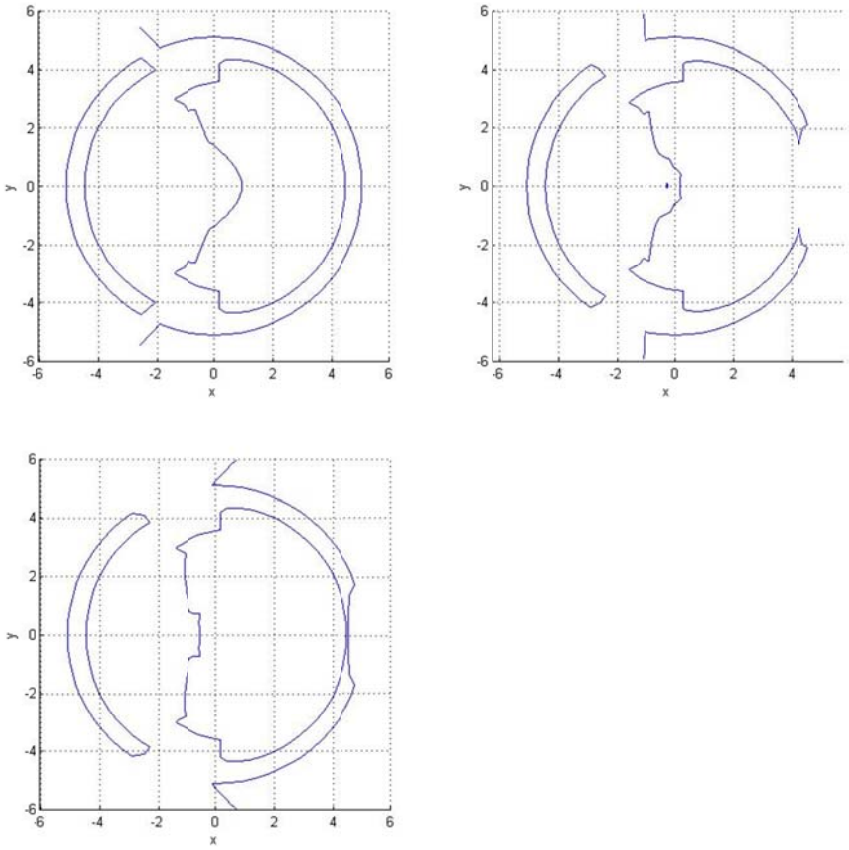

Figure 3-8 The 2nd and 3rd coupled inflow mode shape

at $\chi = 30^o, 60^o, 90^o$ (cos part)

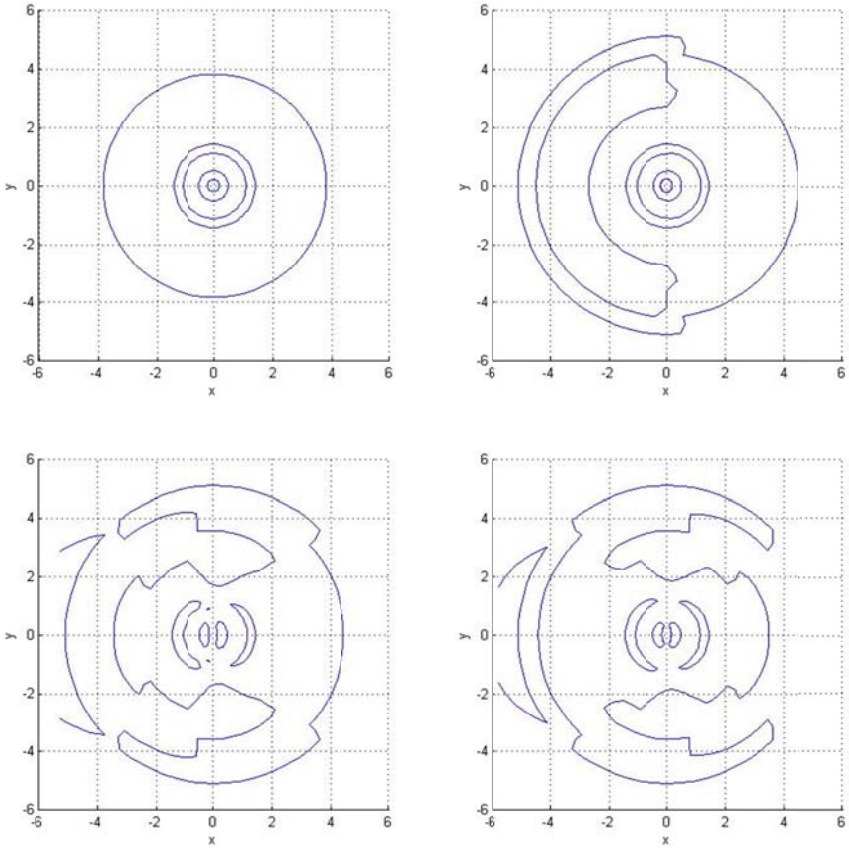

Figure 3-9 Node lines of the 50th inflow mode shape

at $\chi = 0^o, 30^o, 60^o, 90^o$ (cos part)

For the sine modes, we still follow the procedure for cosine part. Compared with the cosine modes, we can obtain the induced flow mode shapes from the sine equations of motion.

$$\vec{v} = \sum_{m=0}^{\infty} \sum_{n=m}^{\infty} \left[\bar{\phi}_{ns}^{m} \bar{P}_n^m \bar{Q}_n^m \sin\left(m\bar{\psi}\right) \right] \tag{3.10}$$

Figure 3-10 to Figure 3-12 show the plots of 1st, 20th, 40th mode respectively at typical skew angles for sine harmonics. Through the node line of the contour, we can see the characteristic of each inflow velocity mode and how they affect each other.

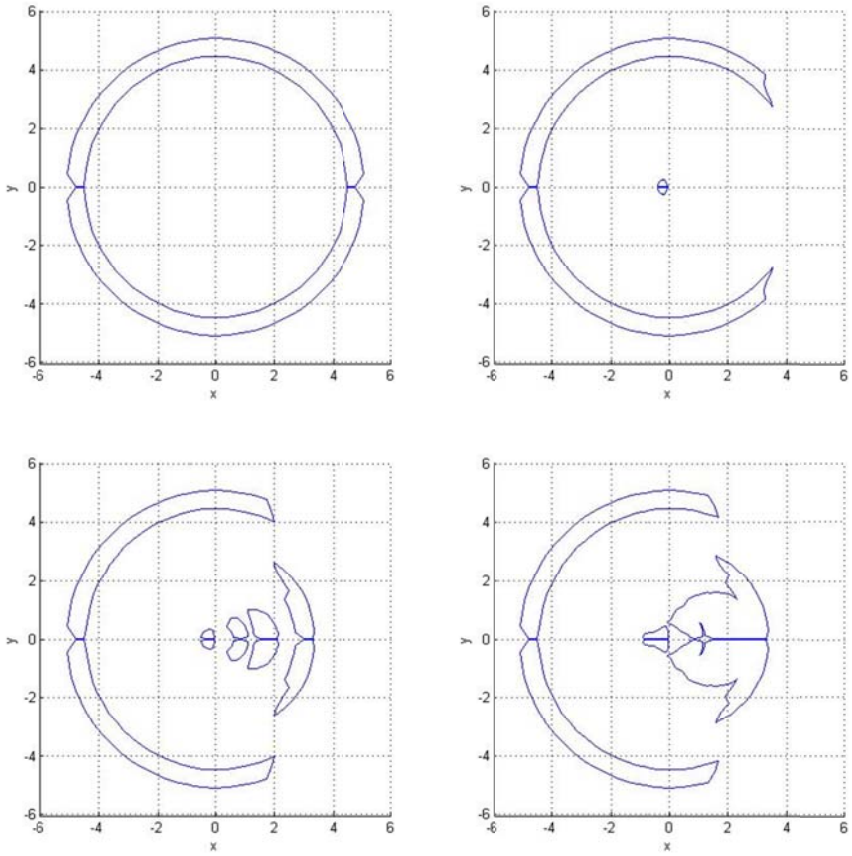

Figure 3-10 Node lines of the 1st inflow mode shape at $\chi = 0^o, 30^o, 60^o, 90^o$ (sin part)

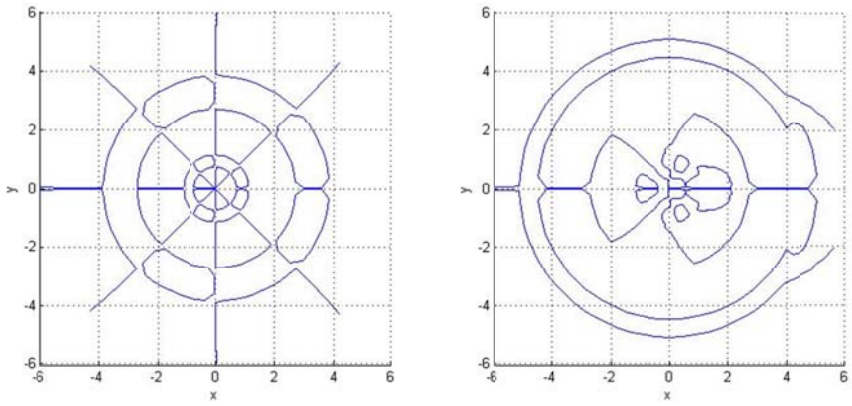

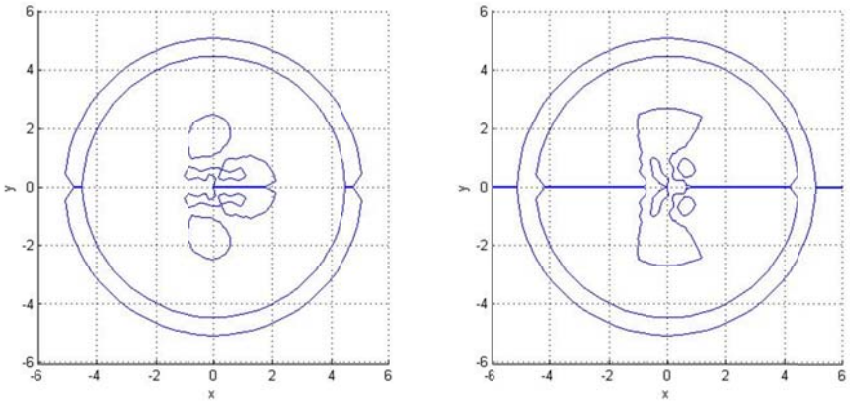

Figure 3-11 Node lines of the 20th inflow mode shape at $\chi = 0^o, 30^o, 60^o, 90^o$ (sin part)

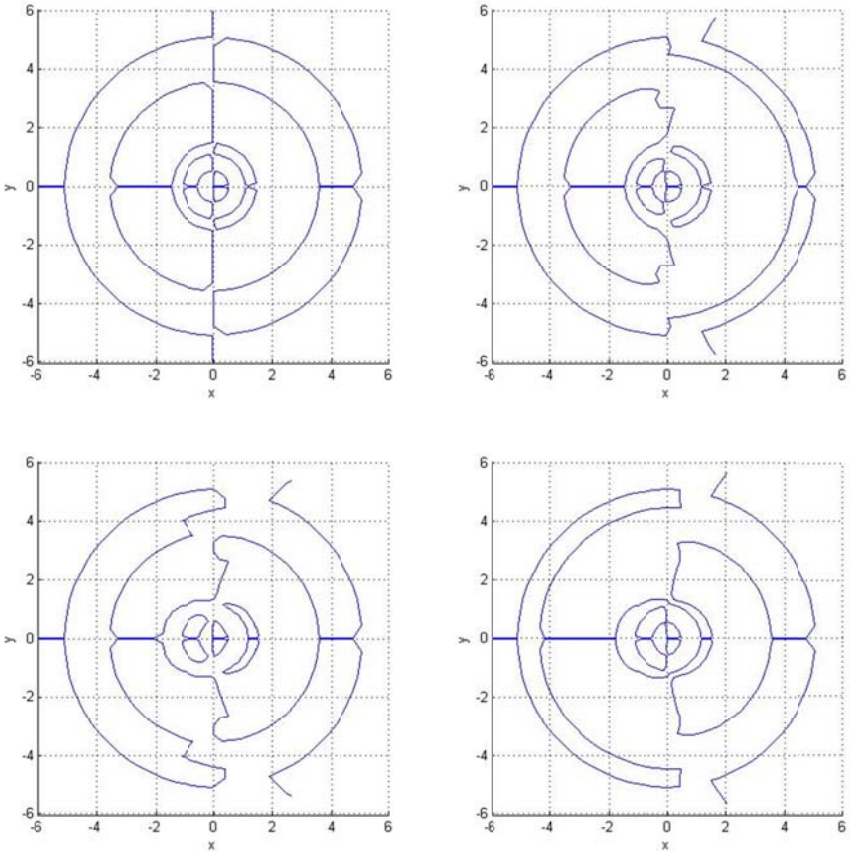

Figure 3-12 Node lines of the 40th inflow mode shape at $\chi = 0^o, 30^o, 60^o, 90^o$ (sin part)

The time responses for both Hsieh/Duffy model and He model are shown in Figure 3-13 compared with exact response at $x = 0.5, y = 0, z = 0$ with 8 harmonics. We can figure out that both models work well for step responses. But Hsieh/Duffy model is much better, since it converges much quicker than He model, as the eigenvalues for Hsieh/Duffy model are much smaller than those in He model. However, the Hsieh/Duffy model exacts this added accuracy at the cost of twice as many states and with a system that is not as well-conditioned as the He model.

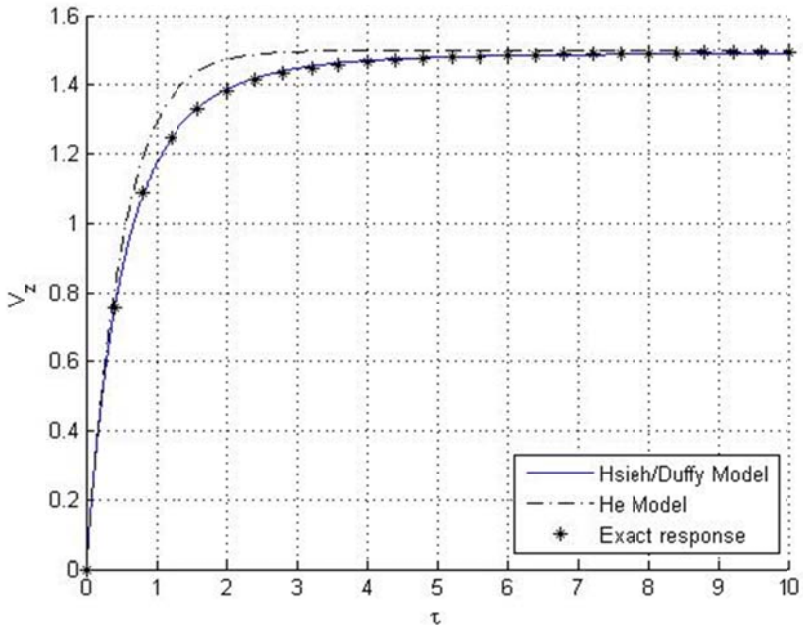

Figure 3-13 Step responses with different models
for τ_1^0 (8 harmonics at $x = 0.5, y = 0, z = 0$)

Chapter 4 Inflow Below the Disk

4.1 Exact Solution for Frequency Responses

The linearized potential flow equations can be written in nondimensional form as:

$$\frac{\partial \vec{v}}{\partial \tau} + \frac{\partial \vec{v}}{\partial \xi} = -\vec{\nabla} P \tag{4.1}$$

where equation (4.1) is the momentum equation, $\vec{v}$ is the local induced velocity vector, τ is nondimensional reduced time, ξ is the stream-wise direction (positive downstream), and P is the pressure field. It is assumed that the velocities are expressed as the gradient of a potential function, thus ensuring continuity. The derivation here is to show that, if one knows the velocity field in the upper hemisphere $\xi < 0$ (i.e., by the method of the previous section) then one can find the velocity in the lower hemisphere, $\xi > 0$. We begin with a derivation for the case of frequency response, and then Fourier Transform arguments will be used to extend the solution to the general time domain.

The solution for simple harmonic excitation is found from a complex harmonic balance applied to the momentum equation. We express the velocity as the real part of a complex quantity.

$$\vec{v}\left(x, y, z, \tau\right) = \vec{\upsilon}\left(x, y, z\right) e^{i\omega\tau} \tag{4.2}$$

where $\vec{\upsilon}\left(x, y, z\right)$ is a complex number and it is implicitly assumed that one takes only the real part of the right-hand side. Further assume that the complex pressure field P can be written as the summation of terms that includes both pressure discontinuities and mass injections:

$$P\left(x, y, z, \tau\right) = -\sum_{m=0}^{\infty} \sum_{n=m}^{\infty} \left[\tau_n^m \Phi_n^m \left(\nu, \eta, \overline{\psi}\right) \right] e^{i\omega\tau} = \overline{P} e^{i\omega\tau} \tag{4.3}$$

where Φ_n^m are a complete set of potential functions with discontinuities across the disk, and terms with $m+n$ odd represent pressure discontinues across the disk and terms with $m+n$ even represent mass sources at the disk.

To obtain a closed-form frequency response, one can expand $\vec{\upsilon}$ into real and imaginary parts.

$$\vec{\upsilon}(x,y,z) = \vec{u}(x,y,z) + i\vec{w}(x,y,z) \tag{4.4}$$

Substitution of equations (4.2) and (4.4) into equation (4.1) gives

$$i\omega\left[\vec{u}(x,y,z) + i\vec{w}(x,y,z)\right] + \left[\frac{\partial\vec{u}(x,y,z)}{\partial\xi} + i\frac{\partial\vec{w}(x,y,z)}{\partial\xi}\right] = -\vec{\nabla}\overline{P} \tag{4.5}$$

One can collect the real and imaginary parts of the equation to give expressions for the real and imaginary parts of the flow.

$$-\omega\vec{w} + \frac{\partial\vec{u}}{\partial\xi} = -\vec{\nabla}\overline{P} \tag{4.6}$$

$$\omega\vec{u} + \frac{\partial\vec{w}}{\partial\xi} = 0 \tag{4.7}$$

Solving for $\vec{u}$ from equation (4.7) and substituting it back into equation (4.6), we have

$$\frac{\partial^2\vec{w}}{\partial\xi^2} + \omega^2\vec{w} = \omega\vec{\nabla}\overline{P} \tag{4.8}$$

Similarly, solving for $\vec{w}$ from equation (4.6) and substituting it back into the derivative of equation (4.7) gives us

$$\frac{\partial^2\vec{u}}{\partial\xi^2} + \omega^2\vec{u} = -\frac{\partial}{\partial\xi}\vec{\nabla}\overline{P} \tag{4.9}$$

A Laplace transform in ξ of equations (4.9) and (4.10) yields

$$\vec{U}(s) = -\frac{s}{s^2+\omega^2}\vec{\nabla}\overline{P}(s) \tag{4.10}$$

$$\vec{W}(s) = \frac{\omega}{s^2+\omega^2}\vec{\nabla}\overline{P}(s) \tag{4.11}$$

where $\vec{W}(s)$ is the Laplace transform of $\vec{w}$, $\vec{U}(s)$ is the Laplace transform of $\vec{u}$ and $\vec{\nabla}\bar{P}(s)$ is the Laplace transform of $\vec{\nabla}\bar{P}$.

Based on the convolution inverse of a Laplace transformation, we have

$$\begin{aligned}\vec{u}(\omega, x_0, y_0, \xi_0) &= -\int_{-\infty}^{\xi_0} \cos\left[\omega(\xi_0 - \xi)\right]\vec{\nabla}\bar{P}(\xi)d\xi \\ \vec{w}(\omega, x_0, y_0, \xi_0) &= \int_{-\infty}^{\xi_0} \sin\left[\omega(\xi_0 - \xi)\right]\vec{\nabla}\bar{P}(\xi)d\xi\end{aligned} \tag{4.12}$$

Note that the only boundary condition on the flow is that the flow approach zero far upstream ($\xi = -\infty$). Thus, the lower limits are set at $-\infty$. The physical meaning of equation (4.12) is that, to obtain the exact solution, one must integrate the gradient of the pressure field along a streamline from far upstream down to the point within the flow field for which that component of velocity is desired. For the real part of the flow, the integral includes the kernel $\cos\left[\omega(\xi_0 - \xi)\right]$, and for the imaginary part it includes the kernel $\sin\left[\omega(\xi_0 - \xi)\right]$. Note that, for axial flow, $\xi = z$.

The above approach is not tractable for use in practical rotor calculations. However, it is useful to have both as a way to determine an "exact" numerical solution against which to compare finite-state solutions (and this has been done in previous work) and as the theoretical basis for an exact time-domain solution. Thus, the utility of equation (4.12) is in its usefulness in a proof of how to find the flow below the disk, as will be outlined below.

4.2 Adjoint-states

In the derivation of the next section, we first define the adjoint velocity above the rotor disk which will be used to find the velocity below the disk. Thus, in this section, we demonstrate how to find the velocity and the adjoint velocity from Morillo's modified model, Ref. [6]. The momentum equation for a skewed flow in the Morillo derived potentials is:

$$\left[M^c\right]\left\{\overset{*}{a}{}_n^m\right\} + \left[D^c\right]\left[\tilde{L}^c\right]^{-1}\left[M^c\right]\left\{a_n^m\right\} = \left[D^c\right]\left\{\tau_n^{mc}\right\} \tag{4.13}$$

Here, we only consider the case of a harmonic cosine pressure input; the sine part can be found by a similar procedure. Suppose the unknowns are expressed in complex notation as the real part of a substitute problem where the barred quantities are cosine and sine coefficients.

$$a_n^m = \left(\bar{a}_n^m + i\bar{b}_n^m\right)e^{i\omega\tau} = \bar{a}_n^m \cos(\omega\tau) - \bar{b}_n^m \sin(\omega\tau) \tag{4.14}$$

$$\tau_n^{mc} = \bar{\tau}_n^m \cos(\omega\tau) \tag{4.15}$$

For the sake of the derivation to follow, we also define tilda-quantities as the barred quantities multiplied by cosine and sine.

$$\tilde{a}_n^m = \bar{a}_n^m \cos(\omega\tau); \tilde{b}_n^m = -\bar{b}_n^m \sin(\omega\tau) \tag{4.16}$$

It follows that $a_n^m = \tilde{a}_n^m + \tilde{b}_n^m$. Substitution of equations (4.14), (4.15) and (4.16) into (4.13) yields

$$\begin{aligned} &-\omega\left[M^c\right]\left\{\bar{a}_n^m\right\}\sin(\omega\tau) - \omega\left[M^c\right]\left\{\bar{b}_n^m\right\}\cos(\omega\tau) \\ &+\left[D^c\right]\left[\tilde{L}^c\right]^{-1}\left[M^c\right]\left\{\bar{a}_n^m\right\}\cos(\omega\tau) - \left[D^c\right]\left[\tilde{L}^c\right]^{-1}\left[M^c\right]\left\{\bar{b}_n^m\right\}\sin(\omega\tau) \\ &=\left[D^c\right]\left\{\bar{\tau}_n^m\right\}\cos(\omega\tau) \end{aligned} \tag{4.17}$$

As equation (4.17) should be satisfied at any time, so the coefficients for cosine and sin terms at both size of the equation should be equal. Collecting the coefficients for cosine and sin terms, we have

$$\begin{aligned} &\cos: -\omega\left[M^c\right]\left\{\bar{b}_n^m\right\} + \left[D^c\right]\left[\tilde{L}^c\right]^{-1}\left[M\right]\left\{\bar{a}_n^m\right\} = \left[D^c\right]\left\{\bar{\tau}_n^{mc}\right\} \\ &\sin: -\omega\left[M^c\right]\left\{\bar{a}_n^m\right\} - \left[D^c\right]\left[\tilde{L}^c\right]^{-1}\left[M^c\right]\left\{\bar{b}_n^m\right\} = \{0\} \end{aligned} \tag{4.18}$$

which are equivalent to

$$\left[M^c\right]\left\{\overset{*}{\tilde{b}}_n^m\right\} + \left[D^c\right]\left[\tilde{L}^c\right]^{-1}\left[M^c\right]\left\{\tilde{a}_n^m\right\} = \left[D^c\right]\left\{\tau_n^{mc}\right\} \tag{4.19}$$

$$\left[M^c\right]\left\{\overset{*}{\tilde{a}}_n^m\right\} + \left[D^c\right]\left[\tilde{L}^c\right]^{-1}\left[M^c\right]\left\{\tilde{b}_n^m\right\} = \{0\} \tag{4.20}$$

We substitute (4.20) into the following adjoint equation

$$
\begin{aligned}
&-\left[M^c\right]\left\{\overset{*}{\tilde{a}}_n^{mc}\right\}+\left[D^c\right]\left[\tilde{L}^c\right]^{-1}\left[M^c\right]\left\{\tilde{a}_n^{mc}\right\}\\
&=-\left[D^c\right]\left[\tilde{L}^c\right]^{-1}\left[M^c\right]\left\{\bar{b}_n^m\right\}\sin(\omega\tau)+\left[D^c\right]\left[\tilde{L}^c\right]^{-1}\left[M^c\right]\left\{\bar{a}_n^m\right\}\cos(\omega\tau)\\
&=\left[D^c\right]\left[\tilde{L}^c\right]^{-1}\left[M^c\right]\left\{a_n^m\right\}
\end{aligned}
\tag{4.21}
$$

And substituting (4.19) into the same adjoint equation

$$
\begin{aligned}
&-\left[M^c\right]\left\{\overset{*}{\tilde{b}}_n^m\right\}+\left[D^c\right]\left[\tilde{L}^c\right]^{-1}\left[M^c\right]\left\{\tilde{b}_n^m\right\}\\
&=\omega\left[M^c\right]\left\{\bar{b}_n^m\right\}\cos(\omega\tau)-\left[D^c\right]\left[\tilde{L}^c\right]^{-1}\left[M^c\right]\left\{b_n^m\right\}\sin(\omega\tau)\\
&=\left[D^c\right]\left[\tilde{L}^c\right]^{-1}\left[M^c\right]\left\{\bar{a}_n^m\right\}\cos(\omega\tau)-\left[D^c\right]\left\{\bar{\tau}_n^m\right\}\cos(\omega\tau)\\
&\qquad\qquad-\left[D^c\right]\left[\tilde{L}^c\right]^{-1}\left[M^c\right]\left\{b_n^m\right\}\sin(\omega\tau)\\
&=\left(\left[D^c\right]\left[\tilde{L}^c\right]^{-1}\left[M^c\right]\left\{\bar{a}_n^m\right\}-\left[D^c\right]\left\{\bar{\tau}_n^m\right\}\right)\cos(\omega\tau)\\
&\qquad\qquad-\left[D^c\right]\left[\tilde{L}^c\right]^{-1}\left[M^c\right]\left\{\bar{b}_n^m\right\}\sin(\omega\tau)\\
&=\left[D^c\right]\left[\tilde{L}^c\right]^{-1}\left[M^c\right]\left\{a_n^m\right\}-\left[D^c\right]\left\{\tau_n^{mc}\right\}
\end{aligned}
\tag{4.22}
$$

We then construct the adjoint to the momentum equation by subtracting equation (4.22) from (4.21), we have

$$
-\left[M^c\right]\left\{\overset{*}{\Delta}_n^m\right\}+\left[D^c\right]\left[\tilde{L}^c\right]^{-1}\left[M^c\right]\left\{\Delta_n^m\right\}=\left[D^c\right]\left\{\tau_n^{mc}\right\} \tag{4.23}
$$

where $\Delta_n^m=\left\{\tilde{a}_n^m\right\}-\left\{\tilde{b}_n^m\right\}=\left\{\bar{a}_n^m\right\}\cos(\omega\tau)+\left\{\bar{b}_n^m\right\}\sin(\omega\tau)$.

We can then define the tilda quantities in terms of regular and adjoint variables.

$$
\begin{aligned}
\left\{\tilde{a}_n^m\right\}&=\frac{1}{2}\left(\left\{a_n^m\right\}+\left\{\Delta_n^m\right\}\right)\\
\left\{\tilde{b}_n^m\right\}&=\frac{1}{2}\left(\left\{a_n^m\right\}-\left\{\Delta_n^m\right\}\right)
\end{aligned}
\tag{4.24}
$$

As we already know that

$$
\begin{aligned}
\vec{v}(r,\bar{\psi},\xi,\tau)&=\left(\sum_{m=0}^{\infty}\sum_{n=m}^{\infty}\bar{a}_n^m\vec{\nabla}\hat{\Psi}_n^m(\nu,\eta,\bar{\psi})+i\sum_{m=0}^{\infty}\sum_{n=m}^{\infty}\bar{b}_n^m\vec{\nabla}\hat{\Psi}_n^m(\nu,\eta,\bar{\psi})\right)e^{i\omega\tau}\\
&=\sum_{m=0}^{\infty}\sum_{n=m}^{\infty}a_n^m\vec{\nabla}\hat{\Psi}_n^{mc}(\nu,\eta,\bar{\psi})
\end{aligned}
\tag{4.25}
$$

Then we can define the adjoint (or conjugate) velocity as

$$\begin{aligned}\vec{\bar{v}}\left(r,\bar{\psi},\xi,\tau\right) &= \left(\sum_{m=0}^{\infty}\sum_{n=m}^{\infty}\bar{a}_n^m\vec{\nabla}\hat{\Psi}_n^m\left(\nu,\eta,\bar{\psi}\right) - i\sum_{m=0}^{\infty}\sum_{n=m}^{\infty}\bar{b}_n^m\vec{\nabla}\hat{\Psi}_n^m\left(\nu,\eta,\bar{\psi}\right)\right)e^{i\omega\tau} \\ &= \sum_{m=0}^{\infty}\sum_{n=m}^{\infty}\Delta_n^m\vec{\nabla}\hat{\Psi}_n^{mc}\left(\nu,\eta,\bar{\psi}\right)\end{aligned} \tag{4.26}$$

4.3 Velocity below Disk

Assume that one knows the solution of the frequency response outlined above by some method (such as the finite-state method) but in the upper hemisphere only. We now wish to show how that solution can be used to find the solution for the complex velocity in the lower hemisphere. In order to simplify the derivation to follow, we define the following quantities for $-\infty < \xi_0 < 0$. (Thus, they are defined only above the disk.)

$$\begin{aligned}\vec{C}\left(\omega,x_0,y_0,\xi_0\right) &\equiv -\int_{-\infty}^{\xi_0}\cos\left(\omega\xi\right)\vec{\nabla}\bar{P}\left(\xi\right)d\xi \\ \vec{S}\left(\omega,x_0,y_0,\xi_0\right) &\equiv -\int_{-\infty}^{\xi_0}\sin\left(\omega\xi\right)\vec{\nabla}\bar{P}\left(\xi\right)d\xi\end{aligned} \tag{4.27}$$

Not that, for the special case $\tau_j^r = 1$, and all other $m \neq r, n \neq j$, $\tau_n^m = 0$, we can write from equation (4.27) with no loss of generality.

$$\begin{aligned}\vec{C}\left(\omega,r_0,\bar{\psi}_0,\xi_0\right) &= \vec{C}\left(\omega,x_0,y_0,\xi_0\right) \equiv -\int_{-\infty}^{\xi_0}\cos\left(\omega\xi\right)\vec{\nabla}\Phi_j^r\left(\xi\right)d\xi \\ \vec{S}\left(\omega,r_0,\bar{\psi}_0,\xi_0\right) &= \vec{S}\left(\omega,x_0,y_0,\xi_0\right) \equiv -\int_{-\infty}^{\xi_0}\sin\left(\omega\xi\right)\vec{\nabla}\Phi_j^r\left(\xi\right)d\xi\end{aligned} \tag{4.28}$$

where $x_0 = -r_0\cos\bar{\psi}_0$ and $y_0 = r_0\sin\bar{\psi}_0$. We rewrite $\vec{u}\left(\omega,x_0,y_0,\xi_0\right)$ and $\vec{w}\left(\omega,x_0,y_0,\xi_0\right)$ as

$$\begin{aligned}\vec{u}\left(\omega,r_0,\bar{\psi}_0,\xi_0\right) &= -\cos\left(\omega\xi_0\right)\int_{-\infty}^{\xi_0}\cos\left(\omega\xi\right)\vec{\nabla}P\left(\xi\right)d\xi - \sin\left(\omega\xi_0\right)\int_{-\infty}^{\xi_0}\sin\left(\omega\xi\right)\vec{\nabla}\bar{P}\left(\xi\right)d\xi \\ &= \cos\left(\omega\xi_0\right)\vec{C}\left(\omega,x_0,y_0,\xi_0\right) + \sin\left(\omega\xi_0\right)\vec{S}\left(\omega,x_0,y_0,\xi_0\right) \\ \vec{w}\left(\omega,r_0,\bar{\psi}_0,\xi_0\right) &= \sin\left(\omega\xi_0\right)\int_{-\infty}^{\xi_0}\cos\left(\omega\xi\right)\vec{\nabla}P\left(\xi\right)d\xi - \cos\left(\omega\xi_0\right)\int_{-\infty}^{\xi_0}\sin\left(\omega\xi\right)\vec{\nabla}\bar{P}\left(\xi\right)d\xi \\ &= -\sin\left(\omega\xi_0\right)C\left(\omega,x_0,y_0,\xi_0\right) + \cos\left(\omega\xi_0\right)S\left(\omega,x_0,y_0,\xi_0\right)\end{aligned} \tag{4.29}$$

The induced velocity above the disk is then

$$\begin{aligned}\vec{v}\left(r_0,\bar{\psi}_0,\xi_0,\tau\right) &= \vec{u}\left(\omega,r_0,\bar{\psi}_0,\xi_0\right)\cos\left(\omega\tau\right)-\vec{w}\left(\omega,r_0,\bar{\psi}_0,\xi_0\right)\sin\left(\omega\tau\right)\\ &= \cos\left(\omega\xi_0\right)\vec{C}\left(\omega,r_0,\bar{\psi}_0,\xi_0\right)\cos\left(\omega\tau\right)+\sin\left(\omega\xi_0\right)\vec{S}\left(\omega,r_0,\bar{\psi}_0,\xi_0\right)\cos\left(\omega\tau\right)\\ &\quad+\sin\left(\omega\xi_0\right)\vec{C}\left(\omega,r_0,\bar{\psi}_0,\xi_0\right)\sin\left(\omega\tau\right)\\ &\quad-\cos\left(\omega\xi_0\right)\vec{S}\left(\omega,r_0,\bar{\psi}_0,\xi_0\right)\sin\left(\omega\tau\right)\end{aligned} \tag{4.30}$$

which is equivalent to

$$\vec{v}\left(r_0,\bar{\psi}_0,\xi_0,\tau\right)=\cos\left[\omega\left(\tau-\xi_0\right)\right]\vec{C}\left(\omega,r_0,\bar{\psi}_0,\xi_0\right)-\sin\left[\omega\left(\tau-\xi_0\right)\right]\vec{S}\left(\omega,r_0,\bar{\psi}_0,\xi_0\right) \tag{4.31}$$

In preparation for the solution of the flow below the disk, we now need to compute $\vec{C}$ and $\vec{S}$ from the finite-state solution above the disk. Since the Morillo states are complex for a frequency response, they are broken into real and imaginary parts $\bar{a}_n^m$ and $\bar{b}_n^m$. This gives:

$$\begin{aligned}\vec{u}\left(\omega,r_0,\bar{\psi}_0,\xi_0\right) &= \sum_{m=0}^{\infty}\sum_{n=m}^{\infty}\bar{a}_n^m\vec{\nabla}\hat{\Psi}_n^m\left(\nu,\eta,\bar{\psi}\right)\\ &= \cos\left(\omega\xi_0\right)\vec{C}\left(\omega,r_0,\bar{\psi}_0,\xi_0\right)+\sin\left(\omega\xi_0\right)\vec{S}\left(\omega,r_0,\bar{\psi}_0,\xi_0\right)\\ \vec{w}\left(\omega,r_0,\bar{\psi}_0,\xi_0\right) &= \sum_{m=0}^{\infty}\sum_{n=m}^{\infty}\bar{b}_n^m\vec{\nabla}\hat{\Psi}_n^m\left(\nu,\eta,\bar{\psi}\right)\\ &= -\sin\left(\omega\xi_0\right)\vec{C}\left(\omega,r_0,\bar{\psi}_0,\xi_0\right)+\cos\left(\omega\xi_0\right)\vec{S}\left(\omega,r_0,\bar{\psi}_0,\xi_0\right)\end{aligned} \tag{4.32}$$

where $\nu,\eta,\bar{\psi}$ is the ellipsoidal coordinate location of $r_0,\bar{\psi}_0,\xi_0$; and $\hat{\Psi}_n^m$ is the derived Morillo velocity potential.

Therefore, Equation (4.32) allows us to express the $\vec{C}$ and $\vec{S}$ integrals in terms of the known finite-state result.

$$\begin{aligned}\vec{C}\left(\omega,r_0,\bar{\psi}_0,\xi_0\right) &= \sum_{m=0}^{\infty}\sum_{n=m}^{\infty}\bar{a}_n^m\cos\left(\omega\xi_0\right)\vec{\nabla}\hat{\Psi}_n^m\left(\nu,\eta,\bar{\psi}\right)-\sum_{m=0}^{\infty}\sum_{n=m}^{\infty}\bar{b}_n^m\sin\left(\omega\xi_0\right)\vec{\nabla}\hat{\Psi}_n^m\left(\nu,\eta,\bar{\psi}\right)\\ \vec{S}\left(\omega,r_0,\bar{\psi}_0,\xi_0\right) &= \sum_{m=0}^{\infty}\sum_{n=m}^{\infty}\bar{a}_n^m\sin\left(\omega\xi_0\right)\vec{\nabla}\hat{\Psi}_n^m\left(\nu,\eta,\bar{\psi}\right)+\sum_{m=0}^{\infty}\sum_{n=m}^{\infty}\bar{b}_n^m\cos\left(\omega\xi_0\right)\vec{\nabla}\hat{\Psi}_n^m\left(\nu,\eta,\bar{\psi}\right)\end{aligned} \tag{4.33}$$

The above are valid above the disk plane which is for $-\infty<\xi_0<0$. However, below the disk, where $\xi_0>0$, we must integrate equation (4.28) from upstream down

to the disk of the rotor plane and then below the plane. For simplicity, we will assume the single term $P = -\Phi_j^r$, where $\Phi_j^r = \bar{P}_j^r(\nu)\bar{Q}_j^r(i\eta)\cos(r\bar{\psi})$. Since any pressure can be represented as a sum of these, as in equation (4.3), this assumption poses no restriction on generality. The below-plane result is:

$$
\begin{aligned}
&\vec{u}(\omega, r_0, \bar{\psi}_0, \xi_0) \\
&\quad = \int_{-\infty}^{\xi_0} \cos\left[\omega(\xi_0 - \xi)\right] \vec{\nabla}\Phi_j^r(\xi)\, d\xi \\
&\quad = \cos(\omega\xi_0) \int_{-\infty}^{0} \cos(\omega\xi) \vec{\nabla}\Phi_j^r(\xi)\, d\xi + \sin\left(\omega\tilde{\xi}_0\right) \int_{-\infty}^{0} \sin(\omega\xi) \vec{\nabla}\Phi_j^r(\xi)\, d\xi \\
&\qquad + \cos(\omega\xi_0) \int_{0}^{\xi_0} \cos(\omega\xi) \vec{\nabla}\Phi_j^r(\xi)\, d\xi + \sin\left(\omega\tilde{\xi}_0\right) \int_{0}^{\xi_0} \sin(\omega\xi) \vec{\nabla}\Phi_j^r(\xi)\, d\xi \\
&\quad = \cos(\omega\xi_0) \vec{C}(\omega, r_0, \bar{\psi}_0, 0) + \sin(\omega\xi_0) \vec{S}(\omega, r_0, \bar{\psi}_0, 0) \\
&\qquad + \cos(\omega\xi_0) \int_{0}^{\xi_0} \cos(\omega\xi) \vec{\nabla}\Phi_j^r(\xi)\, d\xi + \sin(\omega\xi_0) \int_{0}^{\xi_0} \sin(\omega\xi) \vec{\nabla}\Phi_j^r(\xi)\, d\xi \\
&\vec{w}(\omega, r_0, \bar{\psi}_0, \xi_0) \\
&\quad = -\int_{-\infty}^{\xi_0} \sin\left[\omega(\xi_0 - \xi)\right] \vec{\nabla}\Phi_j^r(\xi)\, d\xi \\
&\quad = -\sin(\omega\xi_0) \int_{-\infty}^{0} \cos(\omega\xi) \vec{\nabla}\Phi_j^r(\xi)\, d\xi + \cos(\omega\xi_0) \int_{-\infty}^{0} \sin(\omega\xi) \vec{\nabla}\Phi_j^r(\xi)\, d\xi \\
&\qquad - \sin(\omega\xi_0) \int_{0}^{\xi_0} \cos(\omega\xi) \vec{\nabla}\Phi_j^r(\xi)\, d\xi + \cos(\omega\xi_0) \int_{0}^{\xi_0} \sin(\omega\xi) \vec{\nabla}\Phi_j^r(\xi)\, d\xi \\
&\quad = -\sin(\omega\xi_0) \vec{C}(\omega, r_0, \bar{\psi}_0, 0) + \cos(\omega\xi_0) \vec{S}(\omega, r_0, \bar{\psi}_0, 0) \\
&\qquad - \sin(\omega\xi_0) \int_{0}^{\xi_0} \cos(\omega\xi) \vec{\nabla}\Phi_j^r(\xi)\, d\xi + \cos(\omega\xi_0) \int_{0}^{\xi_0} \sin(\omega\xi) \vec{\nabla}\Phi_j^r(\xi)\, d\xi
\end{aligned}
\tag{4.34}
$$

where the integrals are broken into two parts: one from downstream infinity to the disk, and one from the disk to the desired point below the disk. However, due to the symmetries in the system, we can write the integral segments below the disk in terms of integral segments above the disk. Thus, for $\xi_0 > 0$:

$$
\begin{aligned}
\int_{0}^{\xi_0} \cos(\omega\xi) \vec{\nabla}\Phi_j^r(\xi)\, d\xi &= (-1)^{j+1} \int_{-\xi_0}^{0} \cos(\omega\xi) \vec{\nabla}\Phi_j^r(\xi)\, d\xi \\
&= (-1)^{j+1} \left[\vec{C}(\omega, r_0, \tilde{\psi}_0, 0) - \vec{C}(\omega, r_0, \tilde{\psi}_0, -\xi_0)\right] \\
\int_{0}^{\xi_0} \sin(\omega\xi) \vec{\nabla}\Phi_j^r(\xi)\, d\xi &= (-1)^{j} \int_{-\xi_0}^{0} \sin(\omega\xi) \vec{\nabla}\Phi_j^r(\xi)\, d\xi \\
&= (-1)^{j} \left[\vec{S}(\omega, r_0, \tilde{\psi}_0, 0) - \vec{S}(\omega, r_0, \tilde{\psi}_0, -\xi_0)\right]
\end{aligned}
\tag{4.35}
$$

The reasons for the form of equation (4.35) are as follows. First, with the exception of sign, the downstream streamline emanating from $r_0, \bar{\psi}_0$ is identical in functionality to the upstream streamline emanating from $r_0, \tilde{\psi}_0$ (where $\tilde{\psi}_0 = \bar{\psi}_0 + \pi$). The differences in sign are due to the following

a) For $r + j$ odd, the pressure potential is of opposite sign above and below the disk, whereas the gradient of pressure is the same sign above and below the disk. For $r + j$ even, the opposite is true. Since the integrals involve gradient of pressure, there is a factor of $(-1)^{r+j+1}$

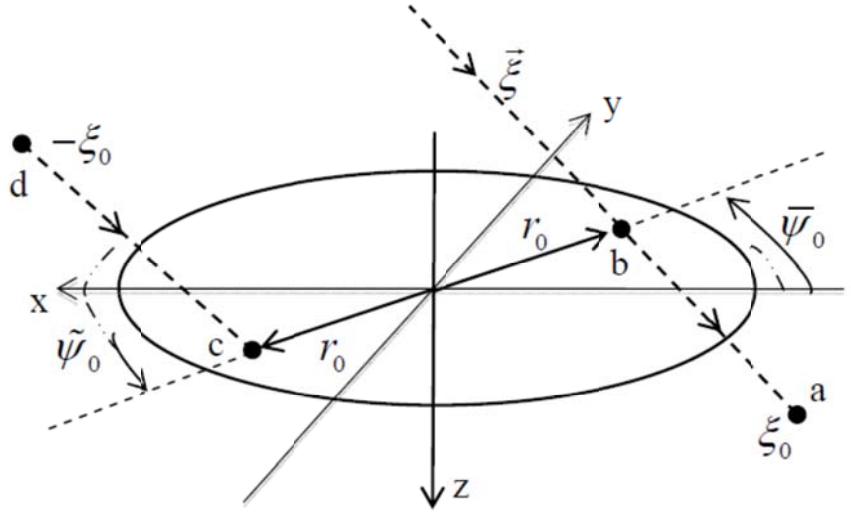

Figure 4-1 3-D Perspective of Co-states

b) The fact that $\tilde{\psi}_0$ is on the opposite side of disk as $\bar{\psi}_0$ implies that every $\bar{\psi}$ along the upstream streamline will differ by π from $\bar{\psi}$ along the downstream streamline. Therefore, the $\sin(r\bar{\psi})$ and $\cos(r\bar{\psi})$ terms in Φ_j^r will yield a factor of $(-1)^r$.

Consequently, we have a total sign change for the cosine integral of:

$$\text{sign} = (-1)^{r+j+1}(-1)^r = (-1)^{2r+j+1} = (-1)^{j+1} \qquad (4.36)$$

An extra (-1) appears in the sine integral because $\sin(\omega\xi) = -\sin(-\omega\xi)$. Thus, the terms $(-1)^{j+1}$ and $(-1)^{j}$ appear in the last lines of equation (4.35). We then have from equations (4.34) and (4.35) that the $\vec{u}$ and $\vec{w}$ for $\xi_0 > 0$ are:

$$\begin{aligned}
&\vec{u}(\omega, r_0, \bar{\psi}_0, \xi_0) \\
&\quad = \cos(\omega\xi_0)\left\{\vec{C}(\omega, r_0, \bar{\psi}_0, 0) + (-1)^{j+1}\left[\vec{C}(\omega, r_0, \tilde{\psi}_0, 0) - \vec{C}(\omega, r_0, \tilde{\psi}_0, -\xi_0)\right]\right\} \\
&\quad + \sin(\omega\xi_0)\left\{\vec{S}(\omega, r_0, \bar{\psi}_0, 0) + (-1)^{j}\left[\vec{S}(\omega, r_0, \tilde{\psi}_0, 0) - \vec{S}(\omega, r_0, \tilde{\psi}_0, -\xi_0)\right]\right\} \\
&\vec{w}(\omega, r_0, \bar{\psi}_0, \xi_0) \\
&\quad = -\sin(\omega\xi_0)\left\{\vec{C}(\omega, r_0, \bar{\psi}_0, 0) + (-1)^{j+1}\left[\vec{C}(\omega, r_0, \tilde{\psi}_0, 0) - \vec{C}(\omega, r_0, \tilde{\psi}_0, -\xi_0)\right]\right\} \\
&\quad + \cos(\omega\xi_0)\left\{\vec{S}(\omega, r_0, \bar{\psi}_0, 0) + (-1)^{j}\left[\vec{S}(\omega, r_0, \tilde{\psi}_0, 0) - \vec{S}(\omega, r_0, \tilde{\psi}_0, -\xi_0)\right]\right\}
\end{aligned} \tag{4.37}$$

Note that the above terms from the integrals below the disk are rewritten in terms of integrals above the disk (i.e., the terms with $(-1)^{j}$ or $(-1)^{j+1}$ which are functions of $\tilde{\psi}_0$ rather than of $\bar{\psi}_0$). These mirror the $\bar{\psi}_0$ terms with the exception that the $\vec{C}$ terms are multiplied by $(-1)^{j+1}$ while the $\vec{S}$ terms are multiplied by $(-1)^{j}$. As a result of these sign differences, when we put the complex below-disk velocity from equation (4.37) back into the time domain—as was done for the above-disk velocity in equation (4.30)—the terms involving $\sin\left[\omega(\tau - \xi_0)\right]$ are of the opposite sign from those in equation (4.31).

$$\begin{aligned}
&\vec{v}(r_0, \bar{\psi}_0, \xi_0, \tau) \\
&\quad = \cos\left[\omega(\tau - \xi_0)\right]\vec{C}(\omega, r_0, \bar{\psi}_0, \xi_0) - \sin\left[\omega(\tau - \xi_0)\right]\vec{S}(\omega, r_0, \bar{\psi}_0, \xi_0) \\
&\quad + (-1)^{j+1}\left\{\cos\left[\omega(\tau - \xi_0)\right]\vec{C}(\omega, r_0, \tilde{\psi}_0, 0) + \sin\left[\omega(\tau - \xi_0)\right]\vec{S}(\omega, r_0, \tilde{\psi}_0, 0)\right\} \\
&\quad - (-1)^{j+1}\left\{\cos\left[\omega(\tau - \xi_0)\right]\vec{C}(\omega, r_0, \tilde{\psi}_0, -\xi_0) + \sin\left[\omega(\tau - \xi_0)\right]\vec{S}(\omega, r_0, \tilde{\psi}_0, -\xi_0)\right\}
\end{aligned} \tag{4.38}$$

From equation (4.38), one can write the general, time-domain version of the induced flow below the rotor disk.

$$\vec{v}\left(r_0,\bar{\psi}_0,\xi_0,\tau\right)=\vec{v}\left(r_0,\bar{\psi}_0,0,\tau-\xi_0\right)+\vec{v}^{*}\left(r_0,\tilde{\psi}_0,0,\tau-\xi_0\right)-\vec{v}^{*}\left(r_0,\tilde{\psi}_0,-\xi_0,\tau\right) \quad (4.39)$$

where $\vec{v}^{*}$ is $(-1)^{j+1}$ times the velocity that would be obtained from the adjoint equations (i.e., the equations with a negative sign on the time derivatives). This equation (4.39) is the fundamental result of this derivation and represents the general form of the velocity below the disk in the time domain and/or frequency domain. As shown in Figure 4-1, $\vec{v}\left(r_0,\bar{\psi}_0,\xi_0,\tau\right)$ is the velocity below the rotor disk at point a along the streamline; $\vec{v}\left(r_0,\bar{\psi}_0,0,\tau-\xi_0\right)$ is the velocity at point b where the free streamline intersect the rotor plane; $\vec{v}^{*}\left(r_0,\tilde{\psi}_0,0,\tau-\xi_0\right)$ is the adjoint velocity at point c which is centro-symmetric to point b; $\vec{v}^{*}\left(r_0,\tilde{\psi}_0,-\xi_0,\tau\right)$ is the adjoint velocity at point d which is centro-symmetric to point a. In other words, it is:

$$\begin{aligned}\vec{v}^{*}\left(r,\bar{\psi},\xi,\tau\right)&=(-1)^{j+1}\left[\vec{u}\cos\left(\omega\tau\right)+\vec{w}\sin\left(\omega\tau\right)\right]\\&=(-1)^{j+1}\vec{\bar{v}}\left(r,\bar{\psi},\xi,\tau\right)\end{aligned} \quad (4.40)$$

where $\vec{\bar{v}}$ is defined in (4.26) as conjugate velocity.

The reason that equation (4.38) can be generalized to equation (4.39) is that any general time-domain solution can be expressed as a Fourier Transform in terms of frequency components. Since equation (4.38) is true for any frequency in the transform, then it is true in general for the inverse transform when written in terms of $\vec{v}^{*}$ as in equation (4.39). In the general time-domain solution, $\vec{v}^{*}$ is defined as the solution to the adjoint equations—i.e., the solution of the differential equations in which the time derivative terms are multiplied by (-1). In addition, this adjoint velocity is defined for the condition in which each forcing function in those time-domain equations—i.e., each $\tau_n^m(\tau)$ in equation (4.3)—is multiplied by $(-1)^{n+1}$ in the forcing functions of the adjoint equations, which is exactly as the following equation:

$$-\left[M^c\right]\left\{\bar{\Delta}_n^{*m}\right\}+\left[D^c\right]\left[\tilde{L}^c\right]^{-1}\left[M^c\right]\left\{\bar{\Delta}_n^m\right\}=\left[D^c\right]\begin{bmatrix}\ddots & & \\ & (-1)^{n+1} & \\ & & \ddots\end{bmatrix}\left\{\tau_n^{mc}\right\} \quad (4.41)$$

Then the conjugate velocity could be expressed as

$$\vec{v}^{*}\left(r,\bar{\psi},\xi,\tau\right)=\sum_{m=0}^{\infty}\sum_{n=m}^{\infty}\bar{\Delta}_{n}^{m}\vec{\nabla}\hat{\Psi}_{n}^{mc}\left(v,\eta,\bar{\psi}\right) \tag{4.42}$$

It should be noted that the solution in equation (4.39) does not include the jump in velocity across the actuator disk due to the mass sources. The purpose of this dissertation is strictly to present the potential flow solution.

4.4 Results for Axial Flow

Axial flow results are shown here to illustrate the effectiveness of the new method. Results include both step-response solutions and frequency-response solutions for a variety of pressure loadings; and the results are compared with closed-form solutions above the disk, in the plane of the disk, and below the plane of the disk (both in the wake and outside of the wake). Several example correlations are given in the figures appended to this abstract.

Figure 4-2 to Figure 4-7 show the real and imaginary part of the z component of flow (perpendicular to the disk plane in the direction of the free-stream) for a frequency-response of the pressure field. Each set gives the real part and imaginary part of the response (i.e., the $\cos(\omega\tau)$ and $\sin(\omega\tau)$ coefficients). Velocity is plotted on a plane one rotor radius below the rotor disk $z=1$ ($\xi=1$) where the rotor wake is the region $-1<x<1$.

Figure 4-2 and Figure 4-3 are for an elliptical pressure oscillation, and Figure 4-4 and Figure 4-5 are for oscillations of a cyclic pressure distribution. Velocity distributions are shown for both static pressure ($\omega=0$) and for dynamic pressure ($\omega=4$). Even though there are several kinks in the exact velocity responses for dynamic pressure, our co-state method can still match these kinks very well.

Figure 4-6 and Figure 4-9 give the normal velocity versus z both at $x_0=0.5$ (i.e., on a streamline passing through the disk at $r_0=0.5$) and at the point $x_0=1.2$ (i.e., a streamline that is outside of the disk, passing through $r_0=1.2$). Figure 4-6 and Figure 4-7 are for an elliptical pressure distribution, while Figure 4-8 and Figure 4-9

are for a cyclic pressure distribution. Negative ξ is upstream (above the disk) and positive ξ is downstream (below the plane of the disk). For all these figures, the velocity begin oscillating while ξ is bigger than 0. $x_0 = 0.5$ is within the wake, and $x_0 = 1.2$ is outside the wake region.

Figure 4-10 to Figure 4-13 show the results for comparisons of the co-state method with even terms equal to odd terms against results for no even terms for a large skew angle ($\chi = 75°$). The blue solid lines in each figure are obtained with the whole matrix, which contains both even and odd terms, while the red dash lines are based on odd terms only. Figure 4-10 and Figure 4-11 are for static pressure ($\omega = 0$), and the results from both methods are almost exact with the results from convolution method. Figure 4-12 and Figure 4-13 are for dynamic pressure ($\omega = 4$), however, the results with even terms are much more accurate than the results with only odd terms on the disk region.

Figure 4-14 and Figure 4-15 are responses to a step input in elliptical pressure versus time within and without wake region. Figure 4-14 is velocity at a point one radius below the disk and 0.5 radii from the center, and Figure 4-15 is also at one radius below the disk, but 1.2 radii from the center. Figure 4-16 and Figure 4-17 are step responses for cyclic pressure distribution at one radius below the rotor disk, and Figure 4-16 is within the wake ($x = 0.5$) and Figure 4-17 is outside the wake ($x = 0.5$).

Figure 4-18 and Figure 4-19 are velocities versus streamline location at a reduced time of $\tau = 1$ at 0.5 radii from the center and 1.2 radii from the center respectively. Figure 4-20 and Figure 4-21 are snapshots for the responses for a cyclic pressure at fixed time $\tau = 1$ within and without wake region. The figures reveal the establishing process of the inflow blow the rotor disk.

Since at the time $\tau = 1$ the wake region is not fully developed, we will take a snapshot of $\tau = 10$ to see what a fully developed wake region would be like. Figure

4-22 and Figure 4-23 are velocities along streamline at a reduced time of $\tau = 10$ at 0.5 radii away from center for elliptical and cyclic pressure distribution. From Figure 4-22 we can tell that the velocity at the rotor disk (which is $\xi = 0$) is around 1.49, and the fully velocity value is around 2.96 (at $\xi = 5$). The numerical result is consistent with the well know conclusion from momentum theory for rotary wing systems that the induced velocity in the far wake is as twice as the velocity at the rotor disk. The same thing for Figure 4-23, which is with -1.18 at the rotor disk and -2.37 in the far wake (at $\xi = 5$).

For all the figures, an exact solution is compared to the finite state solution with 20 regular states (10 odd and 10 even functions) and 20 co-states. One can see that the agreement is virtually exact. For the frequency response, even the discontinuity in slope at the wake edge is found correctly. For the step response, the convection of the start-up system downstream is also found correctly—both in and out of the wake. In Morrilo's desperation, he showed that the velocity also converges upstream ($\xi < 0$ and no co-states required); while the present results show that, with the co-states, the velocity also converges below the plane of the rotor disk ($\xi > 0$) both inside and outside of the wake.

The cost of completing the inflow theory is adding more states to calculate the additional information. For a case in which one is interested in four harmonics of the flow (along with the appropriate number of radial expansion terms), the He model (with only odd functions) would require 15 inflow states for the normal flow on the disk (for both cosine and sine terms). In order to compute all components of the flow above the disk, one must add the even functions, which increases the number of states to 30. In order to compute the flow below the disk, one must additionally compute the adjoint velocity field from another 30 co-states (60 states in all).

One point of importance is that, once the original states are found, the co-states often follow in a trivial manner. For frequency response, the adjoint is just the complex conjugate of the complex velocity field; and for a step response, each co-

state is a constant minus the original state. Even for general cases, the solution of the co-states always involves less numerical effort than the computation of the states themselves. In particular, the co-states are only needed for past time, with the range of past time equal to the depth into the wake for which the solution is desired. This can be seen in equation (4.39) in which the flow at a point ξ_0 depends on the co-states at the time at which that flow particle was at the rotor disk, $\tau - \xi_0$. Assuming one has saved the forcing functions from that duration of past time and then multiplies each τ_j^r by $(-1)^{j+1}$, then the computation of the co-states involves solution of a set of linear equations uncoupled from the rest of the rotorcraft simulation. This makes the computation very straightforward. Furthermore, since the linear adjoint equations are unstable, one time marches backwards from the present time back to $\tau - \xi_0$ with zero initial conditions at the present time. It can be shown that equation (4.39) cancels the homogeneous part of the adjoint solution, so that the initial conditions on this computation are irrelevant.

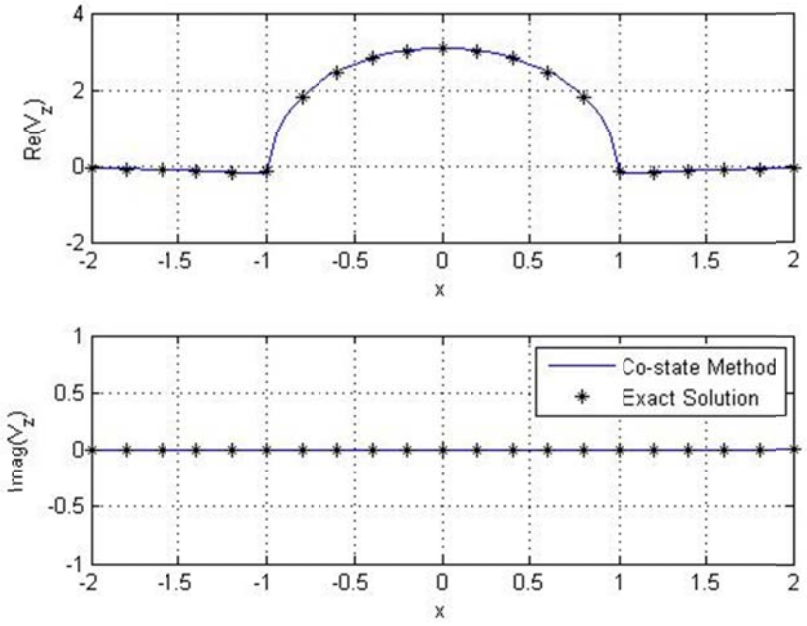

Figure 4-2 Velocity for $\xi = 1$ with τ_1^0 for $\omega = 0$, $\chi = 0^o$

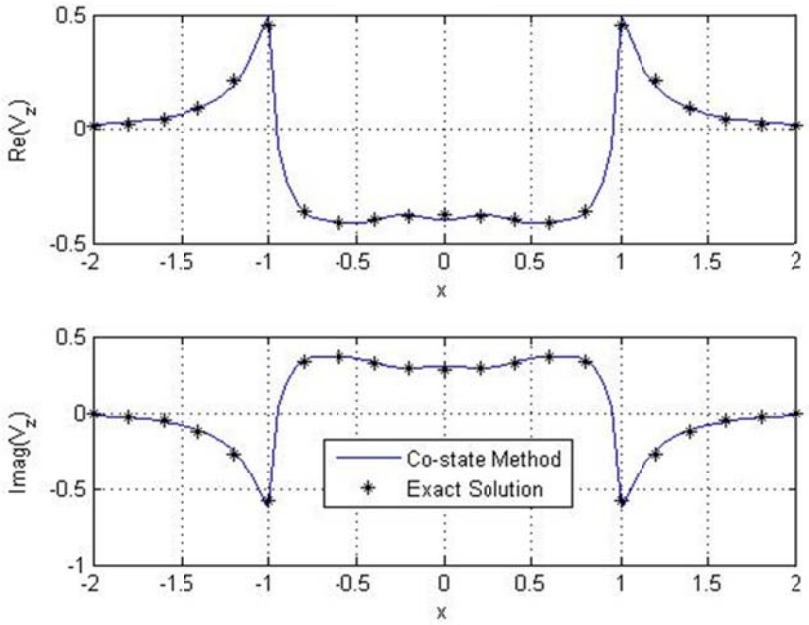

Figure 4-3 Velocity for $\xi = 1$ with τ_1^0 for $\omega = 4$, $\chi = 0^o$

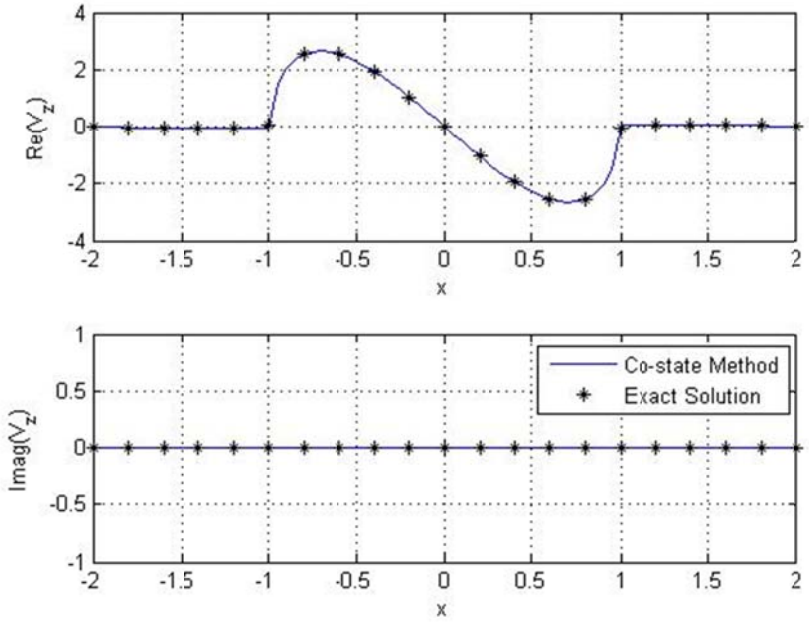

Figure 4-4 Velocity for $\xi = 1$ with τ_2^1 for $\omega = 0$, $\chi = 0^o$

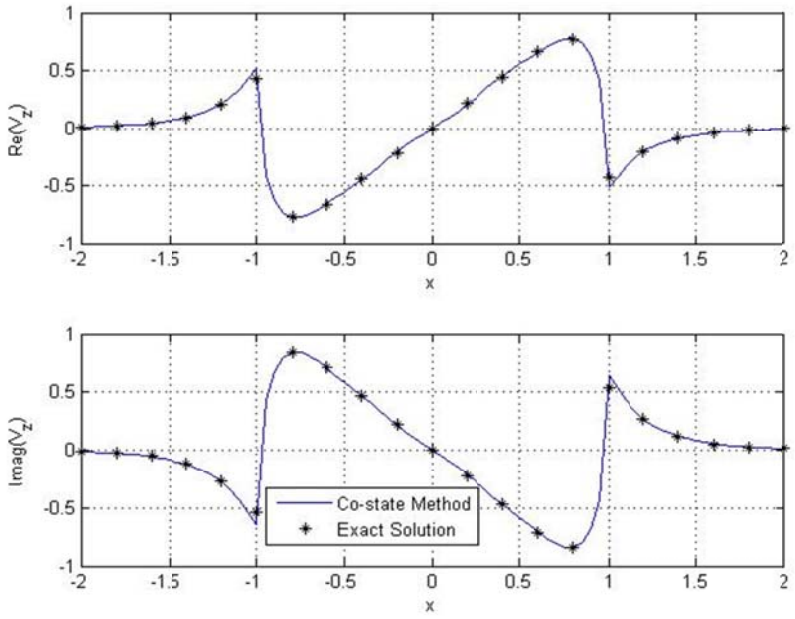

Figure 4-5 Velocity for $\xi = 1$ with τ_2^1 for $\omega = 4$, $\chi = 0^o$

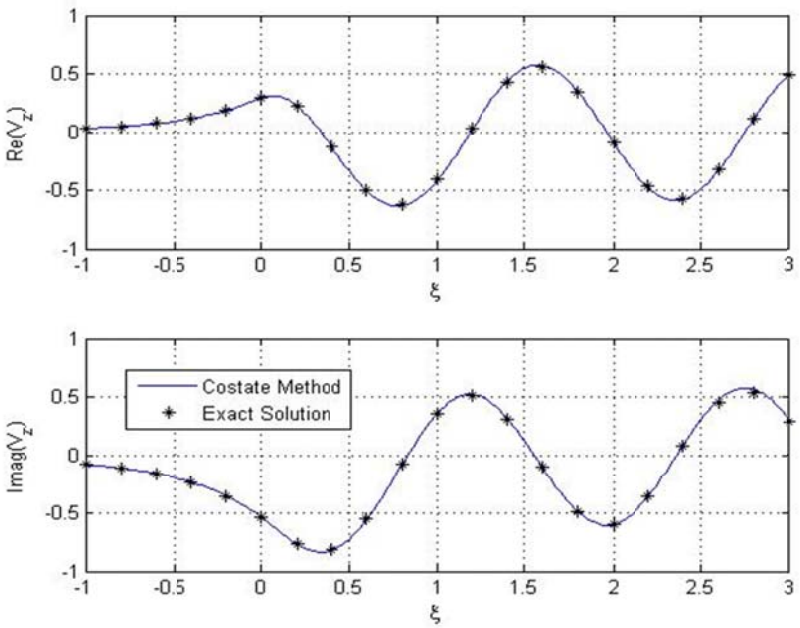

Figure 4-6 Velocity for $x_0 = 0.5$ with τ_1^0 for $\omega = 4$, $\chi = 0^o$

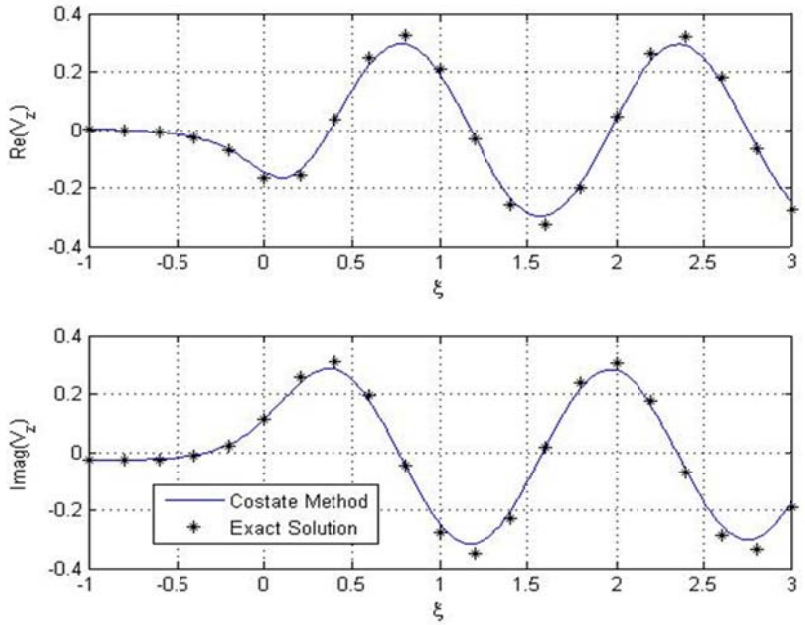

Figure 4-7 Velocity for $x_0 = 1.2$ with τ_1^0 for $\omega = 4$, $\chi = 0^o$

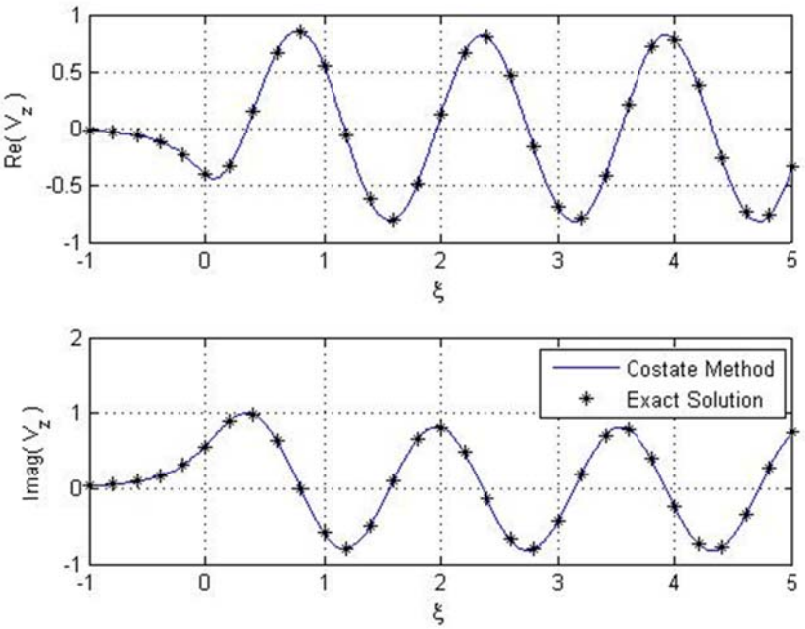

Figure 4-8 Velocity for $x_0 = 0.5$ with τ_2^1 for $\omega = 4$, $\chi = 0^o$

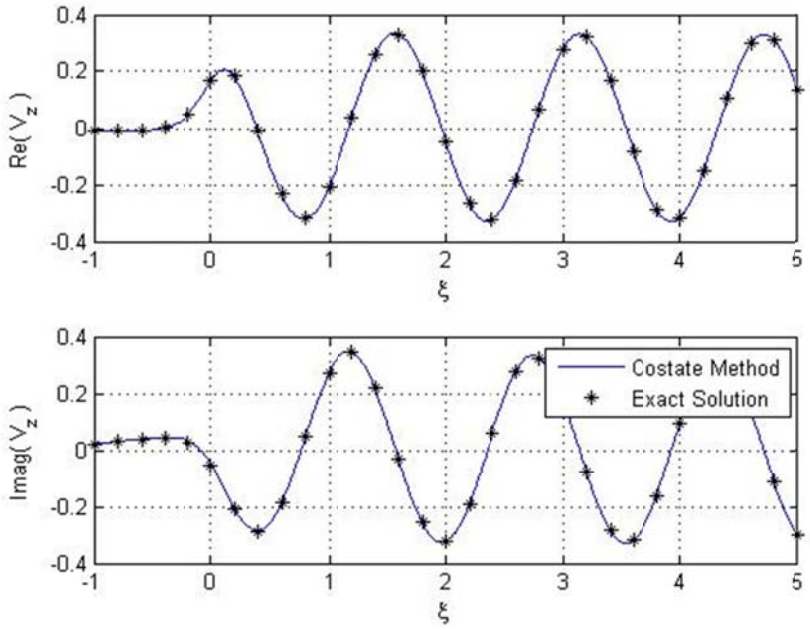

Figure 4-9 Velocity for $x_0 = 1.2$ with τ_2^1 for $\omega = 4$, $\chi = 0^o$

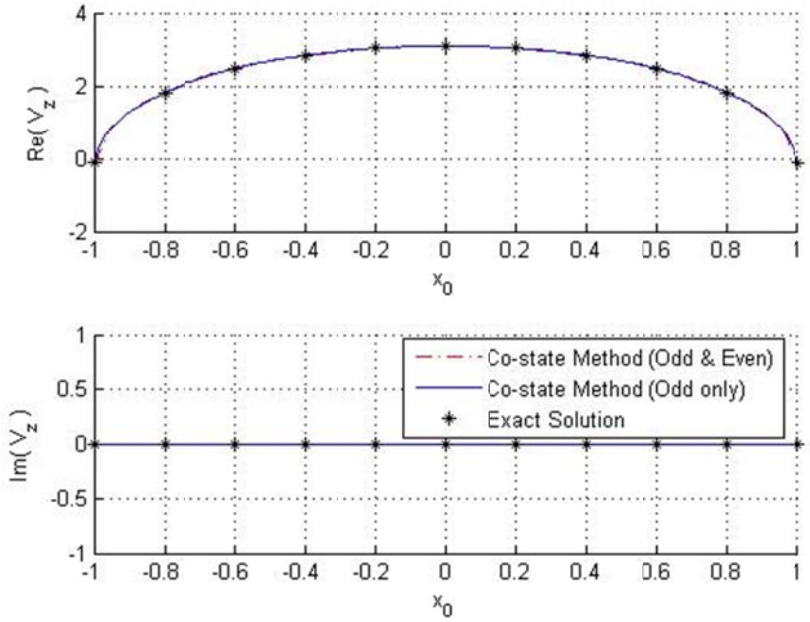

Figure 4-10 Comparison of the co-state method with different number of even terms for $\xi = 1$ with τ_1^0 for $\omega = 0$ and $\chi = 0^o$

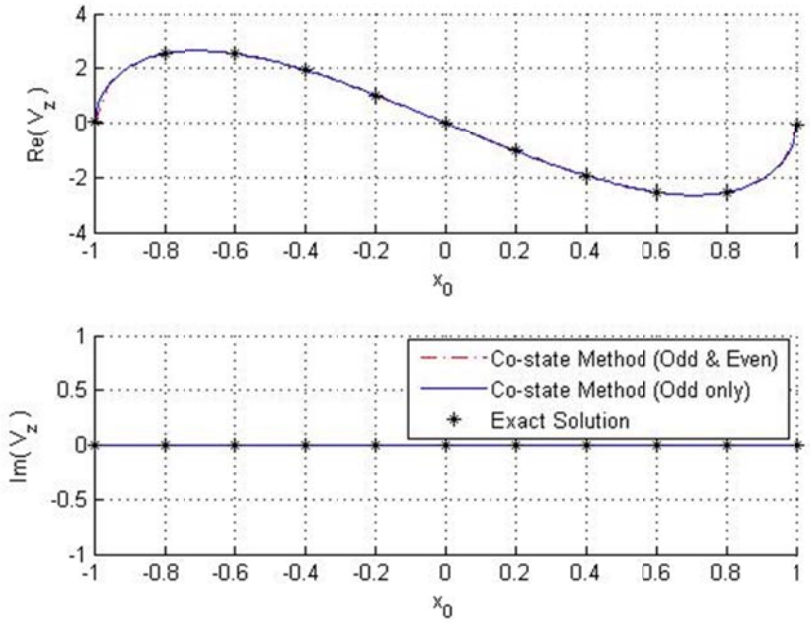

Figure 4-11 Comparison of the co-state method with different number of even terms for $\xi = 1$ with τ_2^1 for $\omega = 0$ and $\chi = 0^o$

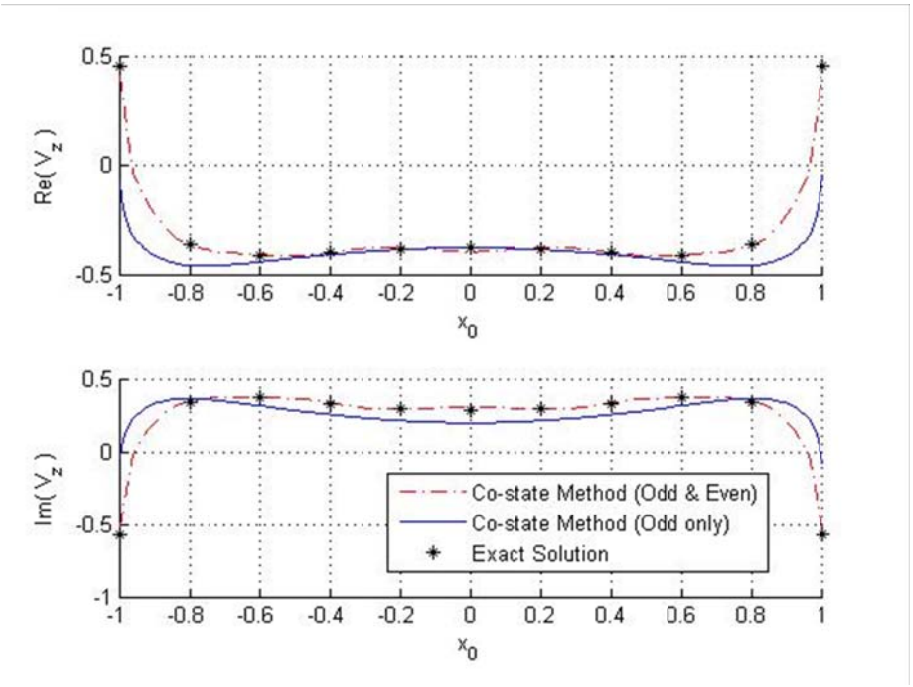

Figure 4-12 Comparison of the co-state method with different number of even terms for $\xi = 1$ with τ_1^0 for $\omega = 4$ and $\chi = 0^o$

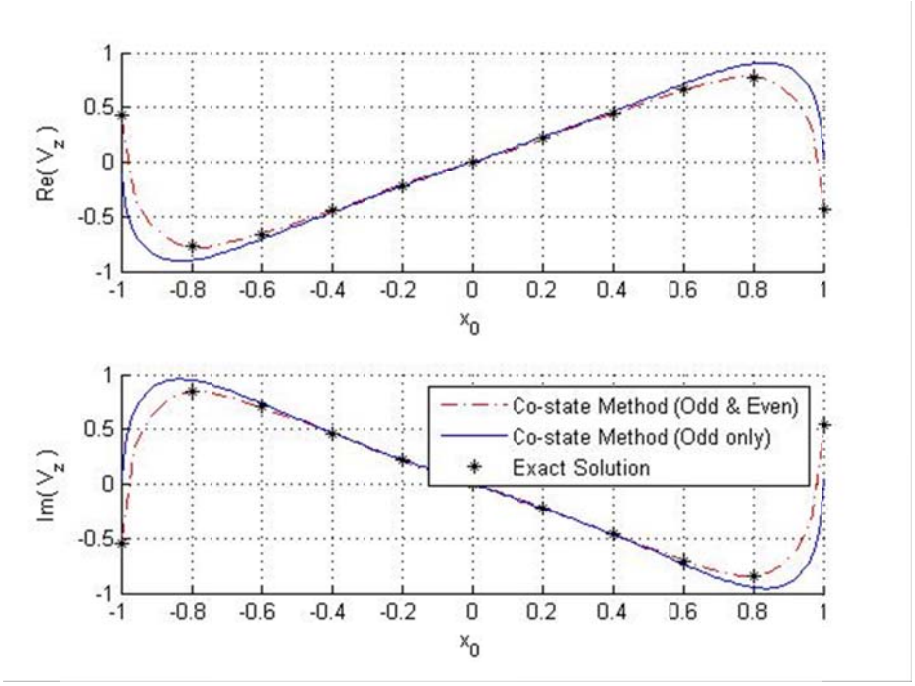

Figure 4-13 Comparison of the co-state method with different number of even terms for $\xi = 1$ with τ_2^1 for $\omega = 4$ and $\chi = 0^o$

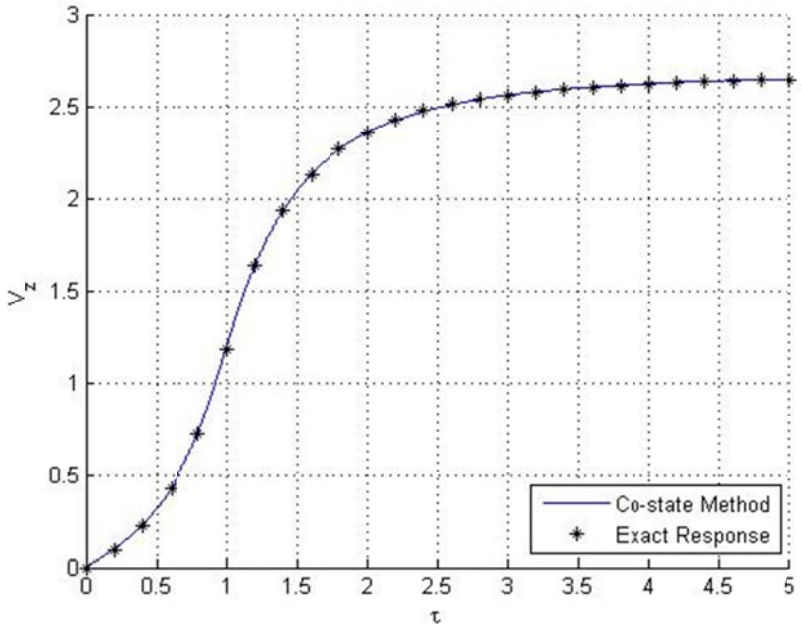

Figure 4-14 Velocity versus time for $\xi = 1,\ x_0 = 0.5$ with step response in τ_1^0

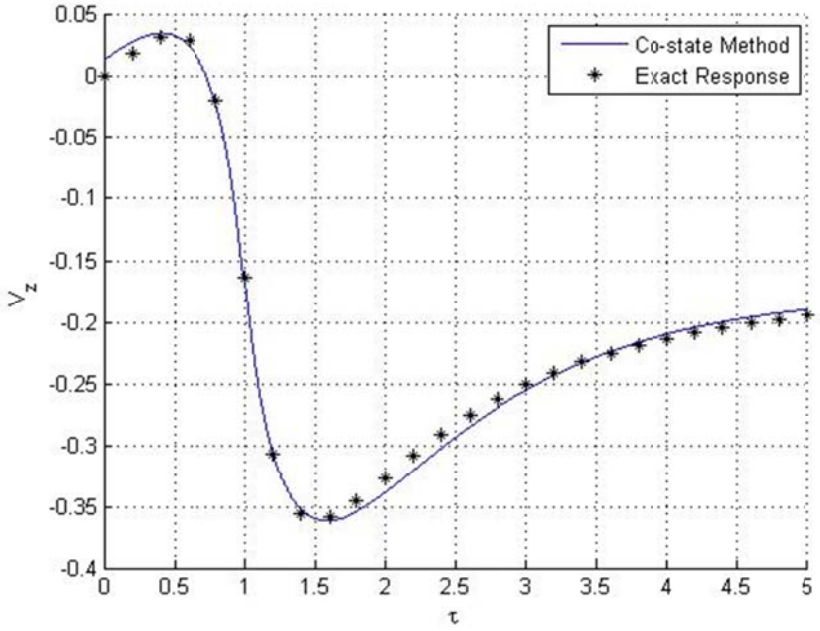

Figure 4-15 Velocity versus time for $\xi = 1,\ x_0 = 1.2$ with step response in τ_1^0

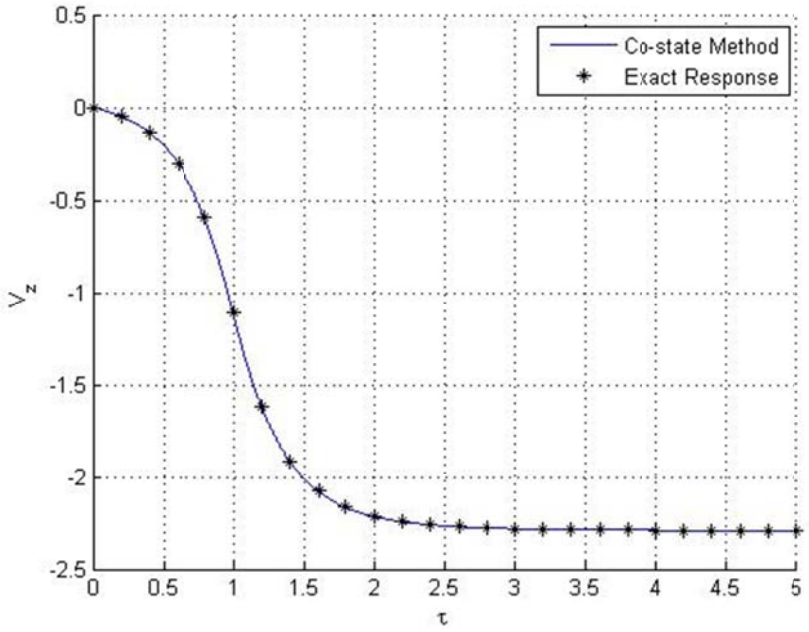

Figure 4-16 Velocity versus time for $\xi = 1,\ x_0 = 0.5$ with step response in τ_2^1

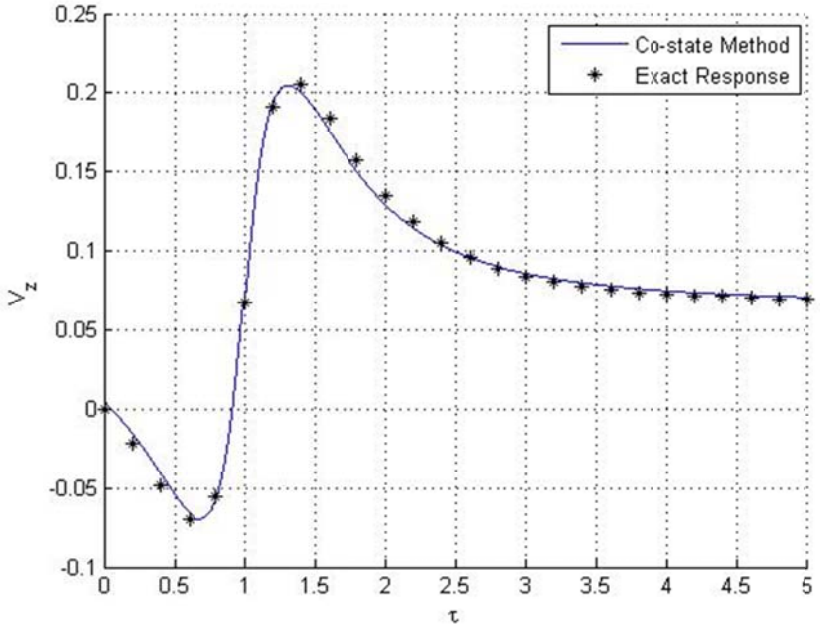

Figure 4-17 Velocity versus time for $\xi = 1,\ x_0 = 1.2$ with step response in τ_2^1

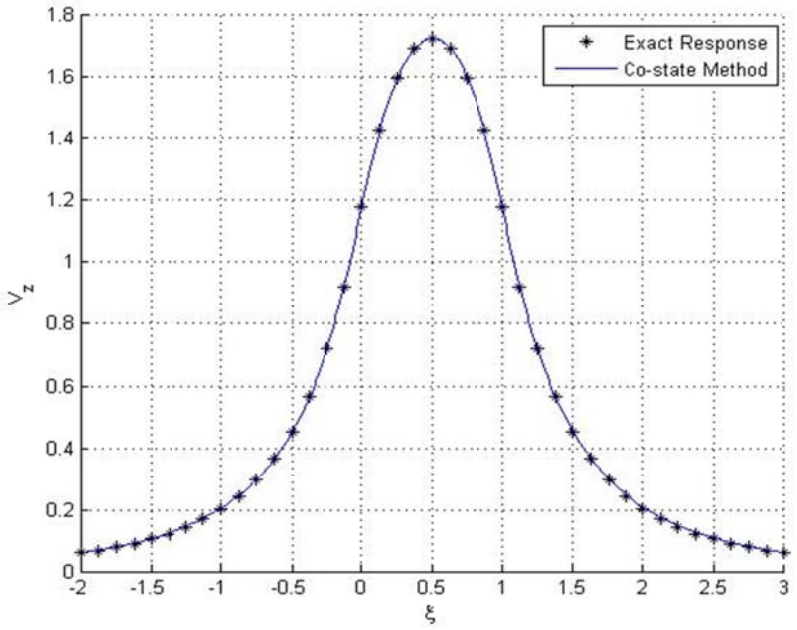

Figure 4-18 Velocity versus ξ for $\tau = 1,\ x_0 = 0.5$ with step response in τ_1^0

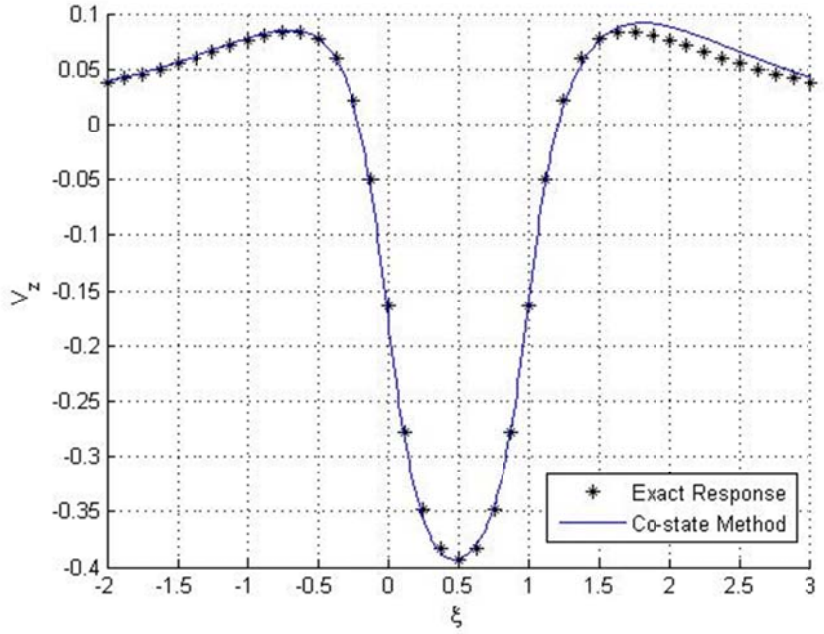

Figure 4-19 Velocity versus ξ for $\tau = 1,\ x_0 = 1.2$ with step response in τ_1^0

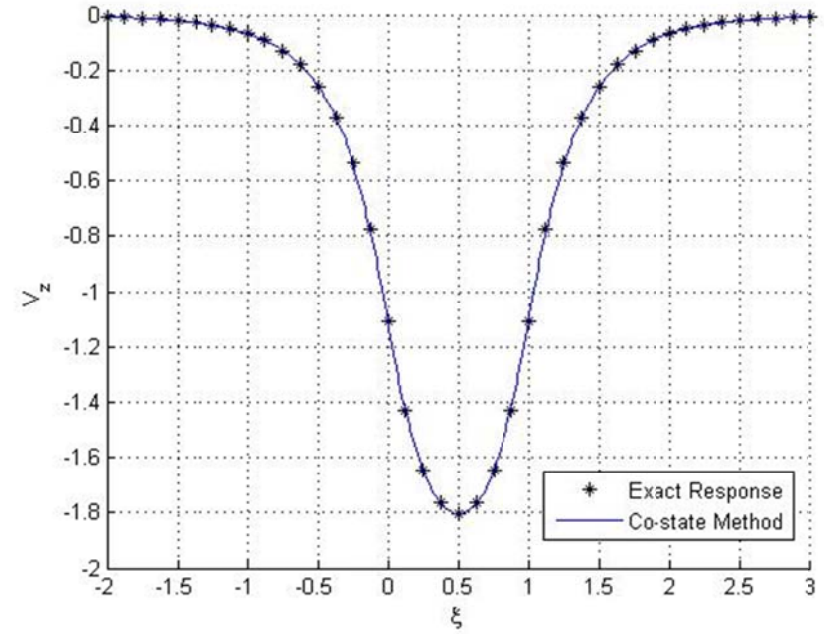

Figure 4-20 Velocity versus ξ for $\tau = 1,\ x_0 = 0.5$ with step response in τ_2^1

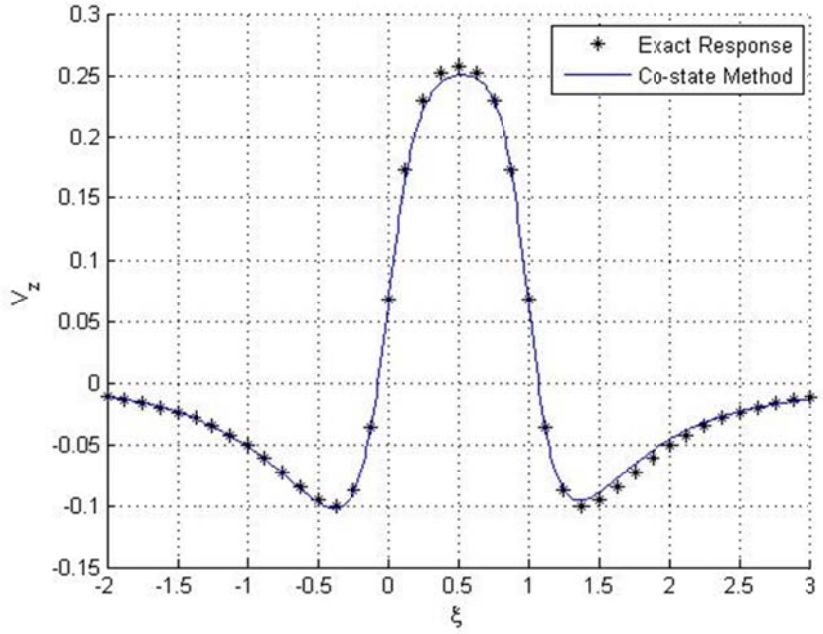

Figure 4-21 Velocity versus ξ for $\tau = 1$, $x_0 = 1.2$ with step response in τ_2^1

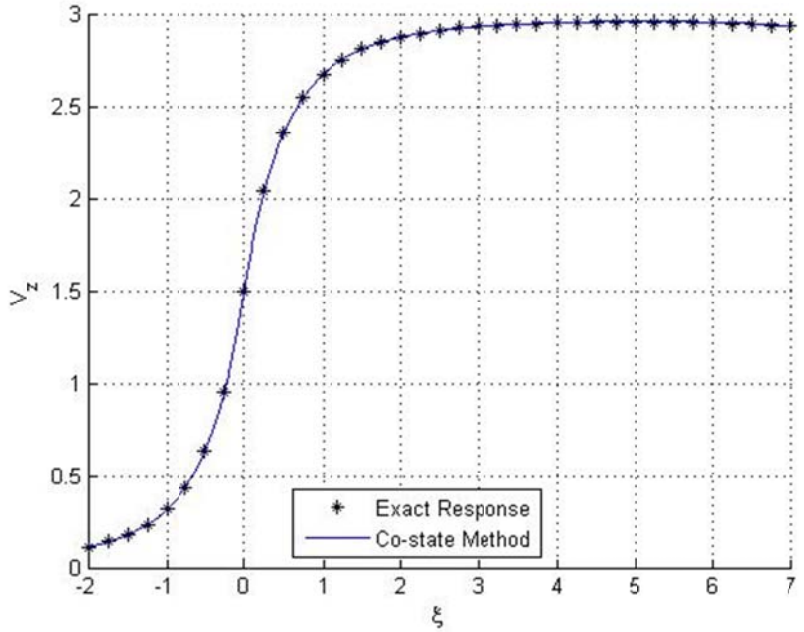

Figure 4-22 Velocity versus ξ for $\tau = 10$, $x_0 = 0.5$ with step response in τ_1^0

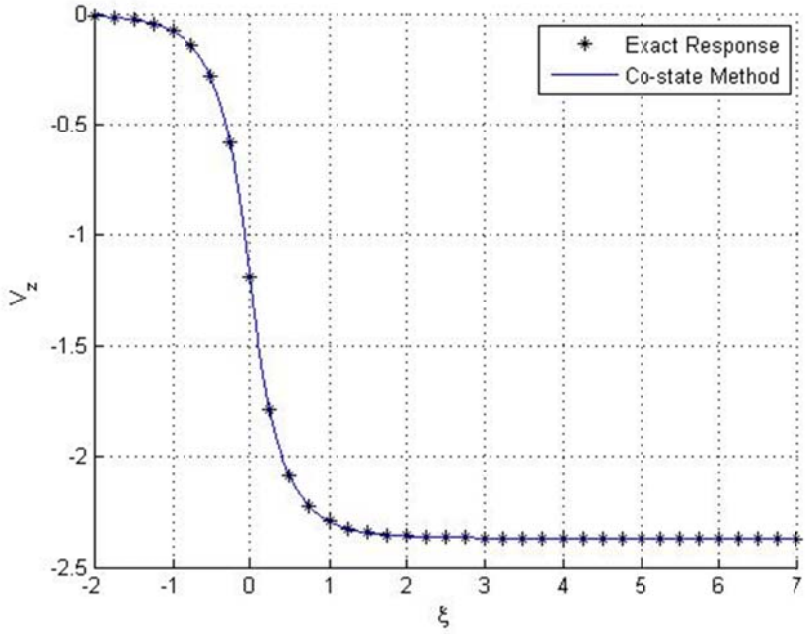

Figure 4-23 Velocity versus ξ for $\tau = 10$, $x_0 = 0.5$ with step response in τ_2^1

4.5 Results for Skewed Angle Flow

Results will now be presented to show velocity fields as obtained by the new methodology below the rotor disk for skewed angle. Here, only the z component of skewed flow are presented for a variety of pressure loadings; and the results are compared with closed-form convolution solutions in the frequency domain below the plane of the disk both in the wake and outside of the wake.

Two skewed angles, $\chi = 30^o$ and $\chi = 75^o$, and two frequencies, $\omega = 0$ and $\omega = 4$, are considered for the velocity perpendicular to the disk plane in the direction of the free-stream. Velocity is plotted on a plane one rotor radius below the rotor disk $\xi = 1$ where the rotor wake is the region $-1 < x_0 < 1$.

For the results labeled "Co-State Method" (i.e., with the adjoint variables used to compute the velocities), we set the maximum harmonic number to 10. Figure 4-24 to Figure 4-31 show the real and imaginary parts for a frequency-response of a pressure field with different skew angles. Figure 4-24 through Figure 4-27 show the

frequency response to the first collective pressure input, Φ_1^0. In Figures Figure 4-24 and Figure 4-26, there are no imaginary parts in the solution since they are for the responses of static pressure ($\omega = 0$). In Figure 4-24 and Figure 4-25 ($\chi = 30^o$), the co-state method gives excellent convergence both on-disk and off disk; however, in Figure 4-26 and Figure 4-27 ($\chi = 75^o$), the convergence of the co-state method is slow and with oscillations. This is typical also of the convergence on the disk, and will be discussed shortly.

Figure 4-28 through Figure 4-31 are for oscillations of a cyclic pressure distribution, Φ_2^1. Figure 4-28 and Figure 4-30 give the static pressure ($\omega = 0$) responses, and Figure 4-29 and Figure 4-31 give the velocity distributions for dynamic pressure ($\omega = 4$). Again, we can see that the results for small skew angle $\chi = 30^o$ is essentially exact, but for large skew angle $\chi = 75^o$, it is still good but not completely converged. The convergence is better for this cyclic response than it was for collective pressure response. In general, the convergence of the lowest collective mode is always the slowest.

Figure 4-32 through Figure 4-35 are responses to an elliptical pressure oscillation with different skewed angle. The normal component of velocity is given versus ξ all at $x_0 = 0.5$ (i.e., on a streamline passing through the disk at $r_0 = 0.5$). Figure 4-32 and Figure 4-34 are with $\omega = 0$, so no imaginary parts are displayed. We can see good agreement between the closed form solutions and the co-state method within the streamline cylinder which contains the rotor disk.

Figure 4-36 through Figure 4-39 are responses to a cyclic pressure distribution with different skewed angle. Normal velocity is given versus ξ with $\omega = 4$. Here, velocities are shown both inside and outside of wake region. Again, for small skew angle ($\chi = 30^o$), we have almost the identical results as from convolution. For large skew angle ($\chi = 75^o$), the result along a streamline within the cylinder ($x_0 = 0.5$) is virtually exact, Figure 4-38; but for $x_0 = 1.2$ (outside of the rotor disk), a small error

occurs, Figure 4-39. This follows directly from the corresponding error on the rotor disk in the Peters-Morrilo model with $\chi = 75^o$ (See Ref. [6]).

The error on the disk with the Morillo model has been shown to converge the best when fewer even terms are included as the skew angle increases). In fact, the optimum is such that—when all even terms are eliminated at 90º skew angle—the He result with no even terms is exact. It would therefore seem that the adjoint method could also be improved by an optimization of even potential functions with skew angle. (Presently even terms equal odd.)

Figure 4-40 through Figure 4-43, show comparisons of the co-state method with even terms equal to odd terms against results for no even terms for a large skew angle ($\chi = 75^o$). The blue solid lines in each figure are obtained with odd terms only, and the red dash lines are based on the whole matrix, which contains both even and odd terms. From these figures, one can tell that the results obtained from the co-state method with only odd terms are more accurate than the ones with both odd and even terms for big skewed angles. Combined with Figure 4-10 through Figure 4-13 for axial flow, one will know that there should be an optimized even terms for different skewed angles. This verifies the findings of Morillo that the number of even terms should be optimized on the basis of skew angle.

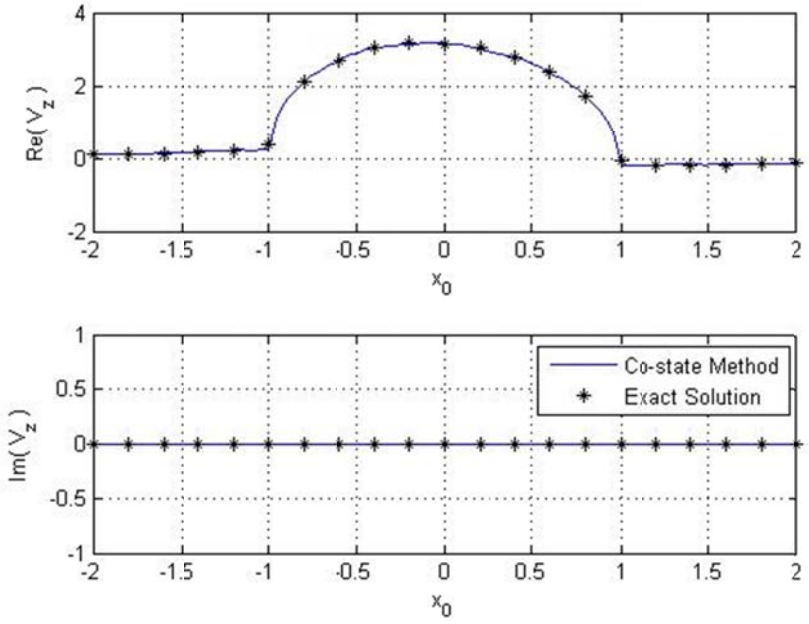

Figure 4-24 Velocity for $\xi = 1$ with τ_1^0 for $\omega = 0$ and $\chi = 30^o$

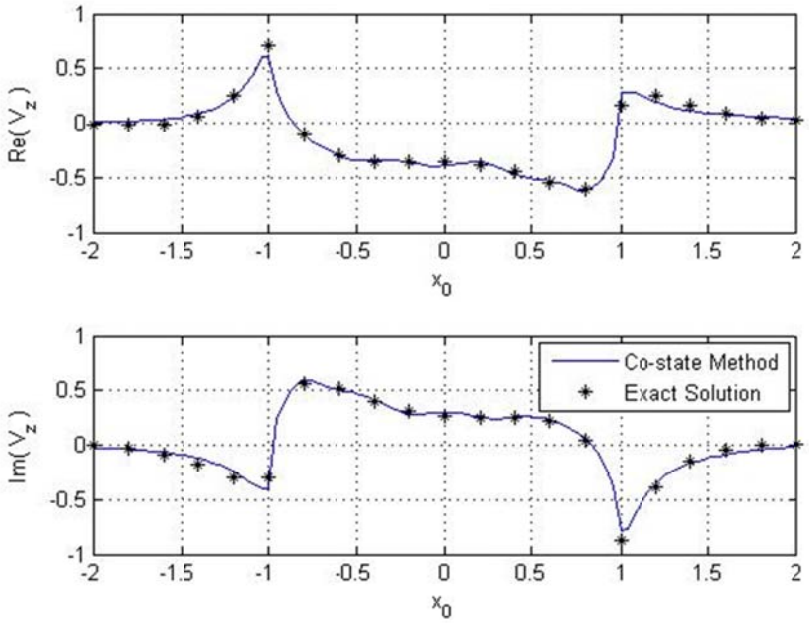

Figure 4-25 Velocity for $\xi = 1$ with τ_1^0 for $\omega = 4$ and $\chi = 30^o$

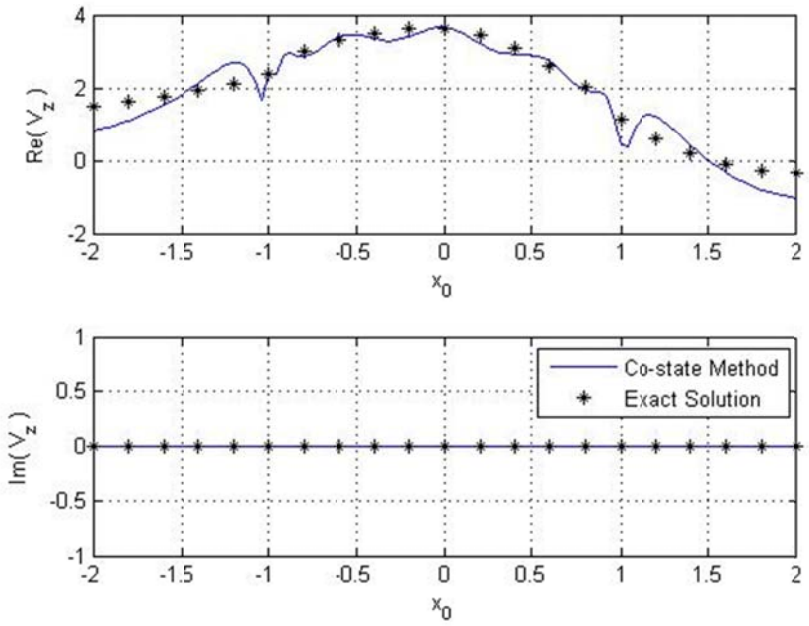

Figure 4-26 Velocity for $\xi = 1$ with τ_1^0 for $\omega = 0$ and $\chi = 75^o$

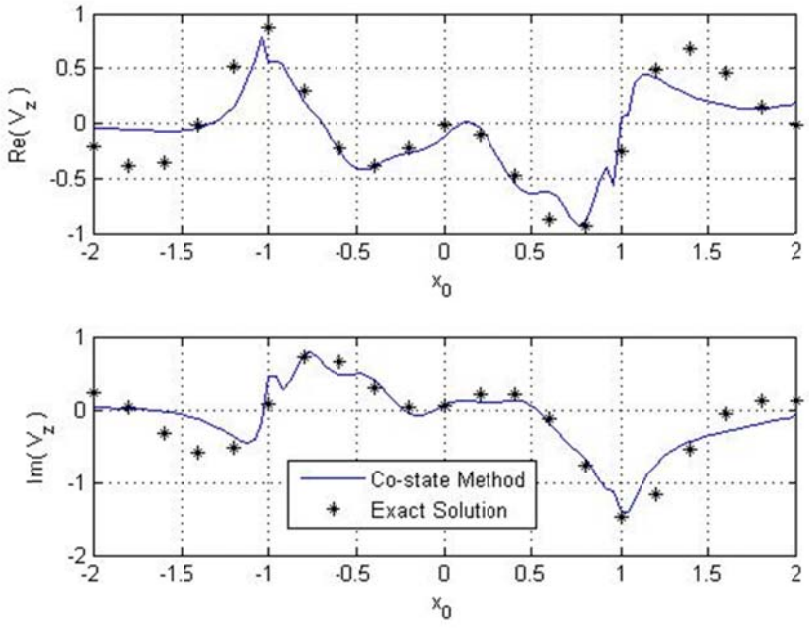

Figure 4-27 Velocity for $\xi = 1$ with τ_1^0 for $\omega = 4$ and $\chi = 75^o$

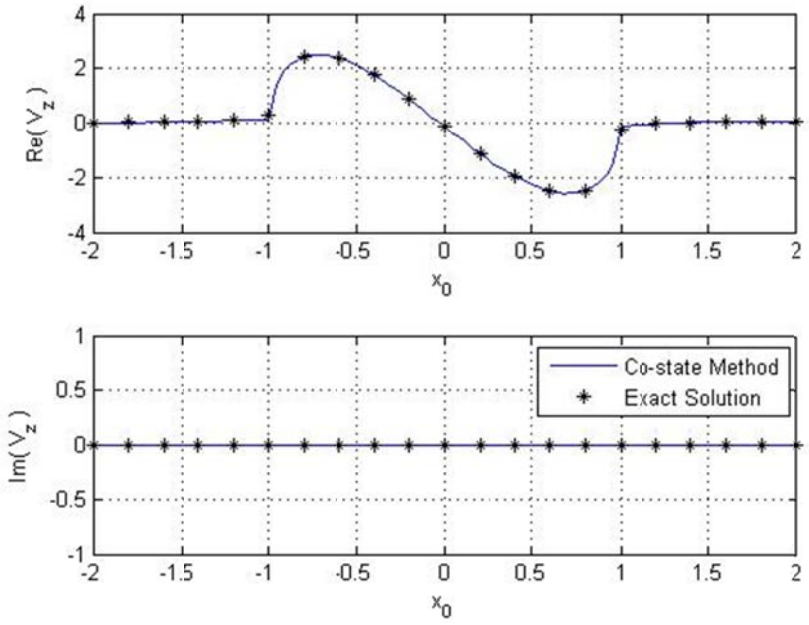

Figure 4-28 Velocity for $\xi = 1$ with τ_2^1 for $\omega = 0$ and $\chi = 30^o$

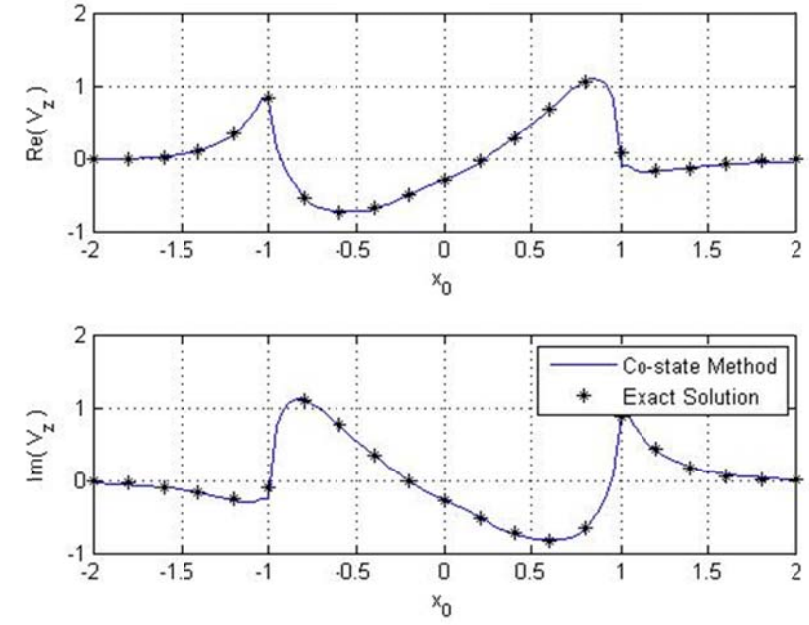

Figure 4-29 Velocity for $\xi = 1$ with τ_2^1 for $\omega = 4$ and $\chi = 30^o$

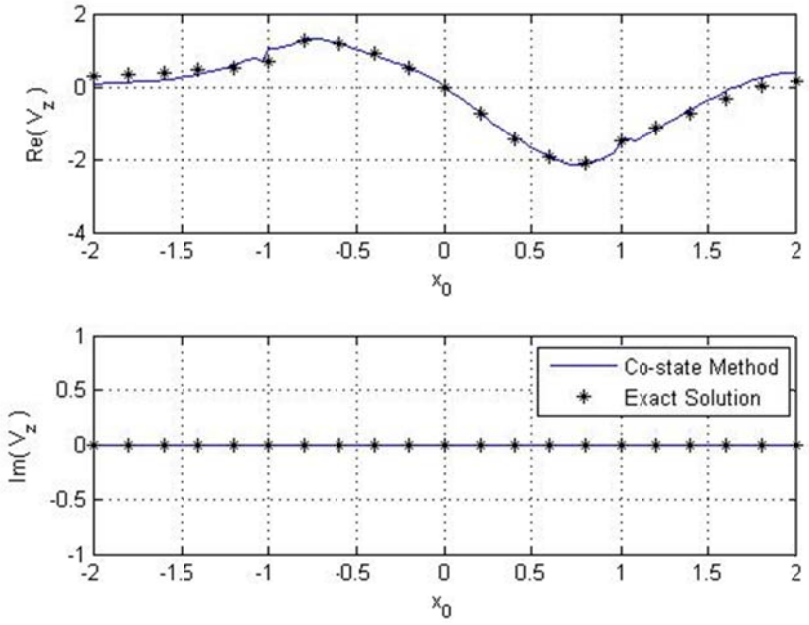

Figure 4-30 Velocity for $\xi = 1$ with τ_2^1 for $\omega = 0$ and $\chi = 75^o$

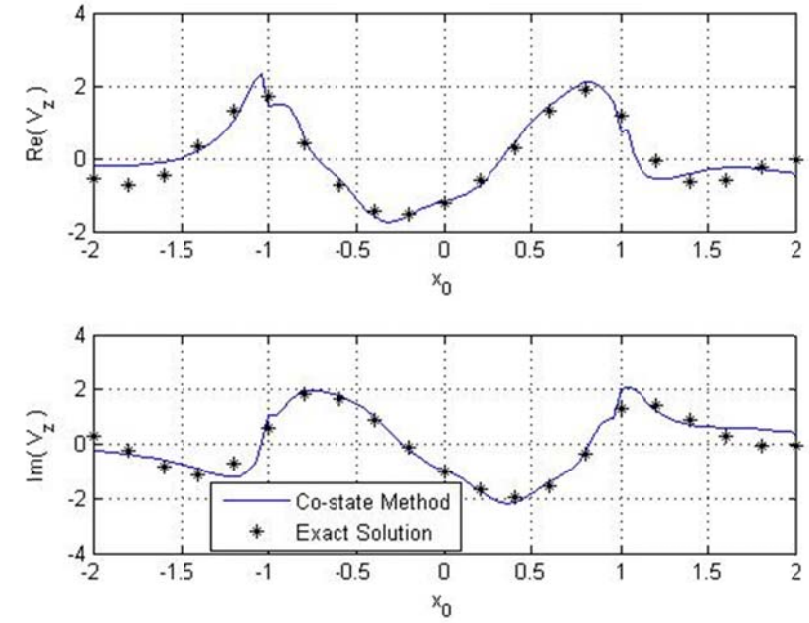

Figure 4-31 Velocity for $\xi = 1$ with τ_2^1 for $\omega = 4$ and $\chi = 75^o$

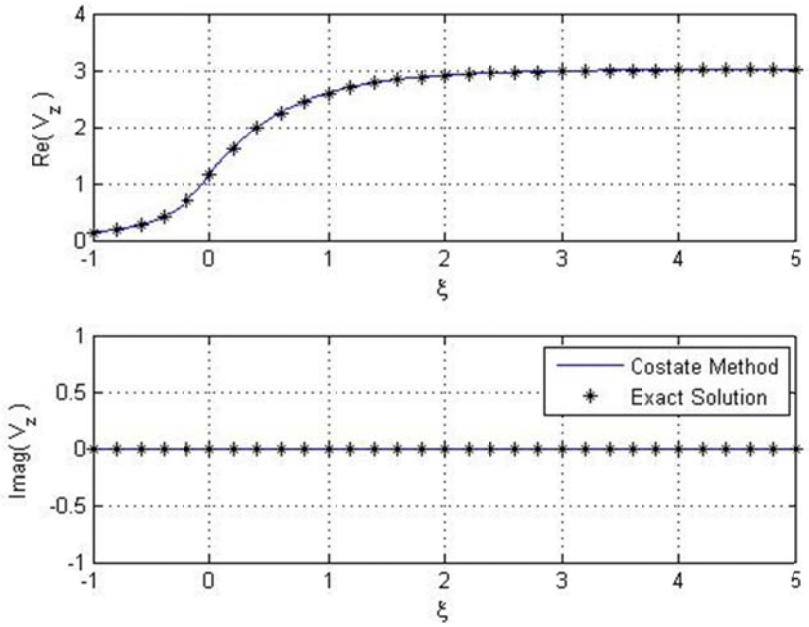

Figure 4-32 Velocity for $x_0 = 0.5$ with τ_1^0 for $\omega = 0$ and $\chi = 30^o$

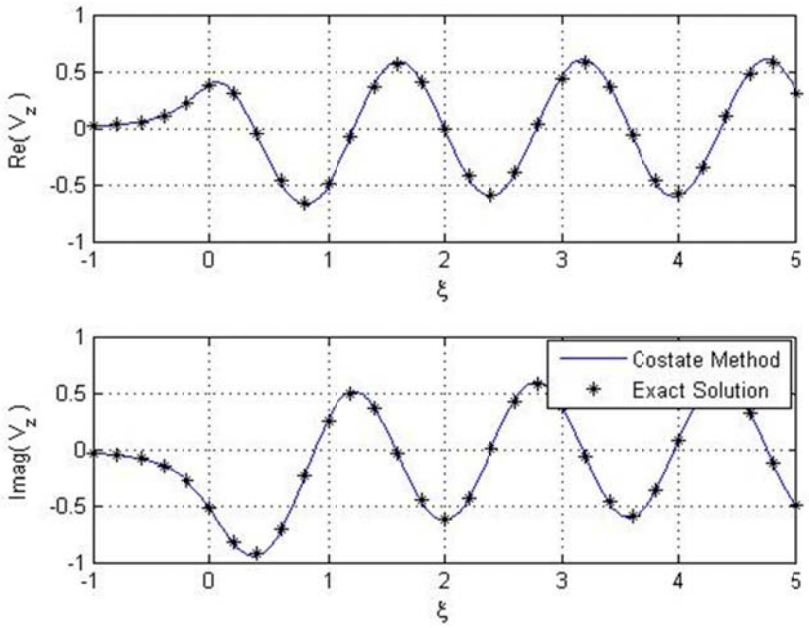

Figure 4-33 Velocity for $x_0 = 0.5$ with τ_1^0 for $\omega = 4$ and $\chi = 30^o$

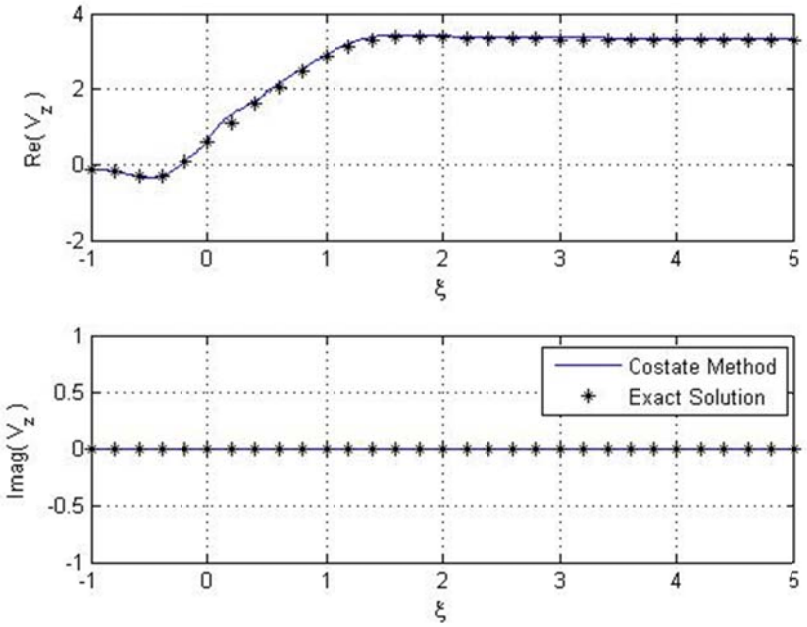

Figure 4-34 Velocity for $x_0 = 0.5$ with τ_1^0 for $\omega = 0$ and $\chi = 75^o$

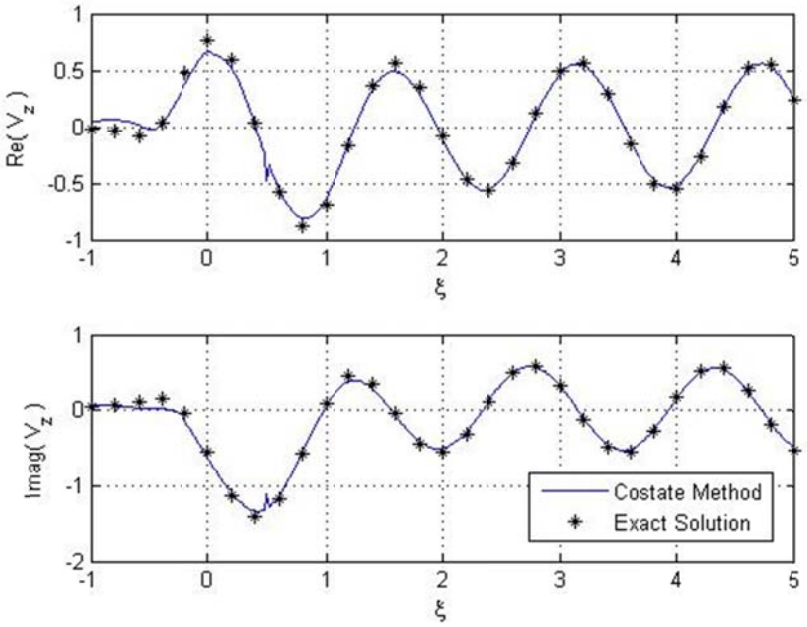

Figure 4-35 Velocity for $x_0 = 0.5$ with τ_1^0 for $\omega = 4$ and $\chi = 75^o$

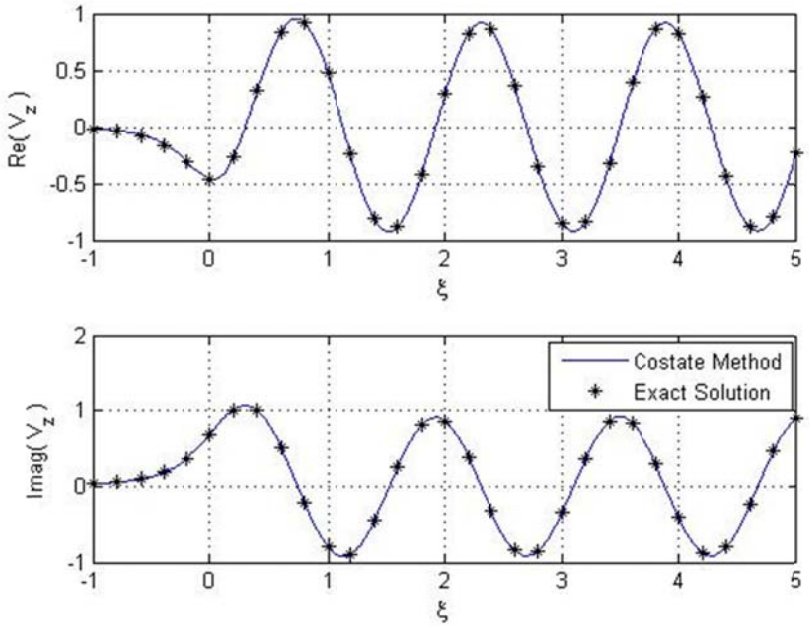

Figure 4-36 Velocity for $x_0 = 0.5$ with τ_2^1 for $\omega = 4$ and $\chi = 30^o$

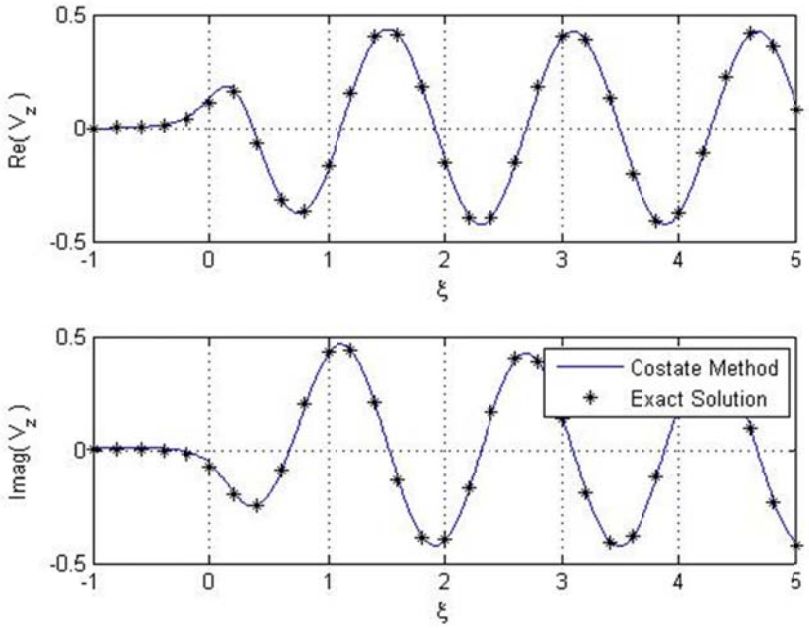

Figure 4-37 Velocity for $x_0 = 1.2$ with τ_2^1 for $\omega = 4$ and $\chi = 30^o$

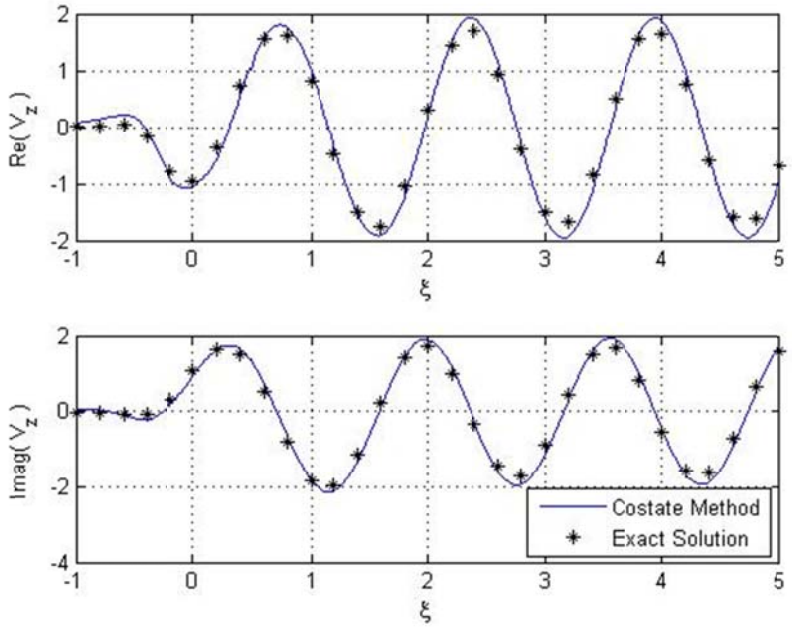

Figure 4-38 Velocity for $x_0 = 0.5$ with τ_2^1 for $\omega = 4$ and $\chi = 75^o$

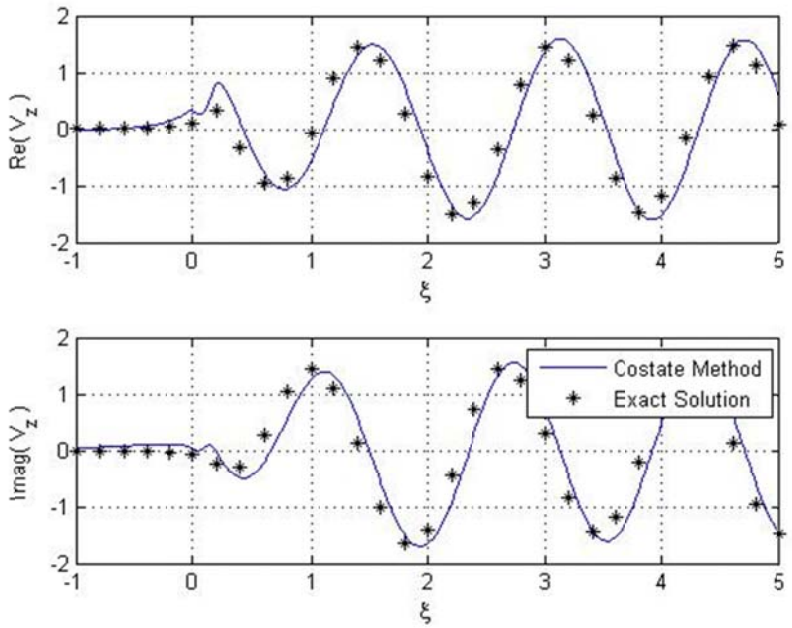

Figure 4-39 Velocity for $x_0 = 1.2$ with τ_2^1 for $\omega = 4$ and $\chi = 75^o$

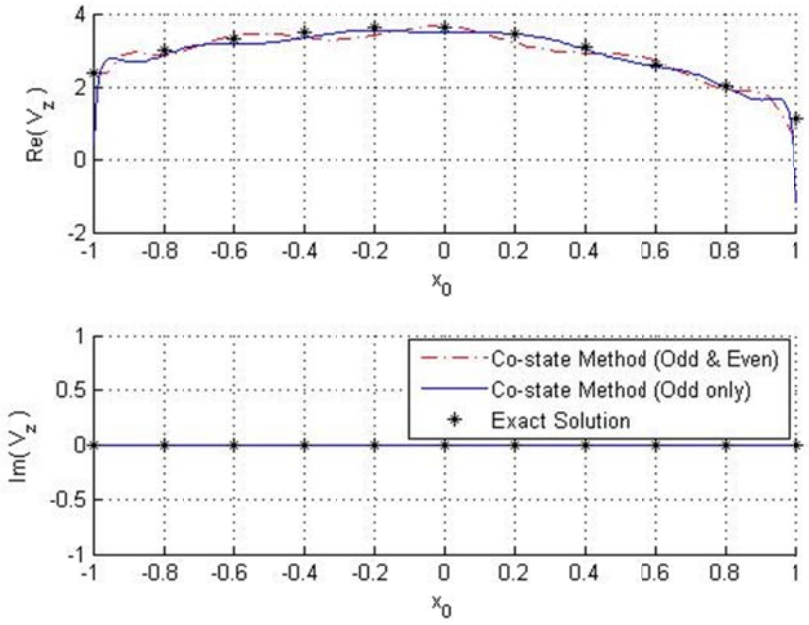

Figure 4-40 Comparison of the co-state method with different number of even terms for $\xi = 1$ with τ_1^0 for $\omega = 0$ and $\chi = 75^o$

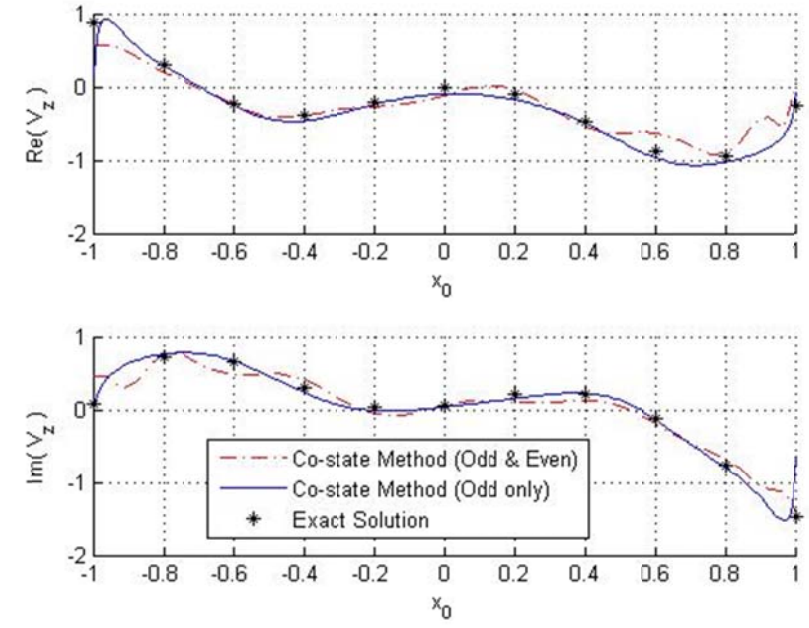

Figure 4-41 Comparison of the co-state method with different number of even terms for $\xi = 1$ with τ_1^0 for $\omega = 4$ and $\chi = 75^o$

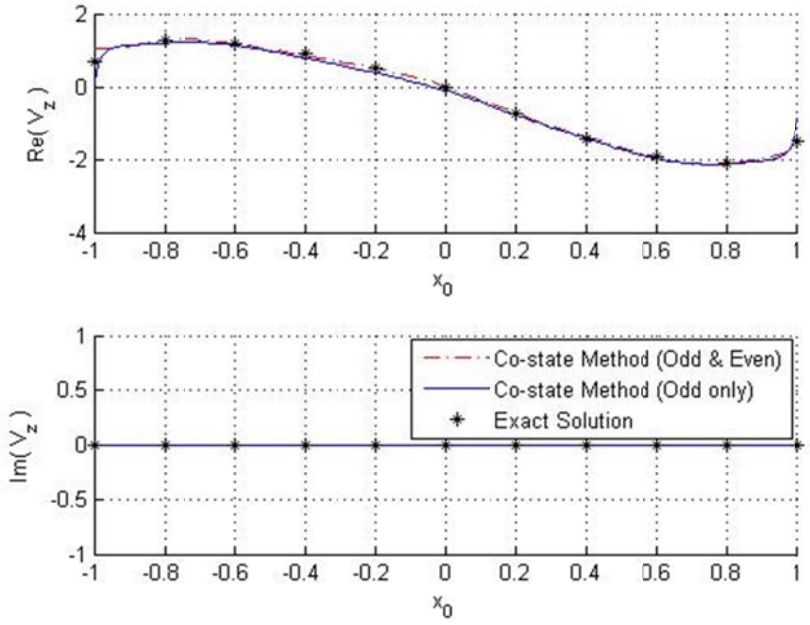

Figure 4-42 Comparison of the co-state method with different number of even terms for $\xi = 1$ with τ_2^1 for $\omega = 0$ and $\chi = 75^o$

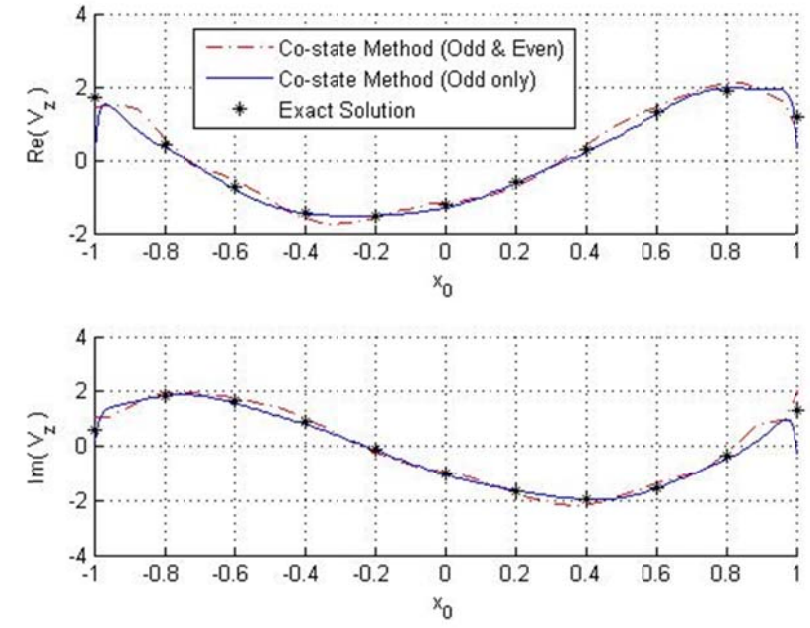

Figure 4-43 Comparison of the co-state method with different number of even terms

4.6 Validation against Experimental Data

It will be helpful to review some former results that correlate the theory with real experimental data from rotary wing systems.

In Ref. [15], the results from Peters-He model were compared with the experimental data from the laser Doppler velocimetry (LDV) measurements conducted in the AEROTECH. A two-bladed Bell 212 teetering tail rotor is used for the test. It compares induced velocity at $z = 0.04$, which is slightly above the rotor disk, with different radical positions vs. special position.

Figure 4-44 and Figure 4-45 show the comparisons of azimuthal variations in inflow velocity at $\bar{r} = 0.765$ and $\bar{r} = 0.824$. Excellent agreement can be seen everywhere on the flowfield with the exception of the size of the doublet spike due to the blade passage. The reason for smaller spikes predicted by the model than in the experimental data is that the model is truncated to 24 harmonics. When more harmonics are added, the computed spikes increase, but the lift will stay the same since the inflow at the center of the doublet remains the same.

Figure 4-46 shows the results with dynamic pitch for a collective mode. The comparison is good except the spikes near the blade passage again.

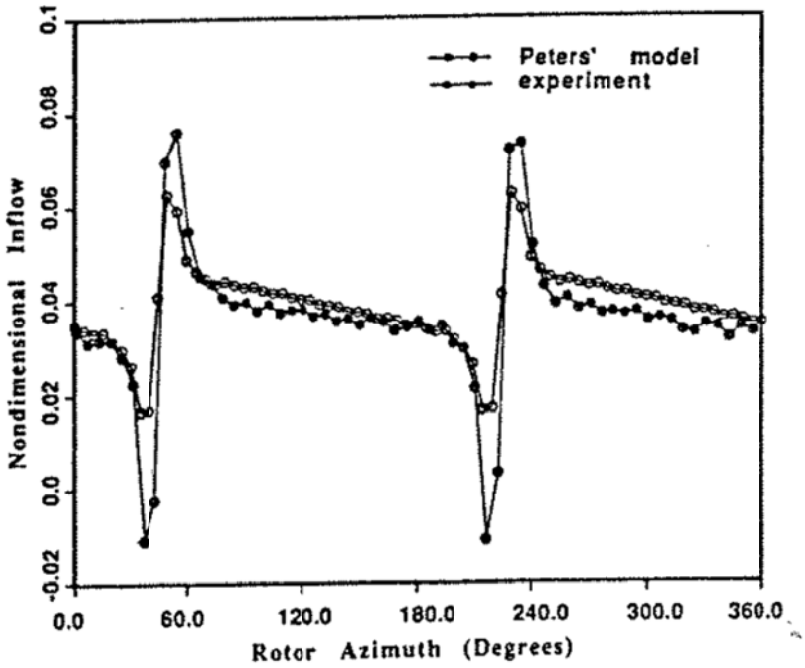

Figure 4- 44 Comparisons of calculated inflow with measured data at $\psi = 45^{o}$ vs spatial position of reference blade: $M = 24$, $\bar{r} = 0.765$; $\sigma a = 0.9$, $\theta = 4^{o}$

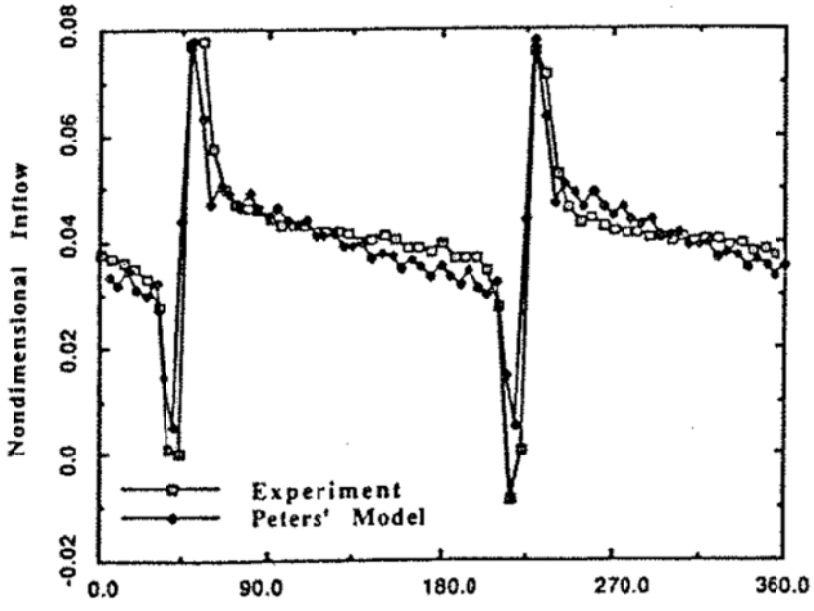

Figure 4-45 Comparisons of calculated inflow with measured data at $\psi = 45^{o}$ vs spatial position of reference blade: $M = 24$, $\bar{r} = 0.824$; $\sigma a = 0.9$, $\theta = 4^{o}$

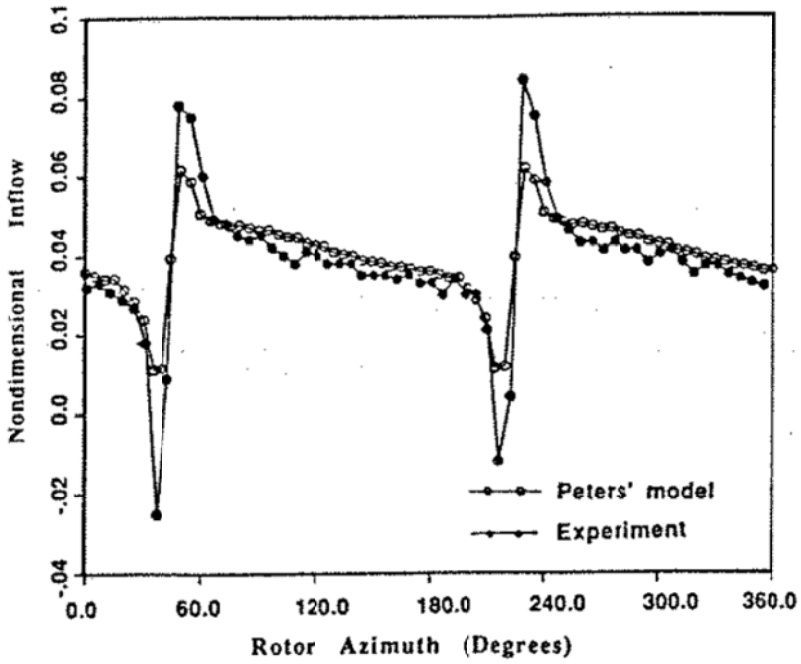

Figure 4-46 Comparisons of calculated inflow with measured data at $\psi = 45^{o}$ vs spatial position of reference blade: $M = 24$, $\bar{r} = 0.765$; $\sigma a = 0.9$, $\theta = 4^{o} + 1^{o}\cos 4\left(t - 52^{o}\right)$

A recent study on a coaxial rotor in hover with finite state models also reveals the correlation between the finite state models and the experimental data, Ref [16]. In Fig. 4-47, the Galerkin model predictions of axial and radial flow velocities at various axial locations from the lower rotor for a separation distance of 0.1D are compared with PIV data from the experiment. Positive z values represent axial locations below the lower rotor and negative z values represent axial locations above the lower rotor. From this figure, we can tell that the predictions of flow velocities from the Galerkin method based inflow model correlate well both qualitatively and quantitatively with experimental data.

In Figs 4-48 and 4-49, the thrust coefficient and torque predictions for coaxial rotor configuration as a function of separation distance are compared with experimental data for the extended Peters-He inflow model and the Galerkin method based inflow model respectively. Both methods correlate well with the experimental thrust measurements over the range of separation distances.

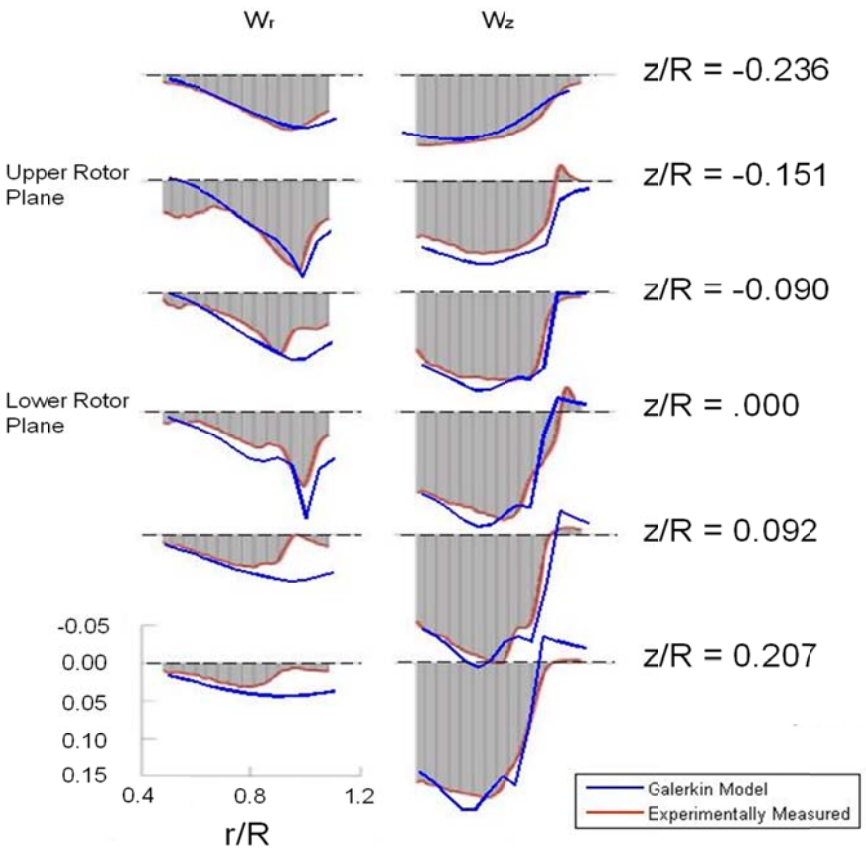

Figure 4-47 Comparisons of predicted axial and radial induced velocities at various axial locations with PIV data for a coaxial rotor configuration of $0.1D$ separation distance. (The lower rotor is located at $z = 0$ with positive z below the lower rotor and negative z above it.)

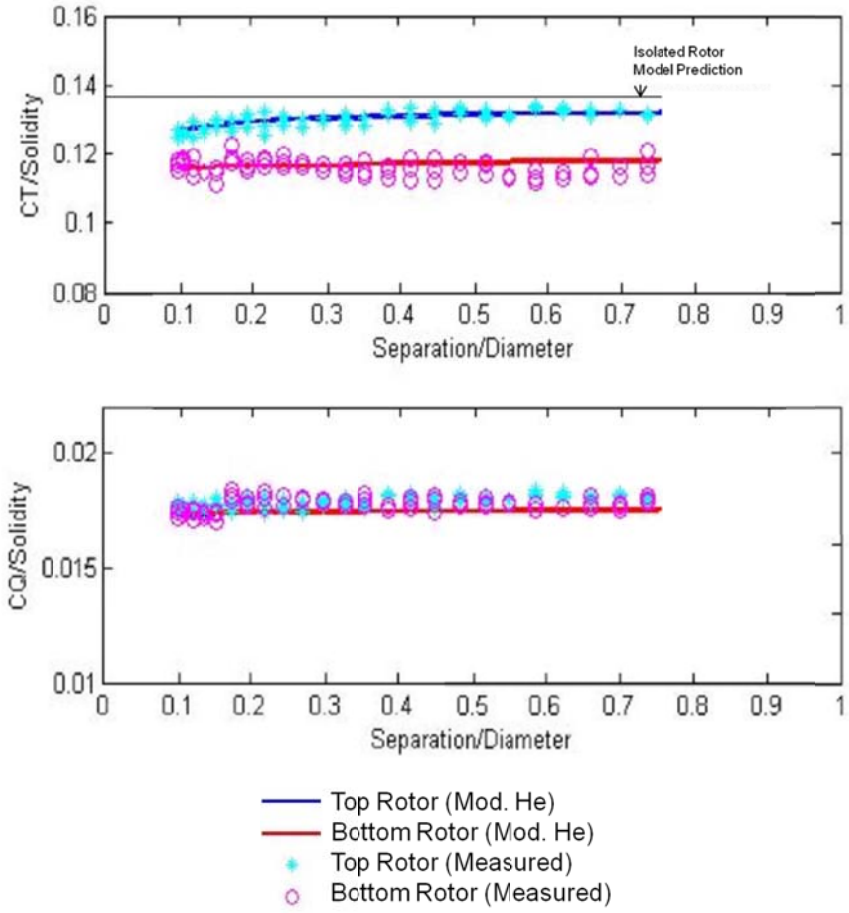

Figure 4-48 Comparisons of thrust and torque predictions using the extended Peters-He inflow model with test data

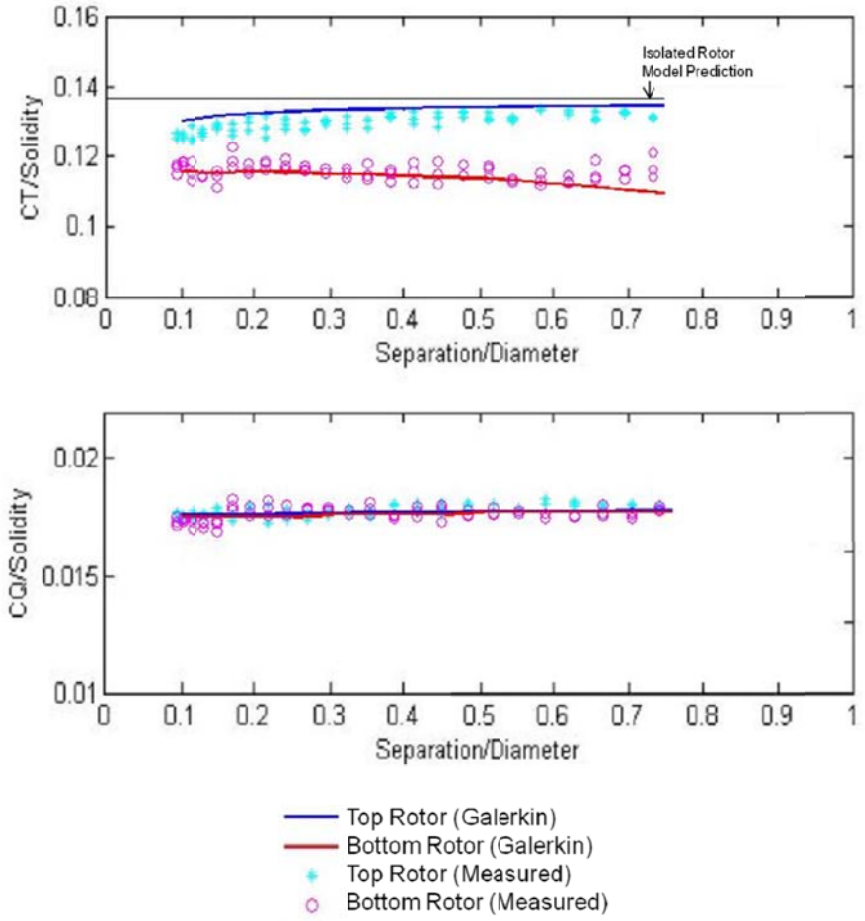

Figure 4-49 Comparisons of thrust and torque predictions using Galerkin method based inflow model with test data

Chapter 5 More Accurate Model

5.1 Optimization for Even Terms

As discussed in former chapters, the convergence of the co-state method can be optimized by use of fewer even terms than odd terms, with the optimum ratio a function of skew angle within the wake below the rotor disk. The convergence of the results will be determined by comparing the results from convolution with the results obtained by the co-state method. The error norm is defined as

$$(E)^2 = \frac{\int_{r_0}^{r_f} (v_1 - v_2)^2 \, dr}{\int_{r_0}^{r_f} v_1^2 dr} \tag{5.1}$$

where v_1 is the inflow distribution from convolution method and v_2 is the result from the co-state method. Here, two kinds of error norms are defined, one is for the on disk region only ($r_0 = -1; r_f = 1$), and the other one for on/off disk region ($r_0 = -2$; $r_f = 2$) at an azimuth angle $\bar{\psi}$.

In order to determine the number of even terms included in the solution, we will use the table method in Ref [14]. There are four different ways to specify the even terms: 1) by indicating the number of harmonics, m; 2) by indicating the number for the highest power of r; 3) by indicating the number of terms for the zeroth harmonics; or 4) by indicating the index of the highest subscript, *n* of the Φ_n^m term. The relationships of different expressions are as follow:

$$highest \quad power \quad of \quad r = m \tag{5.2}$$

$$terms @ zeroth \quad harmonics = Int\left(\frac{highest \quad power \quad of \quad r}{2}\right) + 1 \tag{5.3}$$

$$Index \quad of \quad highest \quad subscripts = \begin{Bmatrix} m+1; odd \quad terms \\ m; even \quad terms \end{Bmatrix} \tag{5.4}$$

where $Int(x)$ is a function that rounds the elements of x the nearest integer towards zero.

5.2 New Formulation for $\bar{Q}_n^m(i\eta)$

Another important aspect of obtaining a converged result is a robust way to compute $\bar{Q}_n^m(i\eta)$. From Appendix 2, we know that, the associate Legendre function of the second kind satisfy the following equation

$$\frac{d}{d\eta}\left[\left(1+\eta^2\right)\frac{d\bar{Q}_n^m}{d\eta}\right]+\left[\frac{m^2}{1+\eta^2}-n(n+1)\right]\bar{Q}_n^m=0 \tag{5.5}$$

Then for large η, we just assume that $\bar{Q}_n^m(i\eta)$ could be written in series as follows

$$\bar{Q}_n^m=\frac{A_0}{\eta^q}+\frac{A_2}{\eta^{q+2}}+\frac{A_4}{\eta^{q+4}}+\ldots+\frac{A_{2p}}{\eta^{q+2p}} \tag{5.6}$$

Then based on the form of $\bar{Q}_n^m(i\eta)$, we have

$$\frac{d\bar{Q}_n^m}{d\eta}=-r\frac{A_0}{\eta^{q+1}}-(r+2)\frac{A_2}{\eta^{q+3}}-(r+4)\frac{A_4}{\eta^{q+5}}-\ldots-(r+2p)\frac{A_{2p}}{\eta^{q+2p+1}} \tag{5.7}$$

And we have the second derivative of $\bar{Q}_n^m(i\eta)$ could be represented by

$$\begin{aligned}\frac{d^2\bar{Q}_n^m}{d\eta^2}=&q(q+1)\frac{A_0}{\eta^{r+2}}+(q+2)(q+3)\frac{A_2}{\eta^{q+4}}+(q+4)(q+5)\frac{A_4}{\eta^{q+6}}+\ldots\\&+(q+2p)(q+2p+1)\frac{A_{2p}}{\eta^{q+2p+2}}\end{aligned} \tag{5.8}$$

We also know

$$\frac{1}{1+\eta^2}=\frac{1}{\eta^2}\left(\frac{1}{1+\frac{1}{\eta^2}}\right)=\frac{1}{\eta^2}\left(1-\frac{1}{\eta^2}+\frac{1}{\eta^4}-\frac{1}{\eta^6}+\ldots\right)=\frac{1}{\eta^2}-\frac{1}{\eta^4}+\frac{1}{\eta^6}-\frac{1}{\eta^8}+\ldots \tag{5.9}$$

Then substitute (5.6), (5.7), (5.8), (5.9) into (5.5), suppose $\Upsilon=\frac{1}{\eta}$, then we have

$$
\begin{aligned}
&q(q+1)A_0\Upsilon^{q+2}+(q+2)(q+3)A_2\Upsilon^{q+4}+(q+4)(q+5)A_4\Upsilon^{q+6}+\ldots\\
&q(q+1)A_0\Upsilon^{q}+(q+2)(q+3)A_2\Upsilon^{q+2}+(q+4)(q+5)A_4\Upsilon^{q+4}+\ldots\\
&-2qA_0\Upsilon^{q}-2(q+2)A_2\Upsilon^{q+2}-2(q+4)A_4\Upsilon^{q+4}-\ldots\\
&+\left[m^2\left(\Upsilon^2-\Upsilon^4+\Upsilon^6+\ldots\right)-n(n+1)\right]\left(A_0\Upsilon^{q}+A_2\Upsilon^{q+2}+A_4\Upsilon^{q+4}+\ldots\right)\\
&=0
\end{aligned}
\tag{5.10}
$$

As Υ is positive for any η (η is positive), then the coefficient for Υ^q should be zero in order to satisfy (5.10), which means

The coefficient of Υ^q:

$$q(q+1)A_0\Upsilon^{q}-2qA_0\Upsilon^{q}-n(n+1)A_0\Upsilon^{q}=0 \tag{5.11}$$

which requires $q(q-1)=n(n+1)$, as n could be any integer that bigger than zero, which means $q=n+1$.

The coefficient of Υ^{q+2}:

$$
\begin{aligned}
&q(q+1)A_0\Upsilon^{q+2}+(q+2)(q+3)A_2\Upsilon^{q+2}-2(q+2)A_2\Upsilon^{q+2}+m^2A_0\Upsilon^{q+2}\\
&\quad-n(n+1)A_2\Upsilon^{q+2}=0
\end{aligned}
\tag{5.12}
$$

which is

$$A_2=\frac{q(q+1)+m^2}{n(n+1)+2(q+2)-(q+2)(q+3)}A_0 \tag{5.13}$$

Substitute $q=n+1$, then we have

$$A_2=\frac{(n+1)(n+2)+m^2}{n(n+1)+2(n+3)-(n+3)(n+4)}A_0=-\frac{(n+1)(n+2)+m^2}{2(2n+3)}A_0 \tag{5.14}$$

Then by the same procedure, we know that the coefficient of Υ^{q+4}:

$$
\begin{aligned}
&(q+2)(q+3)A_2\Upsilon^{q+4}+(q+4)(q+5)A_4\Upsilon^{q+4}-2(q+4)A_4\Upsilon^{q+4}\\
&+m^2A_2\Upsilon^{q+4}-m^2A_0\Upsilon^{q+4}-n(n+1)A_4\Upsilon^{q+4}=0
\end{aligned}
\tag{5.15}
$$

Express A_4 with A_0, we have

$$A_4=\left[\frac{m^2}{4(2n+5)}+\frac{\left[m^2+(n+3)(n+4)\right]\left[m^2+(n+1)(n+2)\right]}{8(2n+3)(2n+5)}\right]A_0 \tag{5.16}$$

Follow the same steps, we can derive more coefficients, with which the calculation for $\bar{Q}_n^m$ could be more accurate.

5.3 Results with Optimized Model

The model we use here is truncated with 20 harmonics. The errors for z component are given in the figures. These results are all obtained at $\xi = 1$.

Figure 5-1 and Figure 5-2 show the error norm in the axial flow component of induced velocity in axial flow at $\omega = 4$ for a pressure distribution Φ_1^0. From Figure 5-1, we can tell that by adding two even terms, the error norm is reduced dramatically, from its original value of 26.0% down to 10.0%. The error will keep reducing with the even term increasing, which means the more even terms in this case, the smaller the error norm will be. The minimum error will be obtained while we include 9 even terms. For the on/off disk error, which is $-2 \le x_0 \le 2$, we can observe almost the same phenomena that the error goes from a very big number (42.9%) with no even terms straightly down to 0.3% when even terms with 9 at the index is included.

Figure 5-2 is the error norm for the first cyclic pressure distribution Φ_2^1 at frequency $\omega = 4$, which shows a similar result for Φ_1^0. In this case, only 2 even terms are enough to reduce the on-disk error to about 1%. The on/off disk error goes from 30% to 0.3% when 10 even terms are included for m=0 harmonics.

The analysis for axial flow cases reveals that choosing proper number of even terms may dramatically decrease the error norm for different pressure distributions. It will be helpful to analyze the behavior of the convergence for steeper skew angels to find what numbers should be chosen for different cases. In order to find a proper pattern description for even terms, we will do the same analysis for skew angle $\chi = 30^o$ and $\chi = 75^o$.

Figure 5-3 shows the on disk and on/off disk errors when the input is Φ_1^0 at a frequency $\omega = 4$. In this case, maximum error is 22.7%, also with no even terms and the minimum error is 0.6% with 9 even terms involved in the solution. In this case, the maximum error and minimum error are both smaller than what show in axial flow. It is indicated that error introduced by the Peters-He model decreases as the skew angle increases. The on/off disk error has a similar behavior. The almost same phenomena for cyclic pressure distribution under small skew angles is shown in Figure 5-4. The difference is that the minimum error is with 11 even terms, which odd terms equal to the even terms.

Figure 5-5 and Figure 5-6 are error norms for elliptical pressure distribution and cyclic distribution with deep skew angles, $\chi = 75^o$. In both figures, we can tell that the model converges slowly. In Figure 5-5, without even terms, the error is 14.0%, meanwhile the error is 32.0% with 2 even terms. The error with a small number of even terms included in the solution is lower than the one obtained with a large number of even terms. However, with adding more even terms, the error is tending to get smaller. With 9 even terms, the error is 14.5%, though not the minimum point, it is only slightly bigger than the result without even terms. For on/off disk error, it is obvious that more even terms make the error smaller till the number reaches 8. In Figure 5-6, the minimum on disk error will be 7.4% with 10 even terms compared to a small bigger error 8.2% without even terms. For the on/off disk error, it goes from 55% without even terms monotonically down to 21.1% with 10 even terms.

From the above figures, we can tell that the for different skew angles, the model may require different even terms to minimize the errors, and with small skew angels, more even terms are needed, and for big skew angels, less even terms should be included. However, for big skew angles, there is still a comparable small error norm with even terms. For real simulation system, the helicopter may change fly status quite often and it will be much more convenient and practical if we can choose a fix number for even terms instead of choosing it as a variable of skew angles while we can still have a relative small error. By comparing, we found that limit the number of

even terms to 9 for m=0 harmonics works well for almost all cases without losing too much accuracy. And the on/off disk error also benefits from this chosen based on the error curve shown in the figures.

We would also show the results from the optimized co-state method and the co-state method with odd terms equivalent to even terms compared with convolution result. Figure 5-7 compares the frequency responses for the first elliptical pressure distribution. In this figure, we can tell that the optimized method not only did well at on rotor disk region, but also at off disk region. The isolation around $x_0 = -1.5$ is because of the error in computation of $\bar{Q}_n^m(i\eta)$ for large η, which is also mentioned in Ref. [17]. Figure 5-8 compares the frequency responses of the first cyclic pressure distribution.

In order to minimize these errors and make the calculation for $\bar{Q}_n^m(i\eta)$ more accurate and robust, we develop a new scheme for calculating $\bar{Q}_n^m(i\eta)$. In Figure 5-9, it is displayed of a comparison $\bar{Q}_{20}^0(i\eta)$ (since it is the worst case for 20 harmonics) by different methods. $\bar{Q}_{20}^0(i\eta)$ will blow up around $\eta = 1.08$ with the iterative method in Ref. [17]. Here, we will switch to our new method at $\eta = 1$ and maintain the part with $\eta < 1$ from the recursive method. We can see from the figure, after the switch at $\eta = 1$, our method still converges well.

Based on the new scheme for $\bar{Q}_n^m(i\eta)$, we can go deeper within the flow field without blowing up and losing accuracy. Figure 5-10 shows the result of comparison with different schemes for $\bar{Q}_n^m(i\eta)$ with the optimized co-state method for elliptical pressure distribution. It could be seen that for $x_0 < 0$, the result with old scheme diverges, however, the result with the new scheme for $\bar{Q}_n^m(i\eta)$ keeps the inflow distribution follow the convolution result. Figure 5-11 is the comparison of the optimized scheme with different formula for $\bar{Q}_n^m(i\eta)$ for cyclic pressure distribution. Even though the osculation is not as strong as what displays in Figure 5-10 with the

old recursive method to calculate $\bar{Q}_n^m(i\eta)$, with the new formula for $\bar{Q}_n^m(i\eta)$, the result behaves much better.

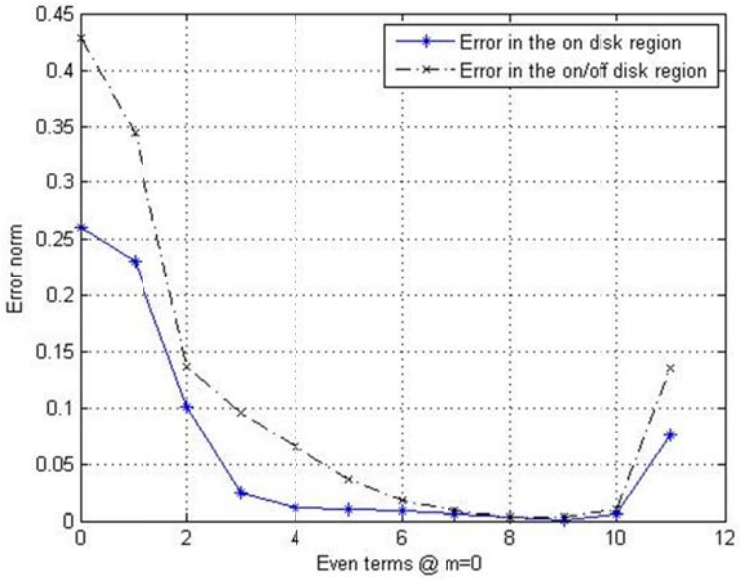

Figure 5-1 Error norm for Φ_1^0 with $\omega = 4$, $\chi = 0^o$

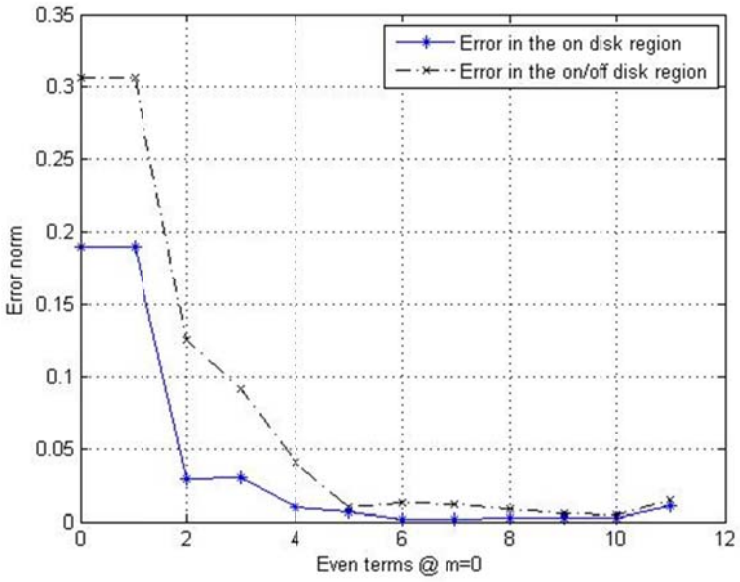

Figure 5-2 Error norm for Φ_2^1 with $\omega = 4$, $\chi = 0^o$

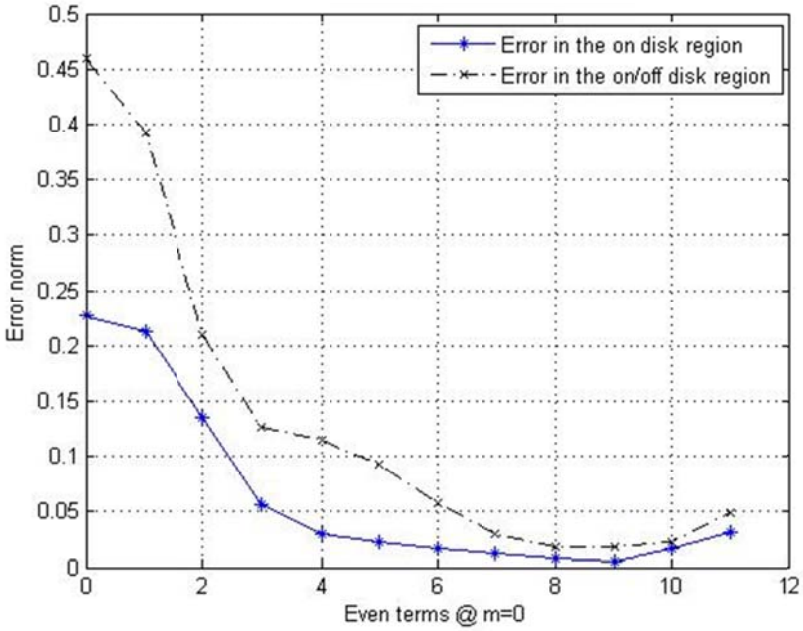

Figure 5-3 Error norm for Φ_1^0 with $\omega = 4$, $\chi = 30^o$

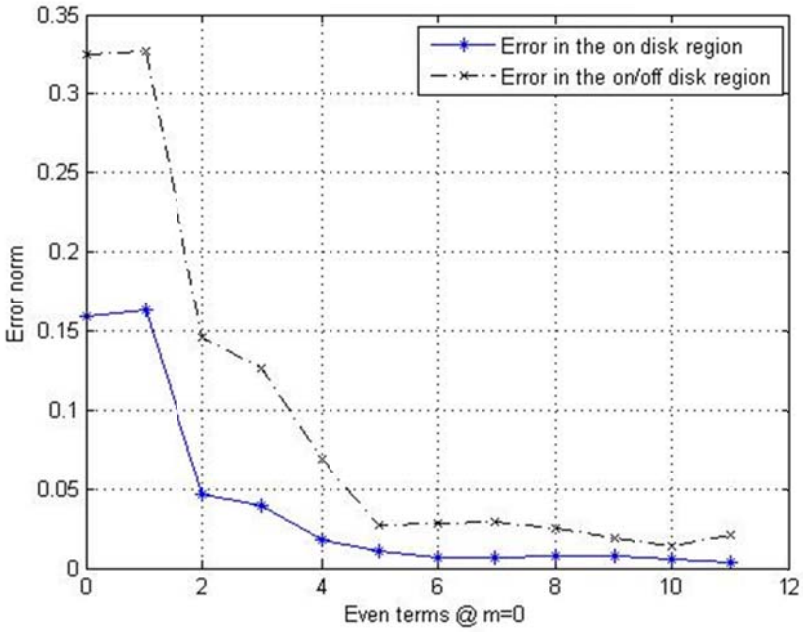

Figure 5-4 Error norm for Φ_2^1 with $\omega = 4$, $\chi = 30^o$

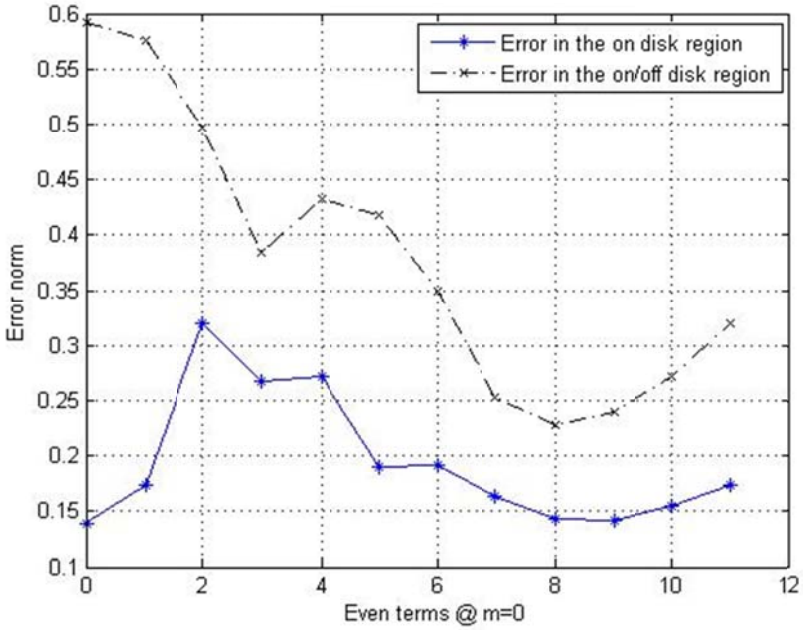

Figure 5-5 Error norm for Φ_1^0 with $\omega = 4$, $\chi = 75^o$

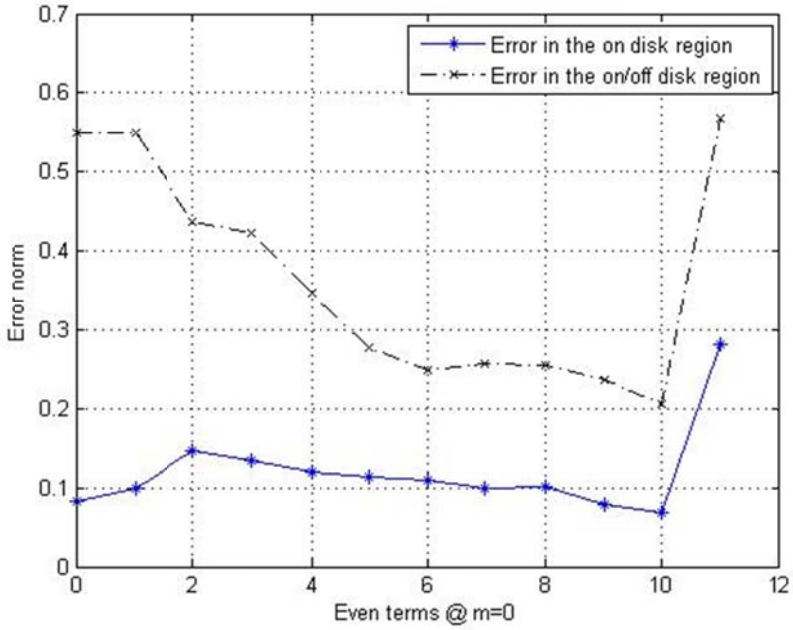

Figure 5-6 Error norm for Φ_2^1 with $\omega = 4$, $\chi = 75^o$

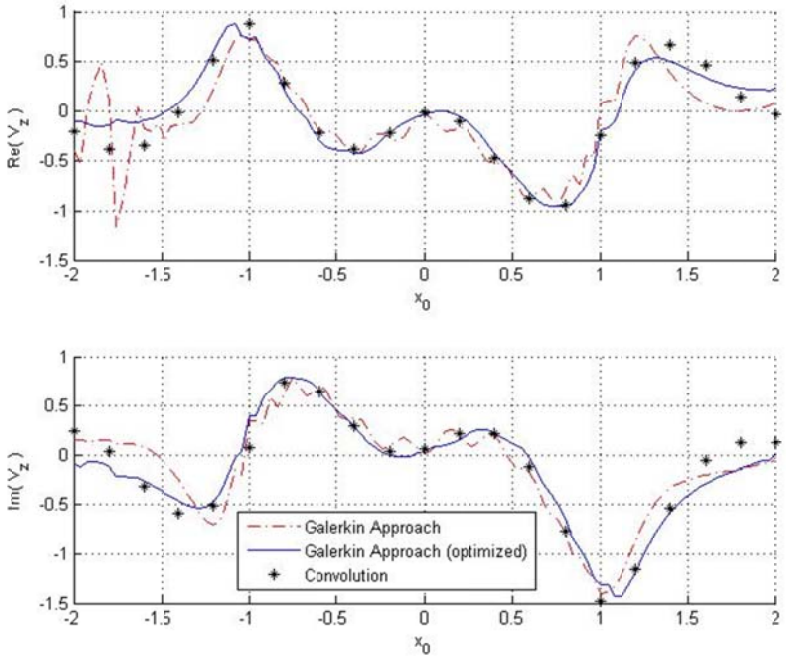

Figure 5-7 Frequency responses for Φ_1^0 with $\omega = 4$, $\chi = 75^o$, $\xi = 1$

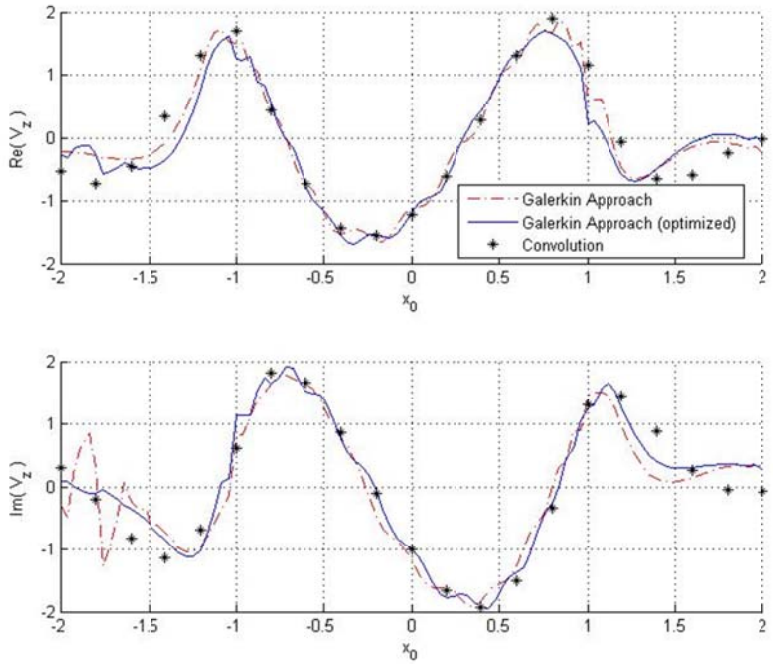

Figure 5-8 Frequency responses for Φ_2^1 with $\omega = 4$, $\chi = 75^o$, $\xi = 1$

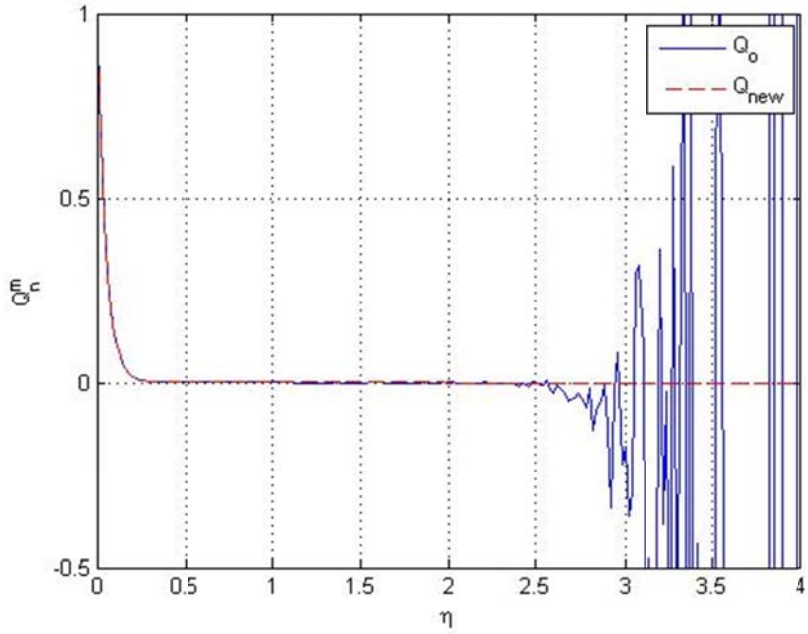

Figure 5-9 Comparison of $\bar{Q}_{20}^{0}(i\eta)$ by different method

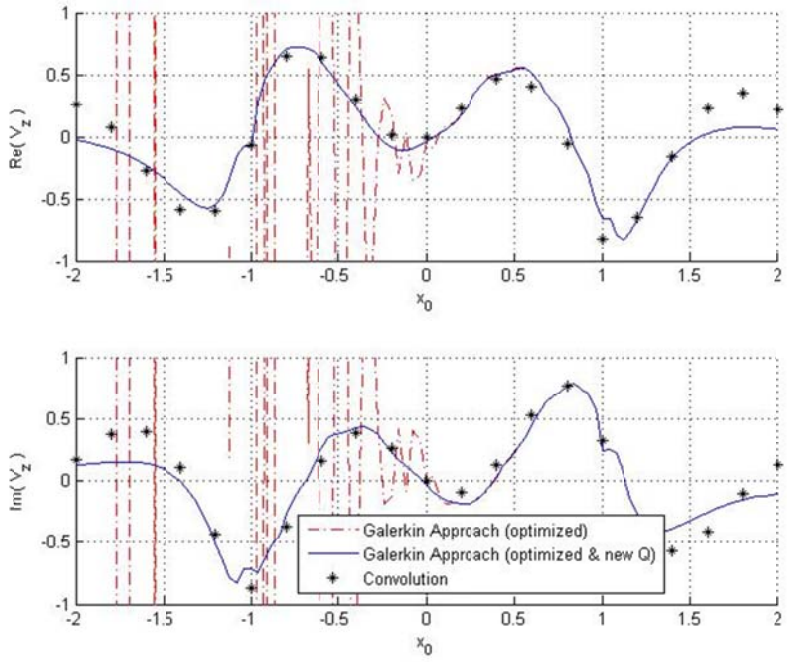

Figure 5-10 Frequency responses for Φ_1^0 with $\omega = 4$, $\chi = 75^{\circ}$, $\xi = 2$

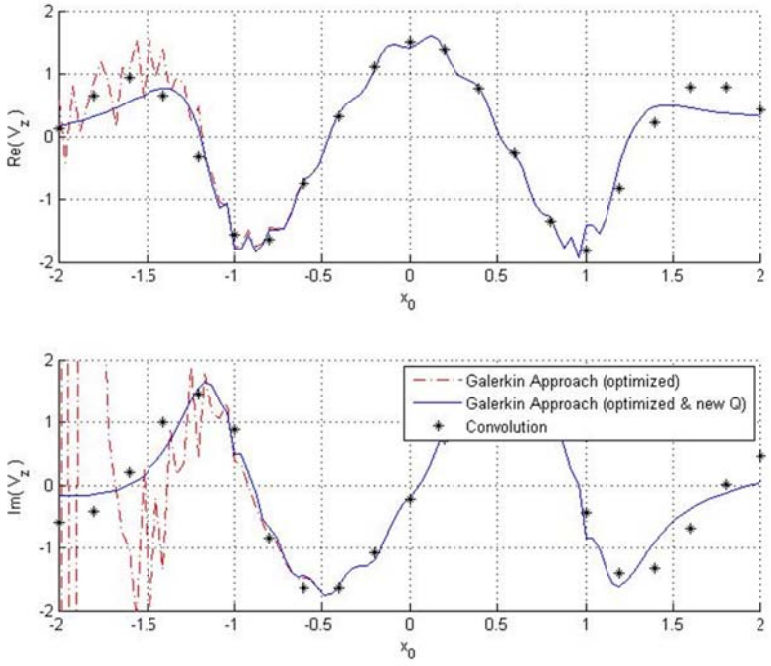

Figure 5-11 Frequency responses for Φ_2^1 with $\omega = 4$, $\chi = 75^o$, $\xi = 2$

Chapter 6 Finite Blade Responses

In this chapter, we apply the model to more practical examples in which pressure spikes from a finite number of blades are rotating around the azimuth at constant speed.

6.1 Finite Blade Systems

The fundamental fluid mechanics of the model is based on the potential-flow functions, and the detail of the theoretical derivation of this unsteady dynamic model is derived in Chapter 2 and Ref [6].

In general, the induced velocity at the disk in terms of harmonics will be

$$\vec{v}\left(r,\psi,\xi,\tau\right)=\sum_{m=0}^{\infty}\sum_{n=m}^{\infty}\begin{bmatrix}a_n^m\left(\tau\right)\vec{\nabla}\left(\sigma_n^m\Phi_{n+1}^{mc}+\varsigma_n^m\Phi_{n-1}^{mc}\right)\\+b_n^m\left(\tau\right)\vec{\nabla}\left(\sigma_n^m\Phi_{n+1}^{ms}+\varsigma_n^m\Phi_{n-1}^{ms}\right)\end{bmatrix} \tag{6.1}$$

and the coefficients a_n^m and b_n^m could be derived from the following governing differential equations

$$\begin{aligned}\left[M^c\right]\left\{\overset{*}{a}_n^m\right\}+\left[D^c\right]\left[L^c\right]^{-1}\left[M^c\right]\left\{a_n^m\right\}&=\left[D^c\right]\left\{\tau_n^{mc}\right\}\\\left[M^s\right]\left\{\overset{*}{b}_n^m\right\}+\left[D^s\right]\left[L^s\right]^{-1}\left[M^s\right]\left\{b_n^m\right\}&=\left[D^s\right]\left\{\tau_n^{ms}\right\}\end{aligned} \tag{6.2}$$

where

$$\tau_n^{0c}=\frac{1}{2\pi}\sum_{q=1}^{Q}\int_0^1 L_q\left(r,\tau\right)\phi_n^0\left(\nu\right)dr \tag{6.3}$$

$$\tau_n^{mc}=\frac{1}{\pi}\sum_{q=1}^{Q}\int_0^1 L_q\left(r,\tau\right)\phi_n^m\left(\nu\right)dr\cos\left(m\psi_q\right) \tag{6.4}$$

$$\tau_n^{ms}=\frac{1}{\pi}\sum_{q=1}^{Q}\int_0^1 L_q\left(r,\tau\right)\phi_n^m\left(\nu\right)dr\sin\left(m\psi_q\right) \tag{6.5}$$

with $\phi_n^m\left(\nu\right)$ the radial expansion functions $\bar{P}_n^m\left(\nu\right)/\nu$, where $r=\sqrt{1-\nu^2}$.

In order to predict the inflow below rotor disk for finite blade systems, it is

advantageous to rewrite the inflow model in the rotating systems. In order to do that, a reference blade needs to be selected first, and then the azimuthal position of any blade ψ_q could be represented according to the reference blade

$$\psi_q = \Omega t + \hat{\psi}_q = \bar{t} + \hat{\psi}_q \tag{6.6}$$

where τ is the position of the reference blade in the nonrotating system and

$$\hat{\psi}_q = \frac{2\pi}{Q}(q-1) \tag{6.7}$$

Thus, for a case with constant blade loading, it is convenient to write the unsteady $\tau_n^m(\bar{t})$ in terms of constant unsteady $\hat{\tau}_n^m$ s.

$$\begin{aligned}
\tau_n^{0c} &= \hat{\tau}_n^{0c} = \frac{1}{2\pi}\sum_{q=1}^{Q}\int_0^1 L_q(r,\tau)\phi_n^0(\nu)\,dr \\
\tau_n^{mc} &= \hat{\tau}_n^{mc}\cos(m\bar{t}) - \hat{\tau}_n^{ms}\sin(m\bar{t}) \\
\tau_n^{ms} &= \tau_n^{mc}\sin(m\bar{t}) + \hat{\tau}_n^{ms}\cos(m\bar{t})
\end{aligned} \tag{6.8}$$

where

$$\hat{\tau}_n^{mc} = \frac{1}{\pi}\sum_{q=1}^{Q}\int_0^1 L_q(r,\tau)\phi_n^m(\nu)\,dr\cos(m\hat{\psi}_q)$$

$$\hat{\tau}_n^{ms} = \frac{1}{\pi}\sum_{q=1}^{Q}\int_0^1 L_q(r,\tau)\phi_n^m(\nu)\,dr\sin(m\hat{\psi}_q)$$

Note further that Eq. (6.2) is in reduced time τ, therefore, one needs to write

$$\begin{aligned}
\cos(m\bar{t}) &= \cos\left[\frac{m\tau}{V_\infty/(\Omega R)}\right] \\
\sin(m\bar{t}) &= \sin\left[\frac{m\tau}{V_\infty/(\Omega R)}\right]
\end{aligned} \tag{6.9}$$

6.2 Relationship between Different Systems

For typical helicopter applications, the angle of the vortex sheets leaving the blade is small such that $\cos(\phi)=1$. However, in cases for which there is significant inflow, Figure 6-1 and Figure 6-2 show how the induced flow of the actuator-disk model correlates to the flow on the actual vortex-system of the rotor. On the actual rotor, the lift is perpendicular to the sheet creating a combination of axial and swirl velocity

that gives an induced velocity along the same direction as the lift, as shown in Figure 6-1. This tilted lift is applied perpendicular to the actuator disk as shown in Figure 6-2. The average induced flow perpendicular to the disk is w which corresponds to the tilted inflow vector of the true rotor system.

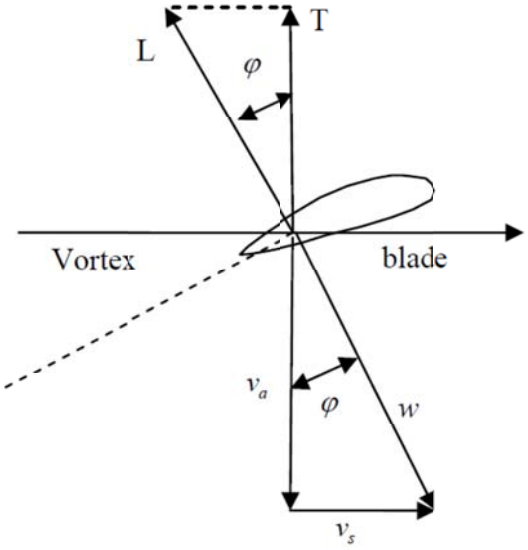

Figure 6-1 Inflow velocity components for physical rotor

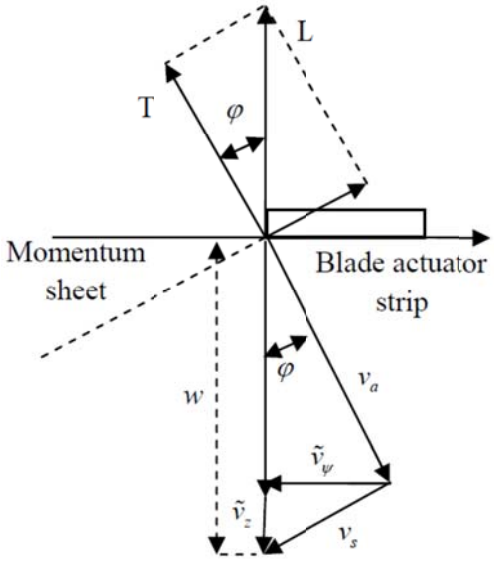

Figure 6-2 Inflow velocity components for actuator disk construct

Interestingly, although the actuator disk can create no net angular momentum (and thus no net swirl velocity), results show that there is positive angular momentum between the momentum sheets and then negative angular momentum within the sheets—which appears as an impulse in velocity along the sheet. If that velocity is subtracted from w, the resultant flow has a component of angular velocity normal to the sheet that is identical to the Glauert prediction of what the angular velocity must be, as shown in Figure 6-1. Thus, the results from the actuator disk theory can be used directly on the true rotor by tilting the velocity vector between the momentum sheets by the appropriate angle, ϕ, as postulated in Ref. [18]. The result is a rigorously exact solution for both axial velocity and swirl velocity.

6.3 Results for Axial Flow with Finite Blades

The results will be presented with 2 blades and $r = 0.8$ with axial flow only. The three components of velocities for both the inflow above and below the rotor disk are given in the figures. The model is truncated at 24 harmonics. There is an optimum combination of even and odd harmonics for maximum accuracy, as illustrated in Chapter 4. Here, we use the case of only odd terms and no even terms and do not pursue an optimum solution.

Figure 6-3 to Figure 6-5 show the three velocity components of inflow versus time on the rotor disk at point $r = 0.8$, $\psi = 0^o$ in space, where the detection point actually locates. The time $\bar{t} = 0$ represents the time at which the blades are parallel with x-axial, which is also $y = 0$ axial. Figure 6-3 to Figure 6-5 show z component, ψ component, and r component respectively. In Figure 6-3, there is a doublet spike around $\bar{t} = \frac{\pi}{2}$ (or $\bar{t} = \frac{3\pi}{2}$), which is due to the rotor blade passage. The impulses in Figure 6-4 and Figure 6-5 are also caused by passing of blades.

Figure 6-6 to Figure 6-8 show the inflow within the wake at one radus below the rotor disk at the point $r = 0.8$, $\psi = 0^o$. We can see v_z, v_ψ and v_r all have impulses at the vortex-sheet passage followed by oscillations between the passages. The average velocity for v_z is 0.3067, which is almost 1.73 times of the average velocity at the rotor disk ($v_z = 0.1772$). [This is not far enough downstream to reach the familiar factor of 2 increase in velocity.] We can see spikes in Figure 6-5 and Figure 6-6, and the peaks of the spikes locate near $\bar{t} = 1$ since the phase shift for the spike should be the same as the depth within the wake region.

Figure 6-9 to Figure 6-11 are about the inflow two radii below the rotor disk at $r = 0.8$, $\psi = 0^o$. The average velocity of z component is 0.3390, which is 1.91 times

of the average velocity at the rotor disk. This is very close to the well know result from momentum theory and could be treated as fully developed. We notice that v_r is decreasing along the streamline, from -0.1853 ($z=0$), -0.0277 ($z=1$) to -0.0075 ($z=2$). This variation could be used to describe the fact that the wake region is contracting.

In order to analysis the effect of blades, we now introduce $\tilde{v}_z$ and $\tilde{v}_\psi$, which are the velocities between blade passages in the z direction and ψ direction, respectively. Suppose w is the velocity downstream. We can predict what $\tilde{v}_z$ and $\tilde{v}_\psi$ should be (based on translational and angular momentum theory) since the total velocity must be perpendicular to the vortex sheet. By the comparing of a real physical rotor system (shown in Figure 6-1) and actuator disk construct (shown in Figure 6-2), we can relate the velocities in these two figures, yielding the expressions $\tilde{v}_\psi = w*\sin(\varphi)*\cos(\varphi)$ and $\tilde{v}_z = w*\sin^2(\varphi)$. For the case $r=0.8$, $\tan(\varphi) = wR/r = 0.1/0.8$, which means $\varphi = 7.1°$. So that we can calculated $\tilde{v}_z = 0.006$ and $\tilde{v}_\psi = 0.044$. Here from numerical integrations, we have $\tilde{v}_z = 0.0093$ and $\tilde{v}_\psi = 0.0564$. Even though the result we have here for w is not the final converged value, we can still tell the evaluate values for $\tilde{v}_z$ and $\tilde{v}_\psi$ are close enough. This further means we can use the result in actuator disk theory to predict the angular momentum in real systems.

Figure 6-12 shows the changing of $\tilde{v}_\psi$ along the free streamline with 0.8 radius away from the center. We can tell from the figure that at one radius above the disk ($z=-1$), $\tilde{v}_\psi$ is almost 0; on the disk, the value is 0.0284 compared with 0.0564 far away from the rotor disk ($z=2$). These numerical results are consistent with the Glauert prediction that full angular momentum just below the disk is twice the angular momentum at the disk. The angular velocity increases as the flow approaches the disk and passes through it. The figure shows close agreement with

the Glauert prediction of “no angular momentum above the disk, and full momentum just below the disk that does not change through the wake”.

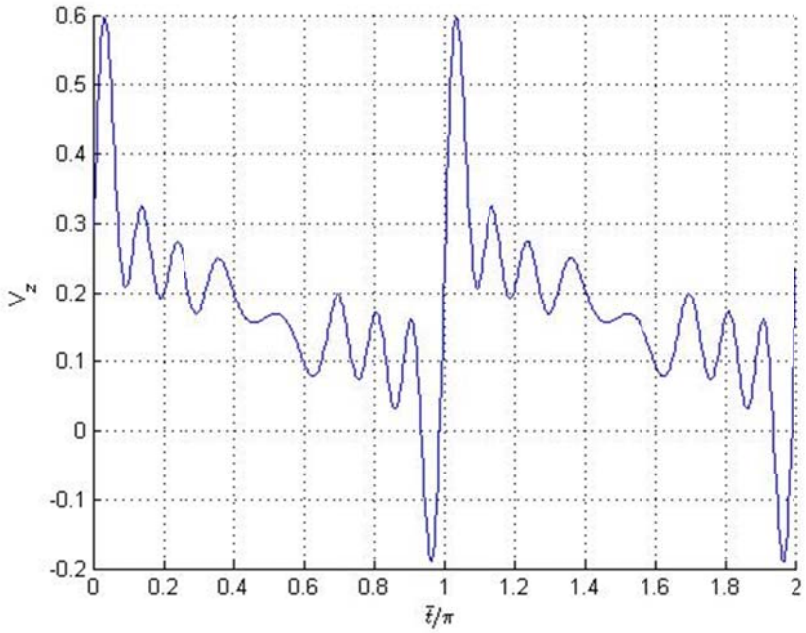

Figure 6-3 V_z for $\xi = 0$ at $r = 0.8$ and $\psi = 0^o$

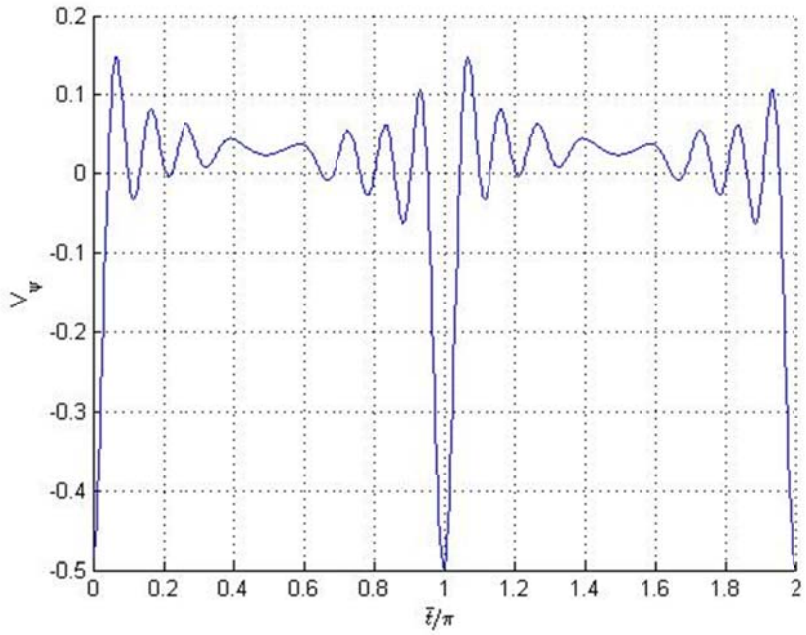

Figure 6-4 V_ψ for $\xi = 0$ at $r = 0.8$ and $\psi = 0^o$

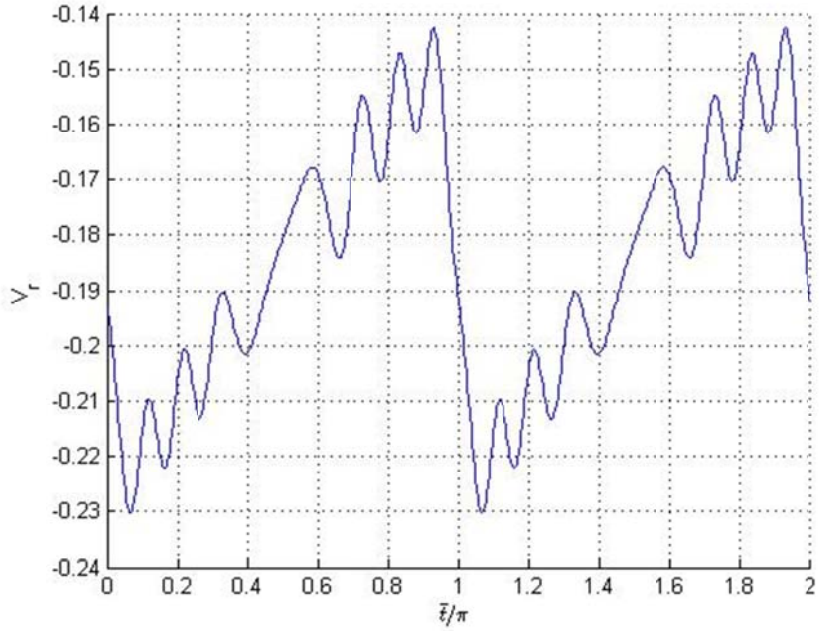

Figure 6-5 V_r for $\xi = 0$ at $r = 0.8$ and $\psi = 0^o$

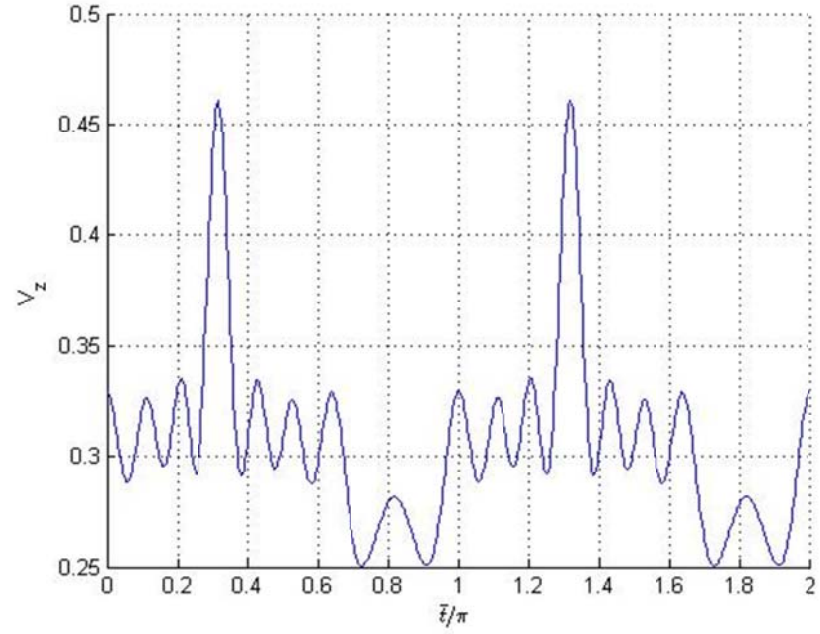

Figure 6-6 V_z for $\xi = 1$ at $r = 0.8$ and $\psi = 0^o$

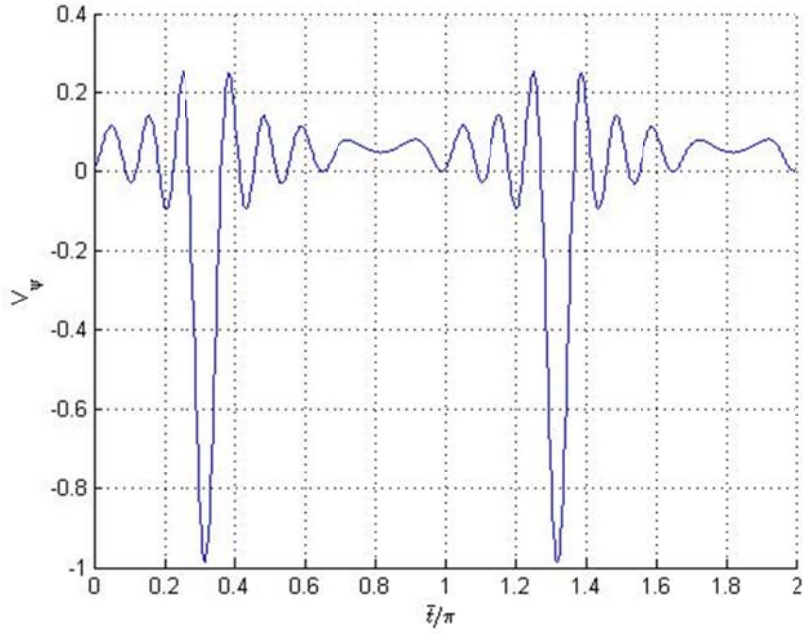

Figure 6-7 V_ψ for $\xi = 1$ at $r = 0.8$ and $\psi = 0^o$

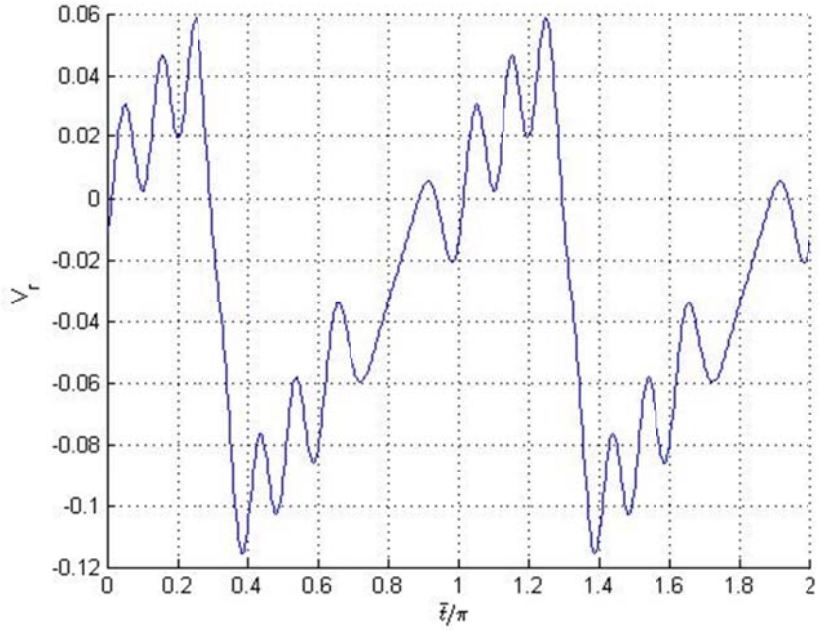

Figure 6-8 V_r for $\xi = 1$ at $r = 0.8$ and $\psi = 0^o$

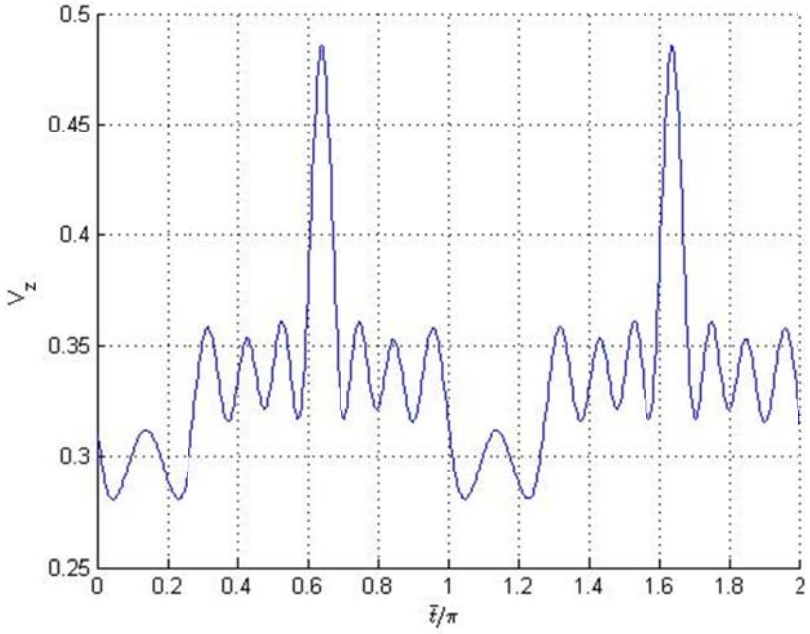

Figure 6-9 V_z for $\xi = 2$ at $r = 0.8$ and $\psi = 0^o$

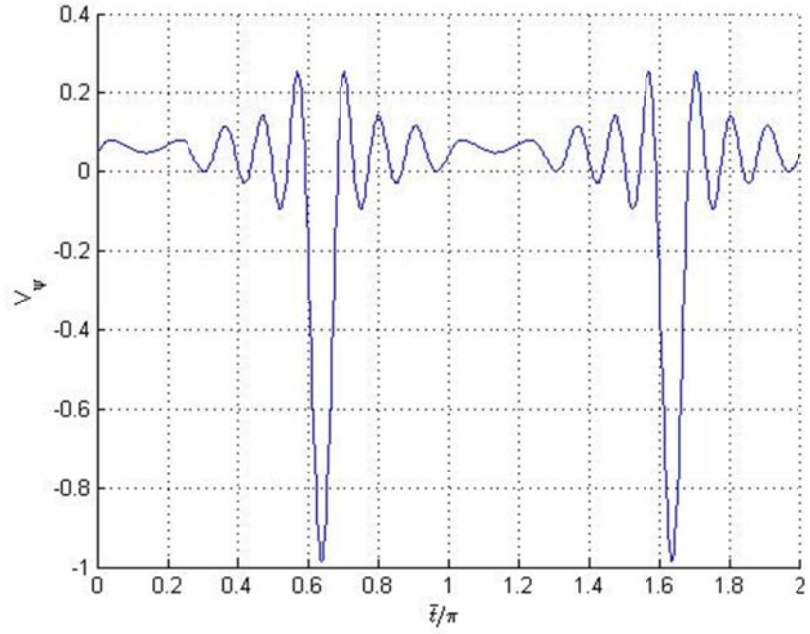

Figure 6-10 V_ψ for $\xi = 2$ at $r = 0.8$ and $\psi = 0^o$

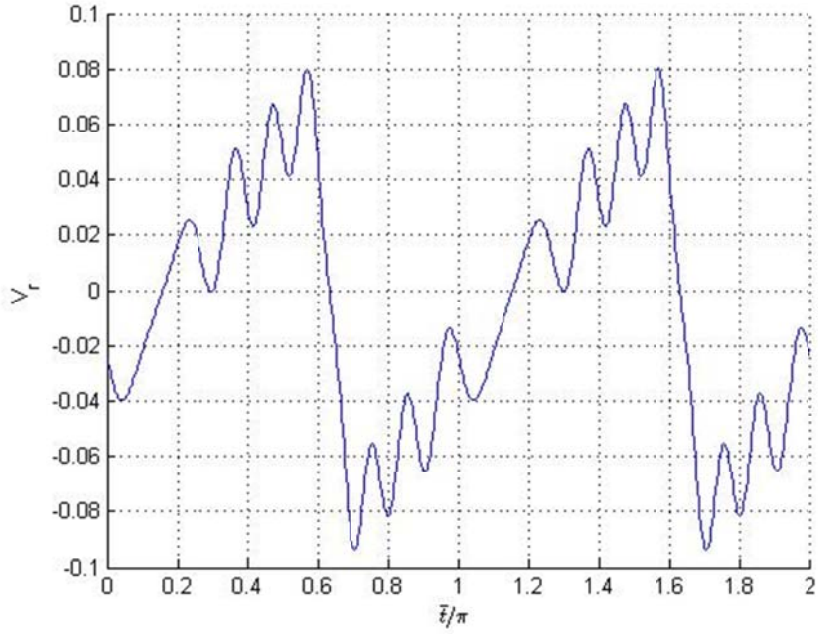

Figure 6-11 V_r for $\xi = 2$ at $r = 0.8$ and $\psi = 0^o$

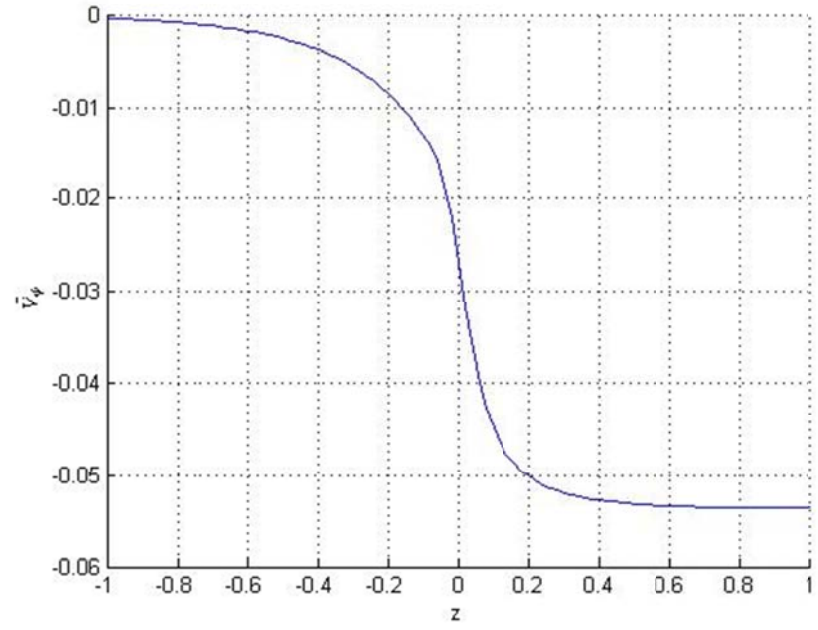

Figure 6-12 $\tilde{V}_\psi$ versus z with $r = 0.8$ and $\psi = 0^o$

Chapter 7 Summary, Conclusions and Future Work

In the first part of this work, the eigenvalues and mode shapes of finite-state inflow models have been studied by eigen-analysis. The visualizing of mode shapes provides us a better understanding of the rotor wake mechanism. The eigen-analysis also shows the inflow harmonics are highly coupled at larger wake skew angles. The structure of the mode shapes outside the rotor disk enables Hsieh/Duffy inflow model to describe the velocity distribution outside the disk. The eigenvalues of Peters-He model change slightly and converge quickly with the number of expansion terms, and an easy way to estimate these eigenvalues is also established. A formula for estimating the eigenvalues in axial flow is shown by regressive method. Though Hsieh/Duffy model converges much more quickly than Peters-He model, it exacts this added accuracy at the cost of twice as many states and with a system that is not as well-conditioned as the He model.

In the second part of this work, finite-state inflow models have now been extended such that the flow can be computed anywhere in the flow field for any wake skew angle. The methodology is developed in a mathematically rigorous way from the potential flow equations. Comparison with convolution results (axial flow and skewed angle flow) demonstrates exact correspondence with closed-form solutions for both time responses and frequency responses. The cost of the operation is the cost of computing the co-states for the adjoint velocity.

After extending the model from above the rotor disk to below the rotor disk, to make the model converge as quickly and accurately as possible within wake region becomes another problem that needs to be solved. An extensive convergence analysis is performed with the new model below the rotor disk with 20 harmonics, and it is concluded that there would be a different combination for odd and even terms with different skew angles to optimize the on-disk and the on/off disk velocity profile. In order to satisfy the requirements of real simulation systems, we find that to keep 9

even terms at m=0 harmonics works nearly for all skew angles and at both on disk and on/off disk region. If the optimum values for even terms are included in the solution with 20 harmonics odd terms, it is observed that the co-state method is virtually exact for axial flow and introduces a smaller than 15.0% error for big skew angle ($\chi = 75^{o}$) with on disk error. At the same time, a new scheme for Legendre function of the second kind $\bar{Q}_n^m(i\eta)$ is derived to solve the divergence with large η. With the optimized model and well converged Legendre function, a more robust result with quick convergence rate is displayed compared with the convolution result.

Finally, the co-state model is applied to finite blade systems to study the inflow within the wake region. A relationship between real systems and actuator disk systems is established for further study. The spikes are appeared in the normal and azimuth velocity responses for the rotating system, which are due to the rotor blade passage. These results are consistent with Glauert predictions about angular momentum in rotary wing systems, and could be used to predict the swirl velocity in the real systems. The velocity is r direction is decreasing along the streamline, which could be used to describe the contracting of the wake region in rotary wing systems.

Once the theory has been developed, several areas and applications are natural for the extension of the work. The most direct line of work that could be developed from the theory is to use it to calculate the drags with fuselage, which would need the inflow within wake region. Another direct of the applications would use it to calculate the inflow for parallel rotors systems (the configuration used in Sikorsky X2), side to side rotors systems (Karman helicopters), even the inflow for tandem systems (Chinook CH42).

For the development of theory, our model is for the flows that are linearized about V_∞, which could only work for cruise conditions. It will break down when the helicopter works in hover conditions since V_∞ goes to 0, which makes the equations singular. So it is necessary to derive a nonlinear version of the co-state method below the rotor disk. In the derivation of the model, we only consider potential inflow

without mass injection, how to complete and extend this theory across the rotor disk to treat with mass injections is still an open problem. Duffy shows how to generalize the inflow above the disk to nonlinear, and the same approach could be used here. However, below the rotor disk there must be an analysis of wake contraction. This is left to future researches.

Appendix 1. Coordinate System

The ellipsoidal coordinate system $(\nu,\eta,\bar{\psi})$ is defined as

$$x=-\sqrt{1-\nu^2}\sqrt{1+\eta^2}\cos(\bar{\psi}) \tag{A1.1}$$

$$y=\sqrt{1-\nu^2}\sqrt{1+\eta^2}\sin(\bar{\psi}) \tag{A1.2}$$

$$z=-\nu\eta \tag{A1.3}$$

where the coordinates ν,η and $\bar{\psi}$ are restricted to the following range

$$-1\le\nu\le 1 \tag{A1.4}$$

$$0\le\eta\le\infty \tag{A1.5}$$

$$0\le\bar{\psi}\le 2\pi \tag{A1.6}$$

Figure A1.1 shows the ellipsoidal coordinate system viewed in the *xz* plane. The surfaces for $\nu=$constant are hyperboloids and the surfaces for $\eta=$constant are ellipsoids. For the special case, $\eta=0$ represents the flat circular plane, and $\nu$is anti-symmetric along the plane which contains the $\eta=0$ circular plane. $\bar{\psi}$ is the azimuth angle measured from the negative x axis, with counterclockwise direction viewed along the positive z axis.

The non-dimensional radial position with the ellipsoidal coordinates could be obtained from equations (A1.1) and (A1.2), which is,

$$\bar{r}^2=x^2+y^2+z^2=\left(1+\eta^2\right)\left(1-\nu^2\right)+\nu^2\eta^2 \tag{A1.7}$$

Similarly, from equation (A1.1), (A1.2) and (A1.3), the ellipsoidal coordinates ν,η and $\bar{\psi}$ can be expressed in terms of x, y and z as

$$\nu=\frac{-sign(z)}{\sqrt{2}}\sqrt{1-\bar{S}+\sqrt{\left(\bar{S}-1\right)^2+4z^2}} \tag{A1.8}$$

$$\eta=\frac{1}{\sqrt{2}}\sqrt{\bar{S}-1+\sqrt{\left(\bar{S}-1\right)^2+4z^2}} \tag{A1.9}$$

$$\bar{\psi} = \tan^{-1}\left(\frac{-y}{x}\right) \tag{A1.10}$$

where

$$\bar{S} = x^2 + y^2 + z^2 \tag{A1.11}$$

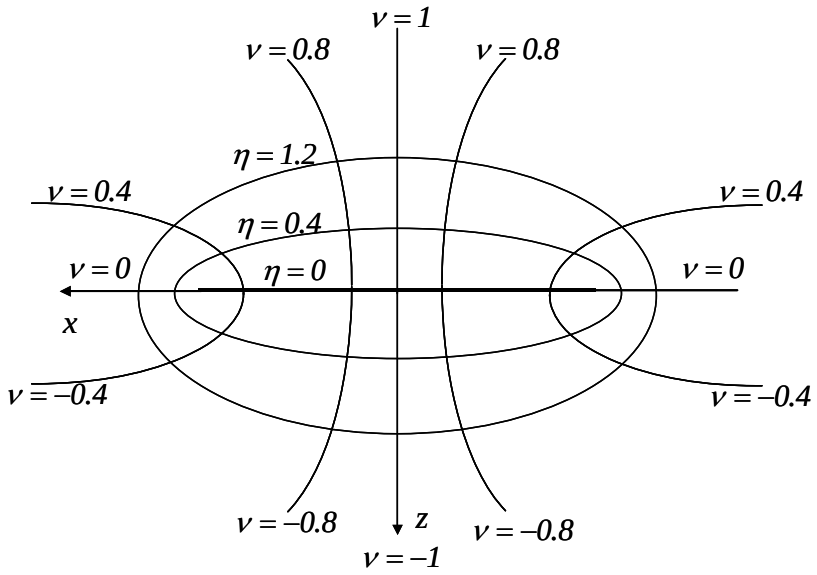

Figure A1.1 Ellipsoidal coordinate system

Appendix 2. Normalized Associated Legendre Functions

In the ellipsoidal coordinate system defined in Appendix 1, the Laplace's equation takes the form

$$\frac{\partial}{\partial \nu}\left[\left(1-\nu^2\right)\frac{\partial \Phi}{\partial \nu}\right]+\frac{\partial}{\partial \eta}\left[\left(1+\eta^2\right)\frac{\partial \Phi}{\partial \eta}\right]+\frac{\partial}{\partial \bar{\psi}}\left[\frac{\left(\nu^2+\eta^2\right)}{\left(1-\nu^2\right)\left(1+\eta^2\right)}\frac{\partial \Phi}{\partial \bar{\psi}}\right]=0 \quad \text{(A2.1)}$$

Using the principle of separation of variables to solve equation (A2.1), the Laplace equation is expressed by a multiplication of three separated parts which are only functions of ν,η and $\bar{\psi}$ respectively.

$$\Phi\left(\nu,\eta,\bar{\psi}\right)=\Phi_1\left(\nu\right)\Phi_2\left(\eta\right)\Phi_3\left(\bar{\psi}\right) \quad \text{(A2.2)}$$

Applying equation (A2.2) to equation (A2.1), the Laplace equation can be separated into the following three equations

$$\frac{d^2\Phi_3}{d\bar{\psi}^2}+m^2\Phi_3=0 \quad \text{(A2.3)}$$

$$\frac{d}{d\nu}\left[\left(1-\nu^2\right)\frac{d\Phi_1}{d\nu}\right]+\left[-\frac{m^2}{1-\nu^2}+n\left(n+1\right)\right]\Phi_1=0 \quad \text{(A2.4)}$$

$$\frac{d}{d\eta}\left[\left(1+\eta^2\right)\frac{d\Phi_2}{d\eta}\right]+\left[\frac{m^2}{1+\eta^2}-n\left(n+1\right)\right]\Phi_2=0 \quad \text{(A2.5)}$$

where m and n are the constant of separation.

Equations (A2.4) and (A2.5) are Legendre's associated differential equations, and the solutions to which are the associated Legendre Functions of the first kind and the second kind ($P_n^m\left(\nu\right)$, $P_n^m\left(i\nu\right)$, $Q_n^m\left(\eta\right)$ and $Q_n^m\left(i\eta\right)$). Since $P_n^m\left(i\nu\right)$ and $Q_n^m\left(\eta\right)$ will yield an infinite pressure in the flow field, so they are omitted.

For the purpose of this research, the associated Legendre functions of the first and second kind are normalized as

$$\bar{P}_n^m = (-1)^m \frac{P_n^m(\nu)}{\rho_n^m} \tag{A2.6}$$

$$\bar{Q}_n^m = \frac{Q_n^m(i\eta)}{Q_n^m(i0)} \tag{A2.7}$$

where

$$\left(\rho_n^m\right)^2 = \int_0^1 \left(P_n^m(\nu)\right)^2 d\nu = \frac{1}{2n+1}\frac{(n+m)!}{(n-m)!} \tag{A2.8}$$

$$Q_n^m(i0) = \begin{cases} \dfrac{\pi}{2}(-1)^{m+n+1}(i)^{n+1}\dfrac{(n+m-1)!!}{(n-m)!!}, & m+n = even \\ (-1)^{m+n+1}(i)^{n+1}\dfrac{(n+m-1)!!}{(n-m)!!}, & m+n = odd \end{cases} \tag{A2.9}$$

In this research, numerical codes are developed to compute all the required values of $\bar{P}_n^m(\nu)$ and $\bar{Q}_n^m(i\eta)$ based on the following recurrence relations

$$\bar{P}_{n+1}^m(\nu) = \sqrt{\frac{(2n+3)(2n+1)}{(n+1)^2-m^2}}\left[\nu\bar{P}_n^m(\nu) - \sqrt{\frac{n^2-m^2}{4n^2-1}}\bar{P}_{n-1}^m(\nu)\right] \tag{A2.1}$$

$$\bar{P}_{n+1}^m(\nu) = \sqrt{\frac{(2n+3)}{(n+m+1)(n+m)}}\left[\begin{array}{l}\sqrt{\dfrac{(n-m+1)(n-m)}{2n-1}}\bar{P}_{n-1}^m(\nu) \\ +\sqrt{1-\nu^2}\sqrt{2n+1}\bar{P}_n^{m-1}(\nu)\end{array}\right] \tag{A2.2}$$

$$\bar{P}_n^{m+1}(\nu) = \frac{1}{\sqrt{1-\nu^2}}\left[\sqrt{\frac{(2n+1)(n+m)}{(2n-1)(n+m+1)}}\bar{P}_{n-1}^m(\nu) - \frac{(n-m)}{\sqrt{(n+m+1)(n-m)}}\nu\bar{P}_n^m(\nu)\right] \tag{A2.3}$$

$$\bar{Q}_{n+1}^m(i\eta) = \bar{Q}_{n-1}^m(i\eta) - (2n+1)K_n^m\eta\bar{Q}_n^m(i\eta) \tag{A2.4}$$

$$\bar{Q}_n^{m+1}(i\eta) = \frac{1}{\sqrt{1+\eta^2}}\left[\bar{Q}_{n-1}^m(i\eta) - (n-m)K_n^m\eta\bar{Q}_n^m(i\eta)\right] \tag{A2.5}$$

where

$$K_n^m = \left(\frac{\pi}{2}\right)^{(-1)^{n+m}} H_n^m \tag{A2.6}$$

$$H_n^m = \frac{(n+m-1)!!(n-m-1)!!}{(n+m)!!(n-m)!!} \tag{A2.7}$$

$$(n)!! = \begin{cases} (n)(n-2)(n-4)\ldots(2) & \text{for } n \text{ even} \\ (n)(n-2)(n-4)\ldots(1) & \text{for } n \text{ odd} \end{cases} \tag{A2.8}$$

$$(0)!! = 1,\ (-1)!! = 1,\ (-2)!! = \infty,\ (-3)!! = -1$$

In order to calculate to the derivation of $\bar{P}_n^m(\nu)$ and $\bar{Q}_n^m(i\eta)$, the recurrence relations for are given by

$$(1-\nu^2)\frac{d\bar{P}_n^m(\nu)}{d\nu} = \sqrt{\frac{(2n+1)(n^2-m^2)}{(2n-1)}}\bar{P}_{n-1}^m(\nu) - n\nu\bar{P}_n^m(\nu) \tag{A2.9}$$

$$(1-\nu^2)\frac{d\bar{P}_n^m(\nu)}{d\nu} = \sqrt{(n+m+1)(n-m)}\sqrt{1-\nu^2}\,\bar{P}_n^{m+1}(\nu) - m\nu\bar{P}_n^m(\nu) \tag{A2.10}$$

$$(1+\eta^2)\frac{d\bar{Q}_n^m(i\eta)}{d\eta} = -\left[\frac{1}{K_n^m}\bar{Q}_{n+1}^m(i\eta) + (n+1)\eta\bar{Q}_n^m(i\eta)\right] \tag{A2.11}$$

$$(1+\eta^2)\frac{d\bar{Q}_n^m(i\eta)}{d\eta} = \sqrt{1+\eta^2}\,\frac{Q_n^{m+1}(i0)}{Q_n^m(i0)}\bar{Q}_n^{m+1}(i\eta) + m\eta\bar{Q}_n^m(i\eta) \tag{A2.12}$$

where K_n^m is defined by equation (A2.6).

A2.1. Orthogonality Integrals

$$\int_0^1 \bar{P}_j^m(\nu)\bar{P}_n^m(\nu)\,d\nu = \begin{cases} \delta_{jn}, & n+m = odd,\ j+m = odd \\ \delta_{jn}, & n+m = even,\ j+m = even \\ U_{jn}^m, & n+m = even,\ j+m = odd \end{cases} \tag{A2.13}$$

$$U_{jn}^m = \sqrt{\frac{H_n^m}{H_j^m}}\,\frac{\sqrt{(2j+1)(2n+1)}}{(j+n+1)(j-n)}(-1)^{\frac{j+n-2m-1}{2}} \tag{A2.14}$$

A2.2. Area Integrals

$$\int_0^1 \bar{P}_n^m(\nu)\bar{P}_j^m(\nu)\nu d\nu = \begin{cases} A_{jn}^m, & j+m=odd, n+m=odd \\ G_{jn}^m, & j+m=even, n+m=even \\ D_{jn}^m, & j+m=odd, n+m=even \end{cases} \tag{A2.15}$$

where A_{jn}^m, G_{jn}^m and D_{jn}^m are defined as:

$$A_{jn}^m = \frac{2}{\sqrt{H_n^m H_j^m}} \frac{\sqrt{(2n+1)(2j+1)}}{(n+j+2)(n+j)} \frac{(-1)^{\frac{n+j-2m}{2}}}{\left((j-n)^2-1\right)} \tag{A2.16}$$

$$G_{jn}^m = \begin{cases} \sqrt{H_j^m H_n^m}\sqrt{(2j+1)(2n+1)} \dfrac{\left(2m^2-n^2-j^2-n-j\right)}{(n+j+2)(n+j)} \dfrac{(-1)^{\frac{n+j-2m}{2}}}{\left((n-j)^2-1\right)}; \\ \qquad\qquad j\neq 0; n\neq 0; m\neq 0 \\ G_{00}^0 = \dfrac{1}{2} \quad j=n=m=0 \end{cases} \tag{A2.17}$$

$$D_{jn}^m = \begin{cases} \sqrt{\dfrac{1}{H_j^m H_n^m}} \dfrac{1}{\sqrt{(2j+1)(2n+1)}}, j=n\pm 1 \\ 0, j\neq n\pm 1 \end{cases} \tag{A2.18}$$

Appendix 3. Exact Solution to a Step Response in Axial Flow

Based on the momentum equations, for axial flow ($\chi = 0$) with a free-stream velocity V_∞ the momentum equation could be written

$$\frac{\partial v_z}{\partial \tau} + \frac{\partial v_z}{\partial z} = -\frac{\partial P}{\partial z} \tag{A3.1}$$

where P is the pressure and v_z is velocity field. If we only consider a step input, $P(z)u(\tau)$, with zero initial conditions, then the particular solution for (A3.1) is clear,

$$v = -P \tag{A3.2}$$

The homogeneous solution is any function of $z-\tau$, defined as $f(z-\tau)$. Thus, outside the wake, we have

$$v_z(z,\tau) = f(z-\tau) - P(z) \tag{A3.3}$$

For zero initial condition, it requires

$$v_z(z,0) = f(z) - P(z) = 0 \tag{A3.4}$$

Then it is easily known that

$$f(z) = P(z) \tag{A3.5}$$

Inside the wake, we have a similar formulation of the total solution

$$v_z(z,\tau) = g(z-\tau) - P(z), \quad \begin{cases} 0 < z < \tau \\ -1 < x < +1 \end{cases} \tag{A3.6}$$

where $g(z-\tau)$ is any homogeneous solution to equation (A3.7). However, there is no initial condition since no wake at $\tau = 0$. A boundary condition at the disk should be included at this case.

Typically, based on momentum inflow theory, the inflow region could be divided into 2 parts, the region above the disk (A in Figure A3.1) and the wake region (B in Figure A3.1). As the flow could be caused by potential differences or mass

flow changes at the disk, the boundary conditions for each case may differ, so we need to deal with it separately.

If the inflow is caused by pressure difference across the rotor disk, the velocity should be continuous across the disk and the pressure will satisfy $P(0^+) = -P(0^-)$ (positive at $z = 0^+$, negative at $z = 0^-$).

From (A3.3) and (A3.5), we know that the velocity at $z = 0^-$ is

$$v_z\left(0^-, \tau\right) = P\left(-\tau\right) - P(0^-) \tag{A3.7}$$

However, from (A3.6) for $z = 0^+$ inside the wake, we have

$$v_z\left(0^+, \tau\right) = g(-\tau) - P(0^+) \tag{A3.8}$$

As for pressure difference, there is no velocity jump across the disk, so

$$v_z\left(0^-, \tau\right) = v_z\left(0^+, \tau\right) \tag{A3.9}$$

which means

$$v_z\left(0^+, \tau\right) = g(-\tau) - P(0^+) = P\left(-\tau\right) - P(0^-) \tag{A3.10}$$

Combining (A3.8) and (A3.10), we will have

$$g(-\tau) = P\left(-\tau\right) + 2P(0^+) \tag{A3.11}$$

Thus for pressure difference across the rotor disk, the velocity inside the wake satisfy

$$v_z\left(z, \tau\right) = P\left(z - \tau\right) - P(z) + 2P(0^+) \tag{A3.12}$$

However, for the case of mass injection, we know that the pressure is continuous across the disk, so that $P(0^+) = P(0^-)$. But there is a velocity difference between the both sides of the rotor , which is $2P(0^+)$

$$v_z\left(0^-, \tau\right) + 2P(0^+) = v_z\left(0^+, \tau\right) \tag{A3.13}$$

From (A3.8), we know for $z = 0^+$ inside the wake

$$v_z\left(0^+,\tau\right)=g(-\tau)-P(0^+) \tag{A3.14}$$

Then we can obtain $g(-\tau)$ from (A3.13) and (A3.14) as

$$g(-\tau)=P\left(-\tau\right)+2P(0^+) \tag{A3.15}$$

Inside the wake for mass injection, we have

$$v_z\left(z,\tau\right)=P\left(z-\tau\right)-P(z)+2P(0^+) \tag{A3.16}$$

Above all, we can conclude that, for both pressure difference and mass injection, the flow inside the wake will have the following format

$$v_z\left(z,\tau\right)=P\left(z-\tau\right)-P(z)+2P(0^+) \tag{A3.17}$$

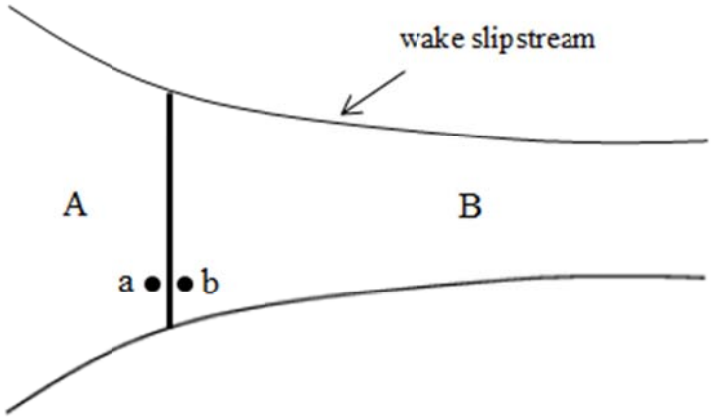

Figure A3.1 Momentum theory flow

Appendix 4. Adjoint velocity for a Step Response in Axial Flow

From Peters-Morrilo model, in order to obtain the time response by Galerkin method, we need to write the momentum equation as

$$\left[M^c\right]\left\{\overset{*}{a}{}_n^m\right\}+\left[D^c\right]\left[\tilde{L}^c\right]^{-1}\left[M^c\right]\left\{a_n^m\right\}=\left[D^c\right]\left\{\tau_n^{mc}\right\} \tag{A4.1}$$

and time-marching from τ_o to τ_f with a time step $\Delta\tau$.

Then the changing of velocity potentials could be represented by

$$\left\{a_n^m(\tau)\right\}=\left[\left\{a_n^m(\tau_o)\right\},\left\{a_n^m(\tau_1)\right\},\ldots,\left\{a_n^m(\tau_f)\right\}\right] \tag{A4.2}$$

The velocity between τ_o and τ_f could be obtained by substituting the value of a_n^m at that specific time into equations (A4.1). For $\tau<\tau_o$, we just assume $\left\{a_n^m(\tau)\right\}=\{0\}$.

Here we need to extend the momentum equation in Peters-Morrilo's model to describe the velocity field for time responses based on the co-states method. First we need to define the co-states Δ_n^m to calculate the adjoint velocity, which satisfies the following equation

$$-\left[M^c\right]\left\{\overset{*}{\Delta}{}_n^m\right\}+\left[D^c\right]\left[\tilde{L}^c\right]^{-1}\left[M^c\right]\left\{\Delta_n^m\right\}=\left[D^c\right]\left\{\tau_n^{mc}\right\} \tag{A4.3}$$

For the adjoint velocity coefficient, if time is between τ_o to τ_f, then $\Delta_n^m(\tau)=\left\{\tau_n^{mc}\right\}$, which means it is equivalent to the forcing function. However, if $\tau<\tau_o$, there will be no forcing functions in equation (A4.3), we need to time-marching backward from τ_o to τ_p with a step $\Delta\tau$ to the following homogeneous equation

$$-\left[M^c\right]\left\{\overset{*}{\Delta}_n^m\right\}+\left[D^c\right]\left[\tilde{L}^c\right]^{-1}\left[M^c\right]\left\{\Delta_n^m\right\}=\{0\} \tag{A4.4}$$

Then the changing of adjoint velocity potentials before τ_o could be

$$\left\{\Delta_n^m(\tau)\right\}=\left[\left\{\Delta_n^m(\tau_p)\right\},\left\{\Delta_n^m(\tau_{p1})\right\},\ldots,\left\{\Delta_n^m(\tau_o)\right\}\right] \tag{A4.5}$$

Even though the differential equations are unstable while time goes forward, it will decay to zero when time goes backward. From section 3.3, we know that the velocity below the rotor disk could be expressed as

$$\vec{v}(r_0,\bar{\psi}_0,\xi_0,\tau)=\vec{v}(r_0,\bar{\psi}_0,0,\tau-\xi_0)+\vec{v}^*(r_0,\tilde{\psi}_0,0,\tau-\xi_0)-\vec{v}^*(r_0,\tilde{\psi}_0,-\xi_0,\tau) \tag{A4.6}$$

So that means we need to time marching Δ_n^m backwards from τ to $\tau-\xi_0$, where ξ_0 is the depth needed in wake along the free streamline.

Appendix 5. Table Method

In order to calculate the induced flow using Hsieh-Duffy model, it is required to truncate the number of harmonics and the number of radial shape. The number of harmonics is chosen based on the highest dynamic frequency of interest, and the choice of the number for radial shape functions using in each harmonics was based on a mathematically consistent hierarchy way, which is shown in Table A5.1. The number of radial shape function for $m+n=even$ is equal to the number for $m+n=odd$, which is the result of adding up each one of the terms included for each harmonic.

Table A5.1 Choice for the Number of Spatial Modes ($n+m=odd$)

Highest power of $\bar{r}$	m									Total Inflow States
	0	1	2	3	4	5	6	7	8	
0	1									1
1	1	1								3
2	2	1	1							6
3	2	2	1	1						10
4	3	2	2	1	1					15
5	3	3	2	2	1	1				21
6	4	3	3	2	2	1	1			28
7	4	4	3	3	2	2	1	1		36
8	5	4	4	3	3	2	2	1	1	45

References

1. Joglekar, M. and Loewy, R. “An Actuator-Disc Analysis of Helicopter Wake Geometry and the Corresponding Blade Responses,” USAAU-LABS Technical Report 69-66, 1970.
2. Pitt, Dale. M. and Peters, David A., “Theoretical Prediction of Dynamic-Inflow Derivatives,” *Vertica*, Vol. 5, No. 1, March 1981, pp. 21-34.
3. Gaonkar, Gopal H. and Peters, David A., “Effectiveness of Current Dynamic-Inflow Models in Hover and Forward Flight,” *Journal of the American Helicopter Society*, Vol. 31, No. 2, April 1986, pp. 47-57.
4. Peters, David A., Boyd, David Doug, and He, Cheng Jian, “A Finite-State Induced-Flow Model for Rotors in Hover and Forward Flight,” *Journal of the American Helicopter Society*, Vol. 34, No. 4, October 1989, pp. 5-17.
5. Peters, David A. and He, Cheng Jian, “Correlation of Measured Induced Velocities with a Finite-State Wake Model,” *Journal of the American Helicopter Society*, Vol. 36, No. 3, July 1991, pp. 59-70.
6. Morillo, Jorge and Peters, David A., “Velocity Field above a Rotor Disk by a New Dynamic Inflow Model,” *Journal of Aircraft*, Vol. 39, No. 5, September-October 2002, pp. 731-738.
7. Peters, David A. and Cao, Wenming, “Off-Rotor Induced Flow by a Finite-State Wake Model,” 37th AIAA SDM Conference, Salt Lake City, April 15-17, 1996, Paper No. 96-1550.
8. Yu, Ke and Peters, David A., “Nonlinear Three-Dimensional State-Space Modeling of Ground Effect with a Dynamic Flow Field,” *Journal of the American Helicopter Society*, Vol. 50, No. 3, July 2005, pp. 259-268.
9. Hsieh, Antonio, *A Complete Finite-State Model for Rotors in Axial Flow*, Master of Science Thesis, Washington University in St. Louis, August 2006.
10. Peters, David A., Hsieh, Antonio, and Garcia-Duffy, Cristina, “A Complete Finite-State Inflow Theory from the Potential Flow Equations,” Given as the Keynote Lecture and included in the Proceedings of the 3rd International Basic Research Conference on Rotorcraft Technology, Nanjing, China, Oct. 14-16,

2009.

11. Currie, I.G., Fundamental Mechanics of Fluids, 2nd Edition, McGraw Hill, United States of America, 1993, p.31.
12. Craig, Roy R. and Kurdila, Andrew J., “Fundamentals of structural dynamics,” 2nd edition, John Wiley & Sons, United States of America, 2006.
13. Wang, Yi-Ren and Peters, David A., “The lifting rotor inflow mode shapes and blade flapping vibration system eigen-analysis,” Computer methods in applied mechanics and engineering, Vol. 134, 1996, pp. 91-105.
14. Morillo, Jorge and Peters, David, “Convergence of Complete Finite-State Inflow Model of A Rotor Flowfield,” the 28th European Rotorcraft Forum, Bristol, England, 2002.
15. Su, Ay, Yoo, Kyung M. and Peters, David A., “Extension and Validation of an Unsteady Wake Model for Rotors,” Journal of Aircraft, Vol. 29, No. 3, May-June, 1992.
16. Prasad, J.V.R., Nowak, Margon, and Xin Hong, “Finite State Inflow Models for a Coaxial Rotor in Hover,” the 38th European Rotorcraft Forum, Amsterdan, Netherlands, 2012.
17. Morillo, Jorge, “A Fully Three-Dimensional Unsteady Rotor Inflow Model Developed in Closed Form from a Galerkin Approach,” Doctor of Science Dissertation, Washington University, December 2001.
18. Makinen, Stephen M., Applying Dynamic Wake Modes to Large Swirl Velocities for Optimal Propellers, Doctor of Science Thesis, Washington University, May 2005.

Vita

Zhongyang Fei

Degrees

Ph.D., Mechanical Engineering, Washington University in St Louis, May 2013
M.S., Aerospace Engineering, Washington University in St Louis, May 2011
M.S., Control Science & Engineering, Harbin Institute of Technology, July 2009
B.S., Control Science & Engineering, Harbin Institute of Technology, July 2007

Professional

American Helicopter Society (AHS)
American Institute of Aeronautics and Astronautics (AIAA)

Publications

Zhongyang Fei and David Peters. Applications of Generalized Dynamic Wake Theory of the Flow in a Rotor Wake. Proceedings of the 69th Annual Forum of the American Helicopter Society, 2013.

Zhongyang Fei and David Peters. Inflow below the Rotor Disk for Skewed Flow by the Finite-state, Adjoint Method. The 38th European Rotorcraft Forum, Amsterdam, 2012.

Zhongyang Fei and David Peters. Eigenvalues and Mode Shapes for the Complete Rotor Dynamic-Wake Model. The 30th AIAA Applied Aerodynamics conference, New Orleans, Louisiana, 2012.

Zhongyang Fei and David Peters. A Rigorous Solution for Finite-state Inflow throughout the Flowfield. The 30th AIAA Applied Aerodynamics conference, New Orleans, Louisiana, 2012.

Xi Rong, David Peters and Zhongyang Fei. Optimum Pitch Settings and RPM for Tethered, Yawed Wind Turbines. Proceedings of the 30th ASME Wind Energy Symposium and 50th AIAA Aerospace Sciences Meeting, Nashville, Tennessee, 2012.